Vol. 25 Nos. 117/118 *Journal of the Radio Research Laboratories* *July/Nov. 1978*
Printed in Tokyo, Japan *pp. 153–246*

IONOSPHERIC PLASMA PROBE STUDIES AND IONOSPHERIC STRUCTURE STUDIES BY SPACE VEHICLE OBSERVATIONS*

By
Shigeru Miyazaki

(Received on April 26, 1978)

CONTENTS

ABSTRACT

CHAPTER I OUTLINE DESCRIPTIONS OF THE IONOSPHERIC RESEARCH BY SPACE VEHICLES

CHAPTER II IONOSPHERIC PLASMA PROBE
- 2.1 Survey of Methods of Measurement of the Ionosphere and Classification of Plasma Probe
- 2.2 Characteristic of Ion Collection of Spherical Langmuir Probe in Drifting Maxwellian Distribution
  - 2.2.1 Introduction
  - 2.2.2 Current-Voltage Characteristic
  - 2.2.3 Theoretical Consideration for Extreme Cases
  - 2.2.4 Summary
- 2.3 Retarding Potential Analyzer
  - 2.3.1 Introduction
  - 2.3.2 Theoretical Consideration of Current-Voltage Characteristic
  - 2.3.3 Method of Measurement
  - 2.3.4 Summary
- 2.4 Resonance Probe
  - 2.4.1 Introduction
  - 2.4.2 Model of Ion Sheath Profile
  - 2.4.3 Impedance/Admittance Profile of Sheath Plasma System
  - 2.4.4 Summary
- 2.5 Two-Wire Radio Frequency Probe
  - 2.5.1 Introduction
  - 2.5.2 Impedance between Two Wires
  - 2.5.3 Numerical Examples
  - 2.5.4 Summary
- 2.6 Special Features of the Space-Vehicle Use of Probes

CHAPTER III IONOSPHERIC STUDIES BY SOUNDING ROCKETS
- 3.1 Rocket Observations at Akita Rocket Range
  - 3.1.1 Introduction
  - 3.1.2 Instruments

* A thesis presented to the University of Tokyo in partial fulfillment of the degree of Doctor of Science.

3.1.3 Observational Results
3.1.4 Summary and Discussions
3.2 Rocket Observations during the IQSY at Kagoshima Space Center
3.2.1 Introduction
3.2.2 Instruments
3.2.3 Observational Results
3.2.4 Summary and Discussions
3.3 Relation between Sunspot Number and Charged Particle Density in the Upper Ionosphere
3.3.1 Introduction
3.3.2 Instruments
3.3.3 Observational Results
3.3.4 Relation between Sunspot Number and Charged Particle Density
3.3.5 Summary and Discussions

CHAPTER IV RELATION BETWEEN LOWER IONOSPHERIC ELECTRON DENSITY PROFILES AND COSMIC NOISE ABSORPTION DURING AURORAL ZONE DISTURBANCES
4.1 Introduction
4.2 Instruments
4.3 Observational Results
4.4 Relation between Lower Ionospheric Electron Density Profiles and Cosmic Noise Absorption
4.5 Summary and Discussions

CHAPTER V ION TRANSITION HEIGHT CHARACTERISTICS IN THE TOPSIDE IONOSPHERE BY SATELLITE TAIYO OBSERVATION
5.1 Introduction
5.2 TAIYO RPA Instrumentation and Orbit
5.3 Longitudinal and Latitudinal Variations of Ion Transition Heights
5.4 Summary and Discussions

CHAPTER VI CONCLUDING REMARKS

ACKNOWLEDGEMENTS

REFERENCES

Zusammenfassung

Die Erde ist mit einer dichten Atmosphäre umgeben. Die Moleküle und Atome der oberen Atmosphäre sind hauptsächlich durch die kurzwellige ultraviolette Sonnenstrahlung, durch die Röntgenstrahlung und durch die korpuskularen Teilchen ionisiert, so daß ein Plasma entsteht, das Ionosphäre genannt wird, welches sich oberhalb von etwa 50 km bis zu den Höhen der oberen Grenze der Atmosphäre ausbreitet. Die Existenz der Ionosphäre spielt eine wichtige Rolle nicht nur im Hinblick auf die Radiowellenausbreitung sondern auch bei solarterrestrischen Phänomenen. Es ist sehr wichtig ein genaues Wissen über den physikalischen Zustand der Ionosphäre zu erhalten und deswegen ist es wichtig die Physik der oberen Atmosphäre und der Ionosphäre zu erforschen.

In Kapitel I ist ein historischer Überblick über die Ionosphärenforschung gegeben.

In Kapitel II ist zuerst ein Überblick der direkten Ionosphärenmessungen gegeben, die bis heute gemacht wurden. Die elektrischen Eigenschaften der elektrostatischen Sonde und der Sonde für elektromagnetische Wellen werden beschrieben. Mit der Theorie der Langmuirsonde wird die Kennlinie des Ionenstromes einer kugelförmigen Sonde mit einer

Relativgeschwindigkeit gegenüber dem Plasma betrachtet. Als Nächstes wird der Gegenspannungsanalysator mit planarer, zylindrischer oder kugelförmiger Elektrode betrachtet. Bei der Sonde für die elektromagnetischen Wellen, sind für die Resonanz-Sonde und die Impedanz-Sonde mit parallelen Drähten Kennlinien und deren numerische Beschreibung gegeben. Zum Schluß, werden spezielle Probleme bei der Verwendung der Sonden auf Raumfahrzeugen erörtert.

In Kapitel III werden Beobachtungsergebnisse der Ionosphäre durch Raketenaufstiege von dem Raketenschußplatz in Akita und dem "Kagoshima Space Center" beschrieben. Als Ergebnis wird eine Beziehung zwischen der Sonnenfleckenzahl und der Dichte der geladenen Teilchen in der Ionosphäre abgeleitet. Außerdem werden verschiedene Eigenschaften der Elektronendichteverteilung beleuchtet.

Die zwölfte, dreizehnte und vierzehnte japanische Antarktische Forschungsexpedition führte einundzwanzig Raketenschüsse durch um die polare Ionosphäre und die Aurora Phänomene in "Syowa Station", Antarktis in der Zeit von 1971 bis 1973 zu beobachten. Die Elektronendichte Profile der Ionosphäre bei verschieden gestörten Bedingungen wurden von zwei S-160JA und zwölf S-160JA Raketen-Experimenten gemessen. In Kapitel IV werden Beobachtungsergebnisse der Elektronendichtemessungen und die Abhängigkeit der Elektronendichte der niederen Ionosphäre von der Absorption des cosmischen Rauschens während einer Aurora beschrieben.

In Kapitel V wird der Gegenspannungsanalysator an Bord des Satelliten "TAIYO" beschrieben. Mit Hilfe dieses Gegenspannungsanalysators werden longitudinale Änderungen der O^+ und H^+ "Übergangshöhe" in der oberen Ionosphäre bei niederen Breiten während der Zeit minimaler Sonnenfleckenzahl beobachtet. Die Ergebnisse zeigen, daß die "Übergangshöhe" der Ionen in der Gegend der geomagnetischen Süd-Atlantik Anomalie wesentlich niederer liegt als in anderen Gebieten auf der Tagseite. Dies bedeutet, daß die "Übergangshöhe" der Ionen eine enge Beziehung zum geomagnetischen Feld hat.

Im letzten Kapitel VI werden kurz die Ergebnisse zusammengefasst und ionosphärische Plasmasonden beschrieben.

Chapter I Outline of Descriptions of the Ionospheric Research by Space Vehicles

Japanese rocket research was initiated in 1955. Sounding rocket, Kappa was one of two rocket projects which the Scientific Council of Japan undertook for the International Geophysical Year, 1957 to 1958. The Kappa project was to develop a multistaged, solid-propellant, ground-launched sounding rocket. The Sigma rocket was used only once for cosmic ray observation, but this type of vehicle will not be used again. The approach to the Kappa rocket was made in two steps. The research started in February, 1955. As the first step, the miniature rocket called the Pencil rocket, was fired in April, 1955 for the basic study. In August, 1955, as the second step, larger rocket called Baby was tested. The first firing of the Kappa rocket, K-1-1, took place on September 24, 1956, without booster. Kappa rocket was designed specifically for upper atmosphere sounding. The design was handled by the Sounding Group of the Institute of Industrial Science of the University of Tokyo. The first large-scale rocket range was on the coast at Michikawa, Akita Prefecture in the northern part of Honshu, facing the Japan Sea. The K-8-1 rocket was fired at 1324 hours on July 11, 1960 and reached peak altitude of 150 km which was the highest record in Japan at that time. Since then, many scientific sounding rockets of K-8 type were

launched and reached peak altitude of 200 km. The ionospheric observation could be done by the K-8 rocket. Thus, the successes of K-8 rocket firings brought to the new age to the upper atmospheric research. In 1961, a three-stage rocket K-9L was developed and an altitude of about 350 km was attained. The introduction of this rocket made it necessary to move the launching site to Uchinoura, Kagoshima Prefecture in the south of Kyushu Island, facing the Pacific Ocean. At the end of 1962, a new two-stage rocket K-9M was developed which had the payload capacity of 85 kg up to 350 km altitude. This rocket had high reliability for the medium altitude sounding. In 1963, Lambda engine was developed, with its diameter 73.5 cm and thrust 50 tons. A rocket called L-3H can carry simultaneously 100 kg payload up to 2100 km by the third stage rocket and 170 kg payload up to 430 km by the second stage rocket.

On the other hand, the first Japanese satellite "OHSUMI" was successfully launched by the Lambda-4S rocket from the Kagoshima Space Center on February 11, 1970. The orbital parameters were; period 144.6 min., perigee 351 km, apogee 5142 km and inclination 31.2°. After the Mu-4S project by the Institute of Space and Aeronautical Science of the University of Tokyo was completed, putting three satellites TANSEI, SHINSEI and DENPA into orbit, a new launch vehicle, Mu-3C, with radio guidance and control systems has been developed for more elaborate mission objectives. The test satellite, TANSEI-II, was launched by Mu-3C-1 from the Kagoshima Space Center on February 16, 1974. With the success of Mu-3C-1 and TANSEI-II, ISAS has proceeded to the Mu-3C Scientific Satellite Project. The Solar Radiation and Thermospheric Structure Satellite, TAIYO (formaly reffered to as SRATS), was successfully launched at 1425 JST on February 24, 1975 (Hirao, 1975).

A development of single stage rockets has been carried out to make the firing operation easy. Two kinds of single stage rocket with their diameters of 160 and 210 mm were developed for the ionospheric sounding and the exploration of auroral phenomena at the Japanese Antarctic base, Syowa Station. Upon reopening of the observations of geophysical phenomena at Syowa Station by the seventh JARE party in 1966, a concrete plan for rocket observation of the upper atmosphere was made in addition to the usual ground-based observations. The rocket center, radar-telemeter center and control center buildings were built by the tenth JARE party, and a rocket launcher was constructed by the eleventh JARE party. Two S-160 rockets were fired with success in February, 1970 as the preliminary experiments. Since then, a total of twenty-one rockets; two S-160 and nineteen S-210 rockets were fired during the auroral phenomena appearance in 1971–73 by the following three JARE parties and various ionospheric disturbances were observed. Furthermore, a new single stage rocket with diameter of 310 mm was developed. Japanese Antarctic Research Expedition 1976–78 which are the years of the IMS, launchings of sounding rockets, S-210 and S-310 type, are carried out.

Chapter II Ionospheric Plasma Probe

2.1 Survey of Methods of Measurement of the Ionosphere and Classification of Plasma Probe

There are two kinds of methods, the electrostatic probe and the radio frequency probe as the typical rocket- or satellite-borne instruments. Each method has proper merits and demerits. Furthermore, the electrostatic probe method is devided into Langmuir probe method, double probe method, ion trap method, retarding potential analyzer, Gerdien

condenser and so on. All the above described methods are based on the electrostatic property of a plasma.

On the other hand, a plasma shows the complex impedance to the radio frequency for the interaction between a plasma and the electromagnetic field and the impedance changes with the frequency. Plasma also indicates singularity on the specific frequency such as the plasma frequency, the cyclotron frequency when the magnetic field exists, the frequency relating to the sheath around the probe inserted in a plasma, that is, the space charge layer, and the hybrid frequency. The radio frequency probe method is one by which the plasma parameters are measured by the use of such a property of a plasma. This method is subdivided into the following four groups:

a) Impedance measurement of a plasma at a fixed frequency.
b) Measurement of the resonant frequency of the resonant or oscillator circuit on the assumption that a plasma is an element of the circuit.
c) Measurement of phenomena occurring at the specific frequency such as the plasma frequency.
d) Electromagnetic wave propagation method, topside sounding method and so forth.

In the above-described radio frequency probe methods, which method to be adopted for plasma measurement depends on the individual case. However, whichever method is adopted, it is very important to consider the configuration of electrodes, magnetic field, boundary conditions and the space charge layer problems.

In 1957, the first ionospheric plasma observation by a radio frequency probe method was done by Jackson and Kane (1959). The method was the measurement of antenna impedance in Seddon CW propagation experiment of 7.75 MHz. Since then, various radio frequency probe methods have been used to measure the ionospheric plasma. Typical methods are listed in the followings:

1) Standing wave impedance probe; Univ. of Utah, AFCRL.
2) RF conductivity probe; Penn. State Univ. (RF capacitance probe).
3) Gyro-plasma probe; Kyoto Univ.
4) VLF admittance probe.
5) RF probe; Univ. of Birmingham.
6) NASA impedance probe (RF short whip antenna).
7) Antenna resonance; Univ. of Birmingham and Univ. of Utah.
8) RF probe; DRTE.
9) Plasma frequency probe; Univ. of Utah.
10) Resonance probe (Resonance rectification probe); RRL.

Evaluation of radio frequency probes for use in ionospheric studies always presents a problem. In practice, evaluation has usually been carried out by the comparison with or more probe methods, or with simultaneous propagation experiments, either carried or the same vehicle or performed by ground-based, vertical incidence soundings (Heikkila *et al.*, 1968; Baker *et al.*, 1966; Ulwick *et al.*, 1962).

As far as studies in the lower ionosphere are concerned, collision frequency measurements are as much important as electron density measurements. These quantities can be deduced from the measurements of complex impedance by a radio frequency probe method.

Since the radio frequency probe is a comparatively new device, as far as operation in the upper atmosphere is concerned, various applications and theoretical considerations in complex situation are future problems.

2.2 Characteristic of Ion Collection of the Spherical Langmuir Probe in Drifting Maxwellian Distribution

2.2.1 Introduction

When there exists a finite relative velocity between a plasma and a spherical probe, there are some analyses of the probe characteristics in the electron collection region, but there is little analysis of the characteristics of ion collection taking into consideration the penetrating electric field into a plasma from the sheath region around the probe. Although the current-voltage characteristics of the probe analysed in various cases where there is no relative velocity between a plasma and a probe (Huddlestone and Leonard, 1965), the characteristics are analysed only in simple cases except the planar probe because of difficulties in mathematical analysis when there is relative velocity between a plasma and a probe as in the positive column with the axial electric field or of ionospheric and exospheric plasma to be measured by sounding rocket or satellite.

Mott-Smith and Langmuir (1926) analysed the characteristic of the cylindrical probe in the case of the sheath of large dimention, assuming the shape of the sheath to be coaxial. Heatley (1937) also analysed approximately the characteristic of a cylindrical probe without any assumption of the sheath dimension and shape. Medicus (1962) analysed a spherical probe in the region of electron collection in drifting Maxwellian distribution by the single energy method. The boundary between a plasma and the sheath can be defined in the electron collection region, but it can not be defined in the ion collection region, and the transition region (pre-sheath) from sheath to a plasma must be considered (Allen *et al.*, 1957). The motion of ions is affected by the penetrating electric field existing in the pre-sheath region. Dote *et al.*, (1962) analysed the characteristic of a spherical probe by considering the penetrating electric field in the ion collection region in drifting Maxwellian distribution, dividing the spherical probe into infinite small planar probes, and assuming the shape of the sheath in the behind region. In this section is analysed the characteristic of ion collection of the spherical Langmuir probe in drifting Maxwellian distribution by the use of the single energy method (Medicus, 1962).

2.2.2 Current-Voltage Characteristic

The current-voltage characteristic of a probe inserted in a plasma can be analysed in principle by Boltzmann's kinetic equation and Poisson's equation (Alpert *et al.*, 1962). They are as follows:

$$\begin{cases} \dfrac{\partial f_e}{\partial t} + V\dfrac{\partial f_e}{\partial r} + \left\{-\dfrac{1}{m}\dfrac{\partial U}{\partial r} - \dfrac{e}{m}\dfrac{\partial \varphi}{\partial r} + \dfrac{e}{mc}(H \times V)\right\}\dfrac{\partial f_e}{\partial V} = \left(\dfrac{\partial f_e}{\partial t}\right)_{\text{coll}}, \\ \dfrac{\partial f_i}{\partial t} + V\dfrac{\partial f_i}{\partial r} + \left\{-\dfrac{1}{M}\dfrac{\partial U}{\partial r} + \dfrac{e}{M}\dfrac{\partial \varphi}{\partial r} - \dfrac{e}{Mc}(H \times V)\right\}\dfrac{\partial f_i}{\partial V} = \left(\dfrac{\partial f_i}{\partial t}\right)_{\text{coll}}, \quad \cdots\cdots\cdots \quad (1) \\ \Delta\varphi = 4\pi e\left\{\int f_e d^3V - \int f_i d^3V\right\}, \end{cases}$$

where f_e and f_i are the distribution functions of electrons and ions, $\varphi = \varphi(r)$ is the potential of the electric field, $U = U(r, t)$ is the potential energy for the interaction of the charged particles with the surface of the electrode, and at infinity, $\varphi \to 0$, and the boundary condition for the potential $\varphi(r)$ at the surface depends on the type of the surface (dielectric, metal) and on the value of charge. Furthermore, as the motion of charged particles is not disturbed at infinity, the distribution functions of electrons and ions become Maxwell-Boltzmann distribution:

$$f_e(U) = n_e \left(\frac{m}{2\pi k T_e}\right)^{3/2} \exp\left\{-\frac{mU^2 - e\varphi(r)}{2kT_e}\right\},$$
$$f_i(U) = n_i \left(\frac{M}{2\pi k T_i}\right)^{3/2} \exp\left\{-\frac{MU^2 + e\varphi(r)}{2kT_i}\right\}, \quad \cdots\cdots (2)$$

Thus, the probe current is as follows:

$$J = J_i - J_e = \int_S U_i f_i dS - \int_S U_e f_e dS, \quad \cdots\cdots (3)$$

where S is the surface area of the probe.

As it is very difficult to solve the above equations, the characteristic of a spherical probe is here analysed by the single energy method. At first, there are three assumptions as follows: i) There is no collision in the sheath, ii) there is no reflection of charged particles at the probe surface, and iii) the shape of the sheath is spherical. The assumptions i) and ii) are general. Although the assumption iii) is correct in the isotropic distribution function, the effect due to the change of shape of sheath can be neglected by the single velocity method of considering the impact parameter even in the general drifting Maxwellian distribution. Medicus (1961) derived the expressions of the probe ion current by using the above assumptions as follows:

In the accelerating potential,

$$J(\eta_v) = \pi e n v_c \left\{ r_s^2 \int_0^{\alpha_k} \alpha F(\alpha) d\alpha + r_p^2 \int_{\alpha_k}^{\infty} \alpha \left(1 + \frac{\eta_v}{\alpha^2}\right) F(\alpha) d\alpha \right\}, \quad \cdots\cdots (4)$$

In the retarding potential,

$$J(\eta_v) = \pi e n v_c r_p^2 \int_{\alpha_v}^{\infty} \alpha \left(1 + \frac{\eta_v}{\alpha^2}\right) F(\alpha) d\alpha. \quad \cdots\cdots (5)$$

where e is the ionic charge, n the total ion density, r_s the sheath thickness, r_p the probe radius, $v_c = (2kT_i/M)^{1/2}$, $F(v)$ the distribution function, v the ion velocity, $\alpha = v/v_c$, $\alpha_k = v_k/v_c$, $Mv_k^2/2e = -V/\{(r_s/r_p)^2 - 1\}$, $Mv_c^2 = 2eU_c$, V the probe voltage and $\eta_v = -V/U_c$.

The drifting Maxwellian distribution function was also derived by Medicus in the following way:

$$F(\alpha) = \frac{2}{\sqrt{\pi}} \frac{\alpha}{\alpha_0} \epsilon^{-\alpha^2 - \alpha_0^2} \sinh(2\alpha\alpha_0), \quad \cdots\cdots (6)$$

where u is the drift velocity and $u/v_c = \alpha_0$.

In the case of ion collection, the effect of the penetrating electric field in the pre-sheath, that is, the acceleration of the ion in the pre-sheath before reaching the sheath edge, demands

consideration. Thus, the distribution function at the sheath edge is:

$$F(\alpha) = \frac{2}{\sqrt{\pi}} \frac{\alpha-\beta}{\alpha_0} \epsilon^{-(\alpha-\beta)^2-\alpha_0{}^2} \sinh\{2(\alpha-\beta)\alpha_0\}, \quad \cdots\cdots\cdots\cdots\cdots\cdots (7)$$

where $\beta = v_{ps}/v_C$ and v_{ps} is the quantity of increasing velocity after acceleration in the pre-sheath. When the potential across the sheath is large enough, $v_{ps} = (kT_e/M)^{1/2}$, $\beta = (T_e/2T_i)^{1/2}$ and $v_{ps} = 0$ at the plasma space potential.

Thus, the characteristic of ion collection of the spherical Langmuir probe in drifting Maxwellian distribution is derived from the distribution function in consideration of the penetrating electric field and the equation of the probe current expressed by integrals. The results are as follows:

In the accelerating potential,

$$\begin{aligned} J(\eta_v) = \sqrt{\pi}\, en\, v_C r_s^2 \Bigg[& \epsilon^{-\alpha_0{}^2} + \left(\frac{1}{\alpha_0} + 2\alpha_0\right) E(0,\alpha_0) \\ & - \frac{\epsilon^{-(\alpha_k-\beta-\alpha_0)^2}}{2(1+\rho^2)} \left(\frac{\alpha_k}{\alpha_0} + 1\right) + \frac{\epsilon^{-(\alpha_k-\beta+\alpha_0)^2}}{2(1+\rho^2)} \left(\frac{\alpha_k}{\alpha_0} - 1\right) \\ & + \frac{E(0,\alpha_k-\beta+\alpha_0)}{1+\rho^2} \left(\beta - \frac{1}{2} - \alpha_0{}^2 + \alpha_k{}^2\right) \\ & + \frac{E(0,\alpha_k-\beta-\alpha_0)}{1+\rho^2} \left(\beta + \frac{1}{2} + \alpha_0{}^2 - \alpha_k{}^2\right) \\ & + \frac{\beta}{1+\rho^2} \left[\rho^2\sqrt{\pi} - \frac{\alpha_k{}^2}{\alpha_0} \{F(\alpha_k,-\beta-\alpha_0) - F(\alpha_k,-\beta+\alpha_0)\} \right] \Bigg] \quad \cdots\cdots\cdots\cdots (8) \end{aligned}$$

This equation is rewritten as follows:

$$\begin{aligned} J(\eta_v) = \sqrt{\pi}\, en v_C r_s^2 \Bigg[& \epsilon^{-\alpha_0{}^2} \left[1 - \frac{\epsilon^{-(\alpha_k-\beta)^2}}{1+\rho^2} \left\{ \frac{\alpha_k}{\alpha_0} \sinh 2\alpha_0(\alpha_k-\beta) \right.\right. \\ & \left.\left. + \cosh 2\alpha_0(\alpha_k-\beta) \right\} \right] + \left(\frac{1}{\alpha_0} + 2\alpha_0\right) E(0,\alpha_0) \\ & - \frac{\alpha_0{}^2 + 1/2 - \rho^2\eta_v}{\alpha_0(1+2\rho^2)} E(\alpha_k-\beta-\alpha_0, \alpha_k-\beta+\alpha_0) \\ & + \beta \left[\frac{1}{1+\rho^2} \{E(0,\alpha_k-\beta-\alpha_0) + E(0,\alpha_k-\beta+\alpha_0)\} + \frac{\rho^2\sqrt{\pi}}{1+\rho^2} \right. \\ & \left. - \frac{\eta_v}{\alpha_0} \frac{\rho^2}{1+\rho^2} \{F(\alpha_k,-\beta-\alpha_0) - F(\alpha_k,-\beta+\alpha_0)\} \right] \Bigg], \quad \cdots\cdots\cdots\cdots (9) \end{aligned}$$

where

$$\alpha_0 = \frac{u}{\sqrt{\frac{2kT_i}{M}}}, \qquad \beta = \sqrt{\frac{T_e}{2T_i}}, \qquad \eta_v = \frac{eV}{kT_i},$$

$$\rho^2 = \frac{r_p^2}{r_s^2 - r_p^2} \quad , \qquad \alpha_k^2 = \rho^2 \eta_v \ ,$$

$$E(a, b) = \int_a^b \epsilon^{-x^2} dx \ ,$$

$$F(c, d) = \int_c^\infty \frac{\epsilon^{-(x+d)^2}}{x} dx \ .$$

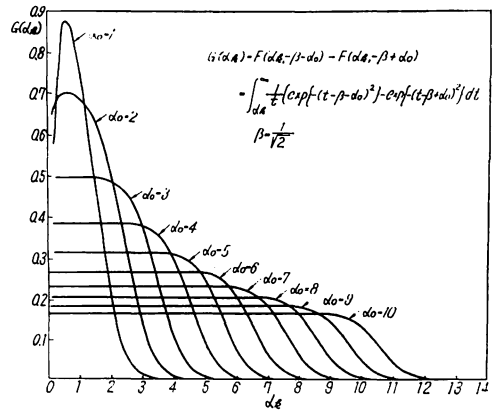


Fig. 1 Diagram of $G(\alpha_k)$ as a function of α_k

Figure 1 shows the graphs of the function $G(\alpha_k) = F(\alpha_k, -\beta-\alpha_0) - F(\alpha_k, -\beta+\alpha_0)$ in the case of $\beta = 1/\sqrt{2}$, that is, $T_e = T_i$ and $\alpha_0 = 1 \sim 10$.

In the retarding potential, as the probe ion current is independent of the sheath, the penetrating electric field is no need of consideration. Therefore, the ion current is expressed as follows:

$$J(\eta_v) = \sqrt{\pi}\, en\, r_p^2\, v_c \left\{ \epsilon^{-\eta_v - \eta_0} \left[\frac{\alpha}{\alpha_0} \sinh(2\alpha\alpha_0) + \cosh(2\alpha\alpha_0) \right] + \frac{1}{\alpha_0} \left(\frac{1}{2} + \eta_0 - \eta_v \right) E(\alpha-\alpha_0, \alpha+\alpha_0) \right\} \quad \cdots\cdots\cdots\cdots \quad (10)$$

This is the same equation as in the electron current.

2.2.3 Theoretical Consideration for Extreme Cases

In the case of $\beta = 0$, that is, if the penetrating electric field is neglected in the accelerating potential,

$$J(\eta_v) = \sqrt{\pi}\, en\, v_c r_s^2 \left[\epsilon^{-\alpha_0^2} \left[1 - \frac{\epsilon^{-\alpha_k^2}}{1+\rho^2} \left\{ \frac{\alpha_k}{\alpha_0} \sinh 2\alpha_0\alpha_k + \cosh 2\alpha_0\alpha_k \right\} \right] + \left(\frac{1}{\alpha_0} + 2\alpha_0 \right) E(0, \alpha_0) \right] - \frac{\alpha_0^2 + 1/2 - \rho^2\eta_v}{\alpha_0(1+\rho^2)} E(\alpha_k - \alpha_0, \alpha_k + \alpha_0) \quad . \quad \ldots\ldots\ldots\ldots\ldots\ldots\ldots\ldots (11)$$

This is the same equation as Eq. (9) in reference (Medicus, 1962).
When $u_0 = 0$ $(\alpha_0 \to 0)$,

$$J(\eta_v) = 2\sqrt{\pi}\, en\, v_c r_s^2 \left[\left\{ 1 - \frac{\epsilon^{-(\alpha_k - \beta)^2}}{1+\rho^2} (1 - \alpha_k\beta) \right\} + \frac{\beta}{1+\rho^2} \left\{ E(0, \alpha_k - \beta)\,(1 + 2\alpha_k^2) + \frac{\sqrt{\pi}}{2} (\rho^2 - 2\alpha_k^2) + 2\beta\alpha_k^2 F(\alpha_k, -\beta) \right\} \right] . \quad \ldots\ldots\ldots\ldots\ldots\ldots\ldots\ldots (12)$$

When $\beta = 0$,

$$J(\eta_v) = 2\sqrt{\pi}\, en\, v_c r_s^2 \left(1 - \frac{\epsilon^{-\alpha_k^2}}{1+\rho^2} \right) = 4\pi r_s^2 \sqrt{\frac{kT_i}{2\pi M}} \left\{ 1 - \frac{r_s^2 - r_p^2}{r_s^2} \exp\left(- \frac{r_p^2 \eta_v}{r_s^2 - r_p^2} \right) \right\} \quad . \quad \ldots\ldots\ldots\ldots\ldots\ldots\ldots\ldots (13)$$

This is the characteristic of the stationary plasma.
Next, when $u_0 \to \infty$ $(\alpha_0 \to \infty)$,

$$J(\eta_v) = \pi\, en\, v_c r_p^2 (\alpha_0 + \beta) \, . \quad \ldots\ldots\ldots\ldots\ldots\ldots\ldots\ldots\ldots\ldots\ldots\ldots\ldots\ldots\ldots\ldots (14)$$

When $\beta = 0$,

$$J(\eta_v) = \pi\, en\, r_p^2 u_0 \, . \quad \ldots\ldots\ldots\ldots\ldots\ldots\ldots\ldots\ldots\ldots\ldots\ldots\ldots\ldots\ldots\ldots\ldots\ldots (15)$$

This shows that the effective surface area of the probe is πr_p^2.

Finally, the sheath radius r_s is calculated from the space charge equation and the kinetic equation of the charged particles in a stationary plasma. The space charge equation is:

$$i = \frac{4}{9} \sqrt{\frac{2e}{M}} \frac{U^{3/2}}{\alpha^2} , \quad \ldots\ldots\ldots\ldots\ldots\ldots\ldots\ldots\ldots\ldots\ldots\ldots\ldots\ldots\ldots\ldots (16)$$

where α^2 is the function of r_s/r_p. The kinetic equation of the charged particle is:

$$i = 4\pi r_s^2\, ne \sqrt{\frac{kT_i}{2\pi M}} \left\{ 1 - \frac{r_s^2 - r_p^2}{r_s^2} \exp\left(- \frac{r_p^2 \eta_v}{r_s^2 - r_p^2} \right) \right\} \quad . \quad \ldots\ldots\ldots\ldots\ldots\ldots\ldots\ldots (17)$$

2.2.4 Summary

The characteristic of the spherical probe analysed in the above sections is exactly the same as in the extreme cases of a stationary plasma and single velocity beams. As the velocity of the space vehicle changes very widely, the analysis in the above sections is usuful, especially in the case where the spherical probe is mounted on a space vehicle. The quantity β in the penetrating electric field is $(T_e/2T_i)^{1/2}$ when the probe voltage is large, but if the probe voltage is very near to the plasma space potential, the analysis of the quantity β is a problem for solution in future (Miyazaki, 1967b).

2.3 Retarding Potential Analyzer

2.3.1 Introduction

A great many ionospheric observations have been carried out till now, and the items of observation are not only the ion density but also the electron density, electron temperature, ion temperature, ion composition, and so on. It is necessary to measure all the ionospheric parameters at the same time especially for detailed comparison between the parameters or for measurement of the ion density when there are many ion species in the ionosphere. Recently experiments were made for comparison of each method (Baker *et al.*, 1966; Heikkila *et al.*, 1968), and the standard method of measurement is desired to be established.

In the following sections is described the method of measuring the electron density, electron temperature, mean ion mass, ion density, ion temperature in the ionosphere at the same time by the use of a single probe assembly which consists of grids and a collector. The DC sweep voltage and the small amplitude of AC voltage are applied to the one of the grids. The plasma parameters are analysed from the DC and AC harmonics components of the currents.

2.3.2 Theoretical Consideration of Current-Voltage Characteristic

(1) Electron density and electron temperature

When the ionospheric and magnetospheric plasma measured by a fast-moving vehicle, the relative velocity between a plasma and a vehicle must be considered in general. But the thermal velocity of electrons in a plasma is much larger than the vehicle velocity. Thus, the relative velocity by the vehicle can be neglected, and the method of analysis of data is the same as in a stationary plasma.

Now at the probe voltage V, the electron current density of the planar probe is expressed as follows:

In the retarding potential,

$$j_e = j_{eo}\exp(-eV/kT_e), \quad \ldots\ldots (18)$$

In the accelerating potential,

$$j_e = j_{eo}, \quad \ldots\ldots (19)$$

where $j_{eo} = N_e e(kT_e/2\pi m)^{1/2}$, that is, the saturation electron current density, N_e is the electron density, T_e the electron temperature, k Boltzmann constant, m the electron mass and e the electron charge. The electron current becomes saturated at the space potential. Although the electron current remains constant in value beyond the space potential for the planar probe, the electron current increases with the probe voltage for the cylindrical or

spherical probe because the sheath around the probe increases. In any way, the electron density is calculated from the electron current at the plasma space potential. In this case, the space potential can be found in the intersection of the two straight lines in the semi-logarithmic plot of the current-voltage curve. However, this method is accompanied with rather big ambiguity. Thus, the AC superposition method is used for measuring the plasma space potential and electron temperature. If the small sinusoidal voltage $a\sin\omega t$ is superimposed on the probe, the AC current of the probe is expressed as:

$$j_\omega = j_{e0}\exp\left(-\frac{eV}{kT_e}\right) \times 2I_1\left(\frac{ea}{kT_e}\right), \quad \cdots\cdots\cdots\cdots\cdots\cdots\cdots\cdots\cdots\cdots (20)$$

where I_1 means the modified Bessel function of order one. In the case of two kinds of small amplitude, a_1 and a_2, superimposed, the electron temperature is obtained by the current ratio, that is,

$$r = \frac{I_1(ea_1/kT_e)}{I_1(ea_2/kT_e)} \cdot \quad \cdots\cdots\cdots\cdots\cdots\cdots\cdots\cdots\cdots\cdots\cdots\cdots\cdots\cdots\cdots\cdots (21)$$

The method of analyses of data for cylindrical and spherical cases are the same as in the planar electrode case.

(2) Ion density, ion temperature and ion mass

In the case of measurement of quantities concerning ions in the ionospheric and magnetospheric plasma by fast-moving vehicle, the relative velocity between the vehicle and plasma must be considered, because the vehicle velocity is comparable with or larger than the ion thermal velocity as shown in Table 1 in which M^+ means the atomic or molecular weight of ion.

Table 1 Maximum probable velocities of ions and electrons (km/sec)

	T(°K)	500	1000	2000	3000	4000
M^+	1	2.87	4.06	5.74	7.04	8.12
	4	1.44	2.03	2.87	3.52	4.06
	16	0.72	1.02	1.44	1.76	2.03
	30	0.52	0.74	1.05	1.28	1.48
Electron		123.	174.	246.	302.	348.

a) Planar electrode

Consider the current-voltage characteristic curve of ion with the relative velocity. Now, suppose that the planar probe is stationary, and the plasma flows with the drift velocity v_R. We choose the coordinate system as shown in Fig. 2. The probe ion current density at the probe voltage V is expressed as the following integrals:

$$j_i = N_i e \int_{v_V}^{\infty}\int_{-\infty}^{\infty}\int_{-\infty}^{\infty} v_x f(v_x, v_y, v_z)dv_x dv_y dv_z , \quad \cdots\cdots\cdots\cdots\cdots (22)$$

where $Mv_v^2/2 = eV$, and the distribution function is:

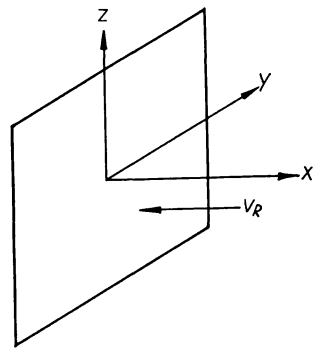


Fig. 2 Coordinate system

$$f(v_x, v_y, v_z) = \left(\frac{M}{2\pi kT_i}\right)^{3/2} \exp\left[-\frac{M}{2kT_i}\{(v_x - v_R)^2 + v_y^2 + v_z^2\}\right] \quad \cdots\cdots\cdots\cdots \quad (23)$$

Therefore, the result is:

$$j_i = j_{i0}\left[\exp\left\{-\left(\frac{v_V - v_R}{v_p}\right)^2\right\} + \frac{\sqrt{\pi}\, v_R}{v_p}\left\{1 - \mathrm{erf}\left(\frac{v_V - v_R}{v_p}\right)\right\}\right] , \quad \cdots\cdots\cdots\cdots \quad (24)$$

where $v_p = (2kT_i/M)^{1/2}$ is the most probable velocity, and

$$j_{i0} = N_i e \sqrt{\frac{kT_i}{2\pi M}} ,$$

$$\mathrm{erf}(x) = \frac{2}{\sqrt{\pi}} \int_0^x \exp(-y^2)\, dy .$$

In the ionosphere, there exist many species of ions, that is, there mainly exist O_2^+ and NO^+ in the lower part of the ionosphere, while in the upper F layer, O^+ is the main constituent of ion, and the constituent changes from O^+ to He^+ and H^+ in the topside ionosphere (Bates and Patterson, 1962; Nagata and Tohmatsu, 1973). Therefore, the total ion current is the sum of such components, that is, $J_i = \Sigma j_i$.

The topside ionosphere is roughly the region of two or three kinds of ions in existence.

Next consider the case of two ions. Figure 3 shows the characteristic curves of ion current in the case of 30 and 16 in molecular weight. The figures on the curves mean the ratio of 30 to 16. It is very difficult to determine the density ratio by this graph. But the values at $V = 0$ show the same in spite of the mixed ratio of the ions, that is, $v_R \gg v_p$, the total ion current is expressed as the following approximate equation:

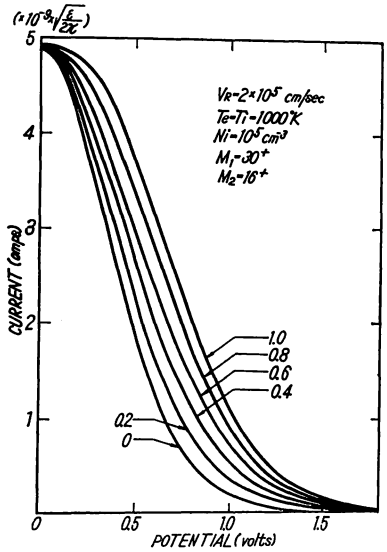


Fig. 3 Characteristic curves of ion current (Planar trap)

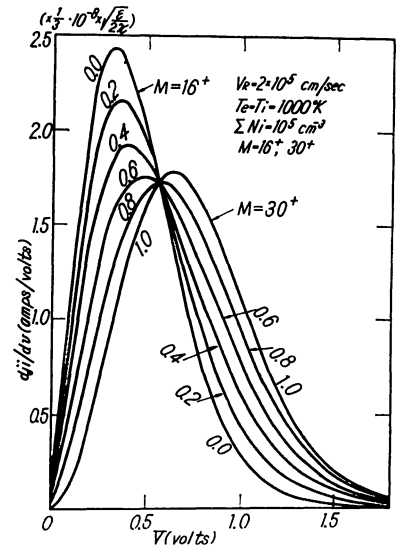


Fig. 4 Characteristic curves of the first derivative of ion current (Planar trap)

$$J_{i0} \approx \Sigma j_{i0} 2\sqrt{\pi}\,\frac{v_R}{\sqrt{2kT_i/M}} = N_i e v_R \,. \qquad \text{..... (25)}$$

Next, calculate the derivative of the ion current with respect to the voltage. The result is:

$$\frac{dj_i}{dV} = -j_{i0}\left(\frac{v_V}{v_p}\right)^2 \frac{1}{V} \exp\left\{-\left(\frac{v_V - v_R}{v_p}\right)^2\right\}$$

$$= -\frac{e^2 N_i}{\sqrt{2\pi k T_i M}} \exp\left\{-\left(\sqrt{\frac{eV}{kT_i}} - \frac{v_R}{\sqrt{2kT_i/M}}\right)^2\right\}, \qquad \text{..... (26)}$$

and

$$\frac{dJ_i}{dV} = \Sigma \frac{dj_i}{dV}\,, \qquad \text{..... (27)}$$

This characteristic curve is shown in Fig. 4 on the same assumption as in Fig. 3. By this graph, the peak value and its position change remarkably with the mixed ratio of ions. For example, Fig. 5 shows the case of molecular weight 1 and 4, Fig. 6 the case of 4 and 16. Figure 7 shows the characteristic curves of dj_i/dV of molecular weight 1, 4, 16 and 30. The peaks appear at the voltage $V_{max} = M_i v_r^2/2e$ according to the ion mass. When more than two kinds of ions exist, the peaks for the mixed ions appear at V_{max} relating to ion constituent or the peak appears between each V_{max} as shown in Figs. 4, 5 and 6.

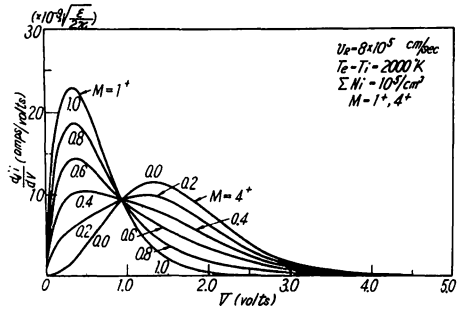


Fig. 5 Characteristic curves of the first derivative of ion current (Planar trap)

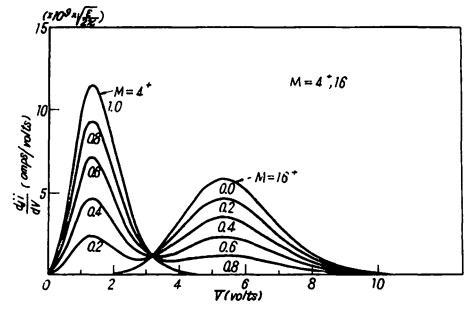


Fig. 6 Characteristic curves of the first derivative of ion current (Planar trap)

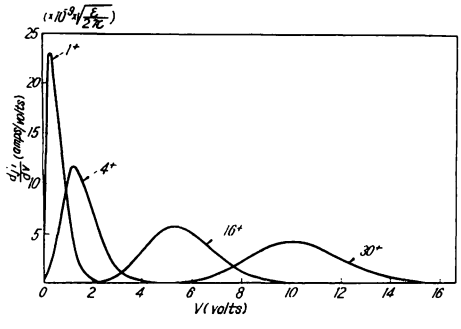


Fig. 7 Characteristic curves of the first derivative of ion current (Planar trap)

Anyhow, the ion species of ions exist, the partial ion densities and ion temperatures are determined by the following equations:

$$\begin{cases} J_{i0} = F_1(N_{i1},\ N_{i2},\ N_{i3},\ T_i), \\ \left(\dfrac{dJ_i}{dV}\right)_{V=V_1} = F_2(N_{i1},\ N_{i2},\ N_{i3},\ T_i), \\ \left(\dfrac{dJ_i}{dV}\right)_{V=V_2} = F_3(N_{i1},\ N_{i2},\ N_{i3},\ T_i), \\ \left(\dfrac{dJ_i}{dV}\right)_{V=V_3} = F_4(N_{i1},\ N_{i2},\ N_{i3},\ T_i) \end{cases} \quad \cdots\cdots\cdots\cdots\cdots\cdots\cdots\cdots \quad (28)$$

where J_{io} is the total ion current at $V = 0$, and $(dj_i/dV)_{V=V_1,V_2,V_3}$ are the values of dJ_i/dV at each V_{max} relating to the ion mass. In the cases of 30 and 32, it is useful to assume the mean ion molecular weight $\bar{M}$, and the derivative of the ion current with respect to the

voltage is:

$$\frac{dJ_i}{dV} = -J_{i0}\frac{e}{kT_i}\exp\left\{-\left(\sqrt{\frac{eV}{kT_i}}-\frac{v_R}{\sqrt{2kT_i/\bar{M}}}\right)^2\right\} \quad \cdots\cdots (29)$$

The mean molecular weight $\bar{M}$ and ion temperature T_i are calculated from the peak value and position of the peak by the following equation:

$$\bar{M} = \frac{2eV_{max}}{v_R^2}, \quad \cdots\cdots (30)$$

$$\frac{-(dJ_i/dV)}{J_{i0}} = \frac{e}{kT_i}. \quad \cdots\cdots (31)$$

b) Spherical and cylindrical electrodes

Now, suppose the probing electrode is stationary, and a plasma flows with the drift velocity u_o.

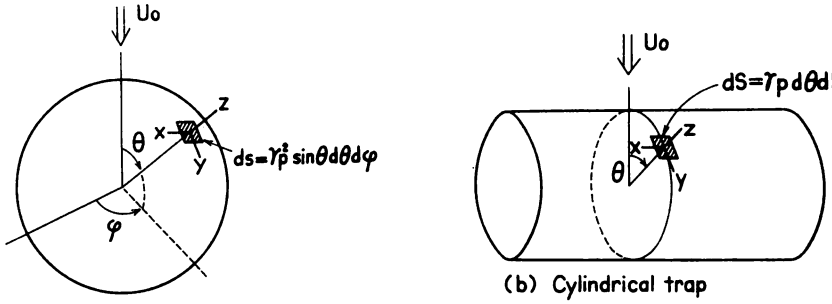


Fig. 8 Coordinate systems

In this section, let us consider the current-voltage characteristic curve of ions with the drifting Maxwellian velocity distribution. We choose the coordinate system as shown in Fig. 8. The collector ion current at the retarding potential V is expressed as the following integrals (Medicus, 1962; Kanal, 1964).

Spherical case

$$i_i = A\int_0^{2\pi}\int_0^{\pi} i_{i-ds}\, r_p^2 \sin\theta\, d\theta\, d\varphi. \quad \cdots\cdots (32)$$

Cylindrical case

$$i_i = A\int_0^{l}\int_0^{2\pi} i_{i-ds}\, r_p\, d\theta\, dl, \quad \cdots\cdots (33)$$

where A is the transparency coefficient of the grids G1 and G2, r is the probe radius, and $i_{i\text{-}ds}$ is the ion current flowing into the surface element ds. The shape of the surface element ds is considered to be planar because its area is infinitely small. Therefore, the ion current $i_{i\text{-}ds}$ is calculated as in the case of planar probe, that is,

$$i_{i-ds} = N_i e \int_{v_V}^{\infty} \int_{-\infty}^{\infty} \int_{-\infty}^{\infty} v_z f(v_x, v_y, v_z) dv_x\, dv_y\, dv_z, \quad \cdots\cdots\cdots\cdots\cdots (34)$$

where N_i is the ion density, e is the unit charge, and f is the velocity distribution function,

$$f(v_x, v_y, v_z) = \left(\frac{M}{2\pi k T_i}\right)^{3/2} \exp\left[-\frac{M}{2kT_i} \; v_x^2 + (v_y + u_0 \sin\theta)^2 + (v_z - u_0 \cos\theta)^2 \right] \quad \cdots (35)$$

and

$$\frac{1}{2} M v_V^2 = eV, \quad \cdots\cdots\cdots\cdots\cdots\cdots\cdots\cdots\cdots\cdots\cdots\cdots\cdots\cdots\cdots (36)$$

where v_V is the equivalent ion velocity, M is the ion mass, T_i is the ion temperature and k is the Boltzmann constant.

The results of calculation are as follows:

i) Spherical case

$$i_i(V) = A\sqrt{\pi}\, e N_i r_p^2 v_p \left[\exp(-\alpha^2 - \alpha_0^2) \left\{ \frac{\alpha}{\alpha_0} \sinh(2\alpha\alpha_0) + \cosh(2\alpha\alpha_0) \right\} + \left(\frac{1}{2\alpha_0} + \alpha_0 - \frac{\alpha^2}{\alpha_0} \right) E(\alpha - \alpha_0, \alpha + \alpha_0) \right], \quad \cdots\cdots (37)$$

where

$$\alpha_0 = \frac{u_0}{v_p}, \quad \alpha = \sqrt{\frac{eV}{kT_i}}, \quad v_p = \sqrt{\frac{2kT_i}{M}}, \quad E(a, b) = \int_a^b \exp(-x^2) dx.$$

The first and second derivatives of the ion current with respect to the voltage are as follows:

$$\frac{di_i}{dV} = -\frac{A\sqrt{\pi}\, e^2 N_i r_p^2 v_p}{kT_i \alpha_0} E(\alpha - \alpha_0, \alpha + \alpha_0), \quad \cdots\cdots\cdots\cdots\cdots\cdots (38)$$

$$\frac{d^2 i_i}{dV^2} = \frac{A\sqrt{\pi}\, e^3 N_i r_p^2 v_p}{k^2 T_i^2 \alpha\alpha_0} \exp(-\alpha^2 - \alpha_0^2) \sinh(2\alpha\alpha_0). \quad \cdots\cdots\cdots\cdots\cdots (39)$$

ii) Cylindrical case

$$i_i(V) = 4AeN_i r_p l v_p \exp(-\alpha^2 - \alpha_0^2) \int_0^{\infty} \alpha_V^2 \exp(-\alpha_V^2) I_0(Z) d\alpha_v, \quad \cdots\cdots\cdots (40)$$

where

I_0: Modified Bessel function of order zero, $Z = 2\alpha_0(\alpha_V^2 + \alpha^2)^{1/2}$, $\alpha_V = v_V / v_p$.

The first derivative of the ion current with respect to the voltage is as follows:

$$\frac{di_i}{dV}=\frac{4Ae^2N_ir_plv_p}{kT_i}\exp(-\alpha^2-\alpha_0^2)\int_0^{\infty}\alpha_V^2\quad\exp(-\alpha_V^2)\quad\left\{2\alpha_0^2\frac{I_1(Z)}{Z}-I_0(Z)\right\}d\alpha_V. \qquad \cdots\cdots\cdots\cdots\cdots\cdots\cdots\cdots\cdots\cdots \quad (41)$$

The total ion currents are:

$$I_i(V)=\sum_{1,2,\ldots}i_i(V),\quad \frac{dI_i}{dV}=\sum_{1,2,\ldots}\frac{di_i}{dV},\quad \frac{d^2I_i}{dV^2}=\sum_{1,2,\ldots}\frac{d^2i_i}{dV^2} \qquad \cdots\cdots\cdots\cdots \quad (42)$$

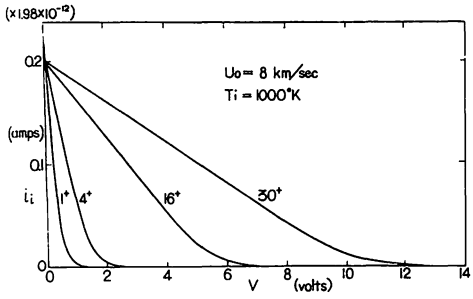


Fig. 9 Characteristic curves of ion current (Spherical trap)

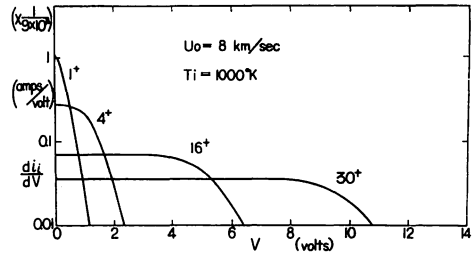


Fig. 10 Characteristic curves of the first derivative of ion current (Spherical trap)

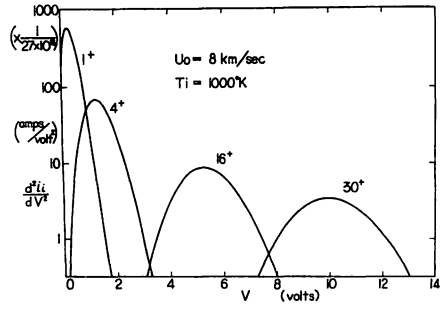


Fig. 11 Characteristic curves of the second derivative of ion current (Spherical trap)

Figure 9, 10 and 11 show the ion characteristic curves of $i_i(V)$, $di_i(V)/dV$ and $d^2i_i(V)/dV^2$ with the molecular weight 1^+, 4^+, 16^+ and 30^+ in spherical trap. Figure 12 shows variation due to the ion temperature in the case of the second derivative of ion current in the spherical trap. Figure 13 shows the characteristic curves of $d^2I_i(V)/dV^2$ in the case where there exist three kinds of ions, 4^+, 16^+ and 30^+ in the spherical trap. The figures on the curves mean the percentage of existence of the ion species, 4^+, 16^+ and 30^+. Figures 14 and 15 show the ion characteristic curves of $i_i(V)$ and $di_i(V)/dV$ of the cylindrical trap. Figure 16 shows the

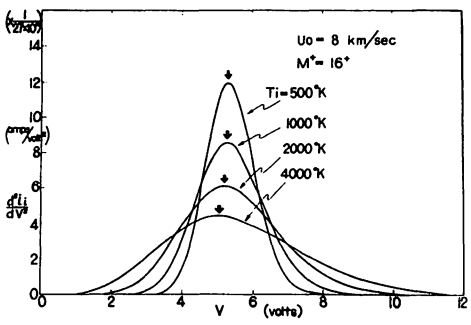


Fig. 12 Variation of characteristic curves of the second derivative of ion current due to the ion temperature (Spherical trap)

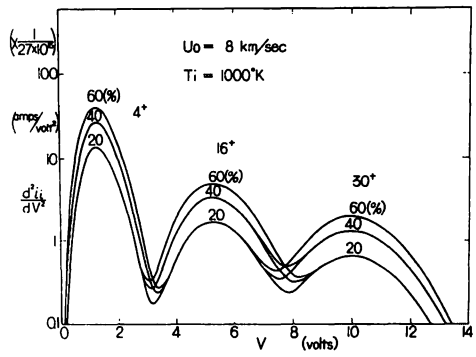


Fig. 13 Characteristic curves of the second derivative of ion current (Spherical trap)

variation of the first derivative ion current due to ion temperature in the cylindrical trap. Figure 17 shows the characteristic curves of $dI_i(V)/dV$ in existing three kinds of ions, 4^+, 16^+ and 30^+ in the cylindrical trap.

In calculating the graphs described above, the unit ion density (N_i = 1 cm^{-3}) and unit length (r_p = 1 cm, l = 1 cm) are chosen. Generally, current maximum appear at different positions according to the ion mass in the characteristic curve of the second derivative of ion current in the spherical trap as shown in Fig. 13 and of the derivative of ion current in the cylindrical trap as shown in Fig. 17.

Next we calculate the position of the peak. In the spherical trap, the value of α, which relates to the position of the peak in the second derivative curve, is obtained from the root of the following equation:

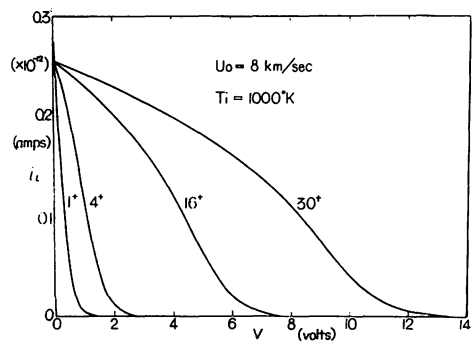


Fig. 14 Characteristic curves of ion current (Cylindrical trap)

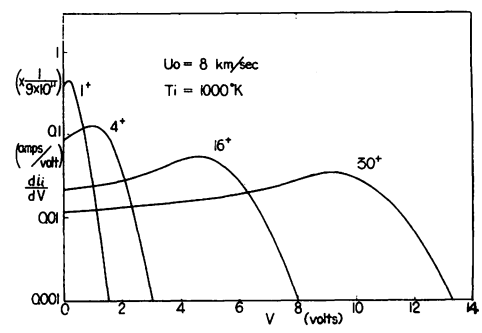


Fig. 15 Characteristic curves of the first derivative of ion current (Cylindrical trap)

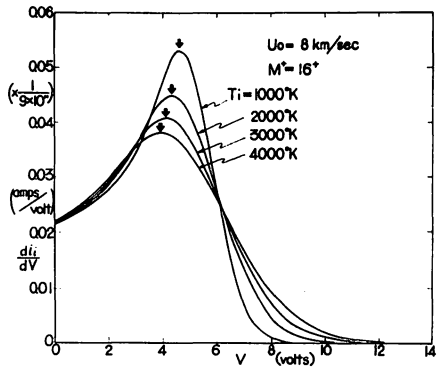


Fig. 16 Variation of characteristic curves of the first derivative of ion current due to the ion temperature (Cylindrical trap)

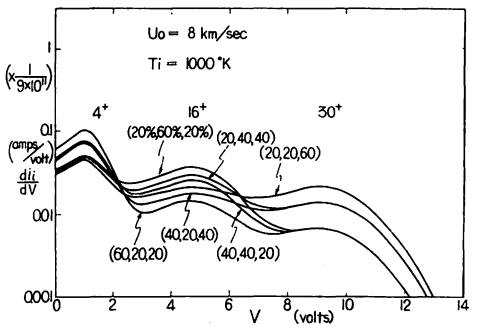


Fig. 17 Characteristic curves of the first derivative of ion current (Cylindrical trap)

$$\frac{d^3 i_i}{dV^3} = \frac{A\sqrt{\pi}e^4 N_i r_p^2 v_p}{4k^3 T_i^3 \alpha_0}\left[\left(-\frac{1}{\alpha^3}-\frac{2}{\alpha}+\frac{2\alpha_0}{\alpha^2}\right)\exp\{-(\alpha_0-\alpha)^2\}\right.$$
$$\left.+\left(\frac{1}{\alpha^3}+\frac{2}{\alpha}+\frac{2\alpha_0}{\alpha^2}\right)\exp\{-(\alpha_0+\alpha)^2\}\right] = 0, \quad \cdots\cdots\cdots\cdots\cdots\cdots \quad (43)$$

that is,

$$\left(-\frac{1}{\alpha^3}-\frac{2}{\alpha}+\frac{2\alpha_0}{\alpha^2}\right)\exp\{-(\alpha_0-\alpha)^2\}+\left(\frac{1}{\alpha^3}+\frac{2}{\alpha}+\frac{2\alpha_0}{\alpha^2}\right)\exp\{-(\alpha_0+\alpha)^2\} = 0. \quad \cdots \quad (44)$$

The above equation can not be solved with an analytical form. But, for $\alpha_0 \gg 1$, the equation can be solved approximately. That is,

$$\alpha \fallingdotseq \alpha_0 - \frac{1}{2\alpha_0} - \frac{1}{4\alpha_0^3} + \cdots\cdots \quad \cdots\cdots\cdots\cdots\cdots\cdots\cdots\cdots\cdots\cdots \quad (45)$$

In the cylindrical trap, the value of α is obtained from that the root of the second derivative equation equals to zero.

$$\frac{d^2 i_i}{dV^2} = \frac{4Ae^3 N_i r_p l v_p}{k^2 T_i^2}\exp(-\alpha^2-\alpha_0^2)\int_0^\infty \alpha_V^2 \exp(-\alpha_V^2)\left\{4\alpha_0^4\frac{I_2(Z)}{Z^2}\right.$$
$$\left.-4\alpha_0^2\frac{I_1(Z)}{Z}+I_0(Z)\right\}d\alpha_V = 0, \quad \cdots\cdots\cdots\cdots\cdots\cdots\cdots\cdots\cdots\cdots \quad (46)$$

where I_0, I_1 and I_2: Modified Bessel functions of order zero, one and two.
That is,

$$\int_0^\infty \alpha_V^2 \exp(-\alpha_V^2)\left\{4\alpha_0^4\frac{I_2(Z)}{Z^2}-4\alpha_0^2\frac{I_1(Z)}{Z}+I_0(Z)\right\}d\alpha_V = 0. \quad \cdots\cdots\cdots\cdots \quad (47)$$

The above equation can be solved approximately for $\alpha_0 \gg 1$.

That is,

$$\alpha^2 \fallingdotseq \alpha_0^2 - 1.077\alpha_0. \quad \cdots\cdots (48)$$

Thus the ion density and ion temperature can be obtained from the peak value and its position.

When there is no peak in the characteristic curve, the ion density and temperature must be solved by simultaneous equations as in the planar retarding potential trap method.

2.3.3 Method of Measurement

As a single planar probe assembly is used Faraday cup type electrode system as shown at the left in Fig. 18. This electrode consists of two circular grids, G1 and G2 and a collector

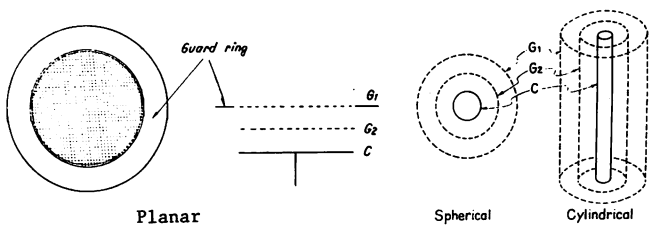


Fig. 18 Structures of retarding potential trap

C. There is a guard ring of the same area as the inner surface around the grid G1 in order to avoid the edge effect of the planar probe. DC sweep voltage is applied to the grid G1. The negative voltage is applied to the collector which collects only the ions passing through the grids. The large negative voltage is applied to the second grid G2, which prevents the photo-emission radiating from the collector surface. As the current-voltage characteristic of G1 is considered to be mainly that of the electron current because the ion current is small, the quantities concerning electrons can be determined by the characteristic curve of the grid G1. The quantities concerning ions can be determined by the characteristic curve of the collector. Figure 18 also shows the schematic illustrations of spherical and cylindrical retarding potential traps which consist of two concentric shape grids, G1 and G2.

When small AC voltage $a\sin\omega t$ is superimposed on DC voltage to the grid, the total ion current of the collector is expressed as:

$$\begin{aligned} i_i &= f(V + a\sin\omega t) \\ &= f(V) + \frac{a^2}{4}\frac{d^2 f(V)}{dV^2} + \frac{a^4}{64}\frac{d^4 f(V)}{dV^4} + \cdots\cdots \\ &\quad + \left\{ a\frac{df(V)}{dV} + \frac{a^3}{8}\frac{d^3 f(V)}{dV^3} + \cdots\cdots \right\} \sin\omega t \\ &\quad - \left\{ \frac{a^2}{4}\frac{d^2 f(V)}{dV^2} + \frac{a^4}{48}\frac{d^4 f(V)}{dV^4} + \cdots\cdots \right\} \cos 2\omega t \end{aligned}$$

$$-\left\{\frac{a^3}{24}\frac{d^3f(V)}{dV^3}+\cdots\cdots\right\}\sin 3\omega t$$

$$+\left\{\frac{a^4}{192}\frac{d^4f(V)}{dV^4}+\cdots\cdots\right\}\cos 4\,\omega t+\cdots\cdots \quad \cdots\cdots\cdots\cdots\cdots\cdots \quad (49)$$

Therefore, if the amplitude a is small enough, the first derivative of ion current is measured from the ω component of AC current, and the second derivative of ion current is measured from the 2ω component of AC current. However, for arbitrary magnitude of a, the ω and 2ω components of AC current are as follows:

$$\omega : \frac{1}{\pi}\int_{-\pi}^{\pi} f(V+a\sin\omega t)\sin\omega t\, d(\omega t), \quad \cdots\cdots\cdots\cdots\cdots\cdots \quad (50)$$

$$2\omega: \frac{1}{\pi}\int_{-\pi}^{\pi} f(V+a\sin\omega t)\cos 2\omega t\, d(\omega t), \quad \cdots\cdots\cdots\cdots\cdots\cdots \quad (51)$$

For example, variations of the second derivative of ion current due to amplitude a in the spherical trap are shown in Fig. 19. The ordinate is normalized with a^{-2} in each curve. From

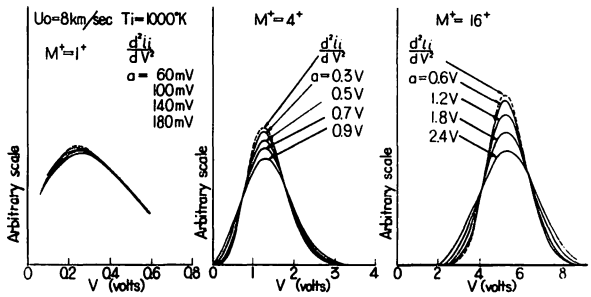


Fig. 19 Variation of characteristic curves of the second derivative of ion current due to the magnitude of AC amplitude a (Spherical trap)

the graph, it is clear that the position of the peak does not change with the amplitude a less than one-tenth of DC voltage. The two modes of voltage are applied to the grid G1 successively. These are DC mode of only DC sweep voltage and (AC + DC) mode, that is, DC sweep voltage superimposed by small amplitude AC voltage. We detect the DC, AC-ω and AC-2ω components of electron current flowing into G1, and the AC-ω and AC-2ω components are proportional to the first and second derivatives of electron current with respect to voltage, di_i/dV and d^2i_i/dV^2. Similarly detect the DC, AC-ω and AC-2ω components of ion current flowing into the collector C. Thus the electron density, electron temperature, ion density, ion temperature, and ion mass are calculated from these current components.

2.3.4 Summary

The above described method of measurement of the basic parameters in the ionosphere with self-consistence and accuracy by the use of the planar, spherical and cylindrical types of retarding potential trap. The merits in use of the spherical trap are that it is omnidirectional and has no edge effect, but the demerit is difficulty in making exactly concentric spherical electrodes. On the other hand the merit in use of the cylindrical trap is that it is easy to make exact configuration of the cylindrical electrode, while the demerit is that the shape of peak in the ion characteristic curve is not steeper than that of the spherical probe (Miyazaki, 1967a; Miyazaki and Mori, 1968).

2.4 Resonance Probe

2.4.1 Introduction

Space charge layer, ion sheath, usually exists around the boundary in a plasma. The electrical property is affected by the existence of the sheath. Therefore, the sheath must be considered in discussing the problems of interaction between bounded plasma and electromagnetic field. Especially it becomes an important problem in the case of satellite- and rocket-borne radio wave measurements because that the sheath changes severely as the vehicle potential is altered very widely by the ambient plasma and the vehicle conditions. For example, Taylor *et al.* (1965) reported spacecraft potential was changed from 0 to −20 V, Brinton *et al.* (1968) stated that the observed change of the OGO 1 spacecraft potential was from 0 to −9 V in the plasmasphere. Hanson *et al.* (1964) observed a satellite of −20 V, and Knudsen and Sharp (1964) observed a potential of −15 V. ATS 5 could charge to potentials as high as 10,000 V during eclipse, and as high as 200 V in sunlight (DeForest, 1972).

Experimental and theoretical studies on electrical properties of the sheath-plasma system have been carrying out by many researchers (Takayama *et al.*, 1960; Kaiser, 1962; Ikegami and Takayama, 1963; Ichikawa, 1963; Uramoto *et al.*, 1963; Pavkovich and Kino, 1963; Pavkovich, 1963; Crawford and Harp, 1965; Harp and Crawford, 1964; Pyati and Weil, 1965; Dote and Ichimiya, 1965, 1967; Crawford, 1965; Balmain, 1966; Buckley, 1966, 1967; Davies, 1966; Ikeji and Takayama, 1966; Baker and Despain, 1966; Kostelnicek, 1968; Kaiser and Tunaley, 1968; Heikkila, 1969; Balmain and Oksiutik, 1969; Holt and Trøim, 1969). In order to treat these problems, there are mainly three methods, that is, dielectric media approximation, hydrodynamic approximation and the method to solve the simultaneous equations of Boltzmann's equation and Maxwell's equation. Although the third method is perfect in view of theoretical point, the results are not only expressed in analytical form but also they need tedious numerical calculations. Thus the analysis is carried out to limited cases (Buckley, 1966, 1967). The hydrodynamic approximation also needs complex calculation in plasma and sheath region (Balmain, 1966; Ikeji and Takayama, 1966; Kostelnicek, 1968; Holt and Trøim, 1969). In the former dielectric media approximation (Dote and Ichimiya, 1965, 1967; Miyazaki, 1968, 1969; Balmain and Oksiutik, 1969), the analysis of the radio frequency probe is treated by rather simple method, for example, a sheath collapse condition, a vacuum simulation for large negative probe potential, or average electron density approximation in the sheath region till now.

Here the various properties of the sheath-plasma impedance are analysed by using a continuous sheath model. And a plasma is treated as dielectric media by using Newtonian model.

2.4.2 Model of Ion Sheath Profile

At first, the typical three cases of the ion sheath profile in one dimension as shown in Fig. 20 are considered, that is (a) the case of vacuum in the half region of the sheath, (b) the case of half electron density in the sheath, (c) the case that electron density decreases as a linear function in the sheath.

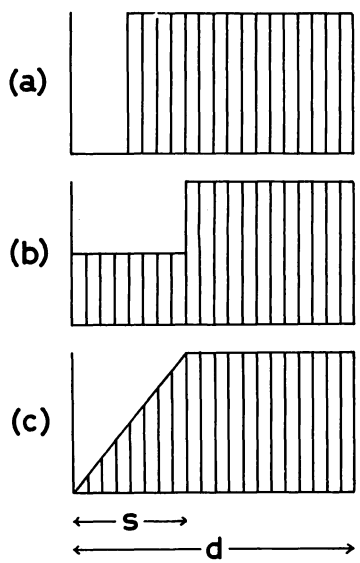


Fig. 20 Sheath profiles

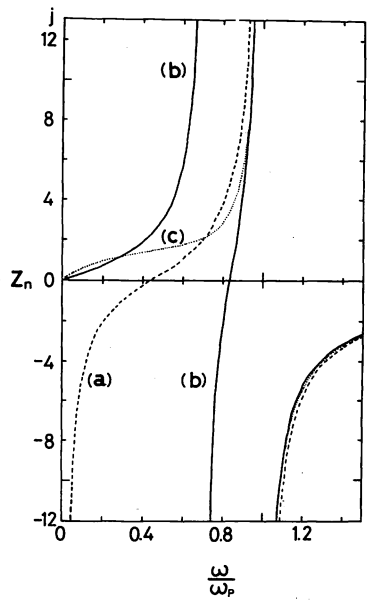


Fig. 21 Impedance characteristics

Now permitivity of a plasma is given by,

$$K_O = 1 - \omega_p^2/(\omega^2 - j\omega\nu), \qquad \cdots\cdots (52)$$

where ω_p is the electron plasma angular frequency and ν is the mean collision frequency.

The sheath-plasma impedance is expressed as follows:

Case (a)

$$Z = \frac{d - s/2}{j\omega\epsilon_0(1-\omega_p^2/\omega^2)} + \frac{s}{2j\,\omega\epsilon_0}, \qquad \cdots\cdots (53)$$

Case (b)

$$Z = \frac{d - s}{j\omega\epsilon_0(1-\omega_p^2/\omega^2)} + \frac{s}{j\omega\epsilon_0\{1-\omega_p^2/(2\omega^2)\}}, \qquad \cdots\cdots (54)$$

Case (c)

$$Z = \frac{d - s}{j\omega\epsilon_0(1-\omega_p^2/\omega^2)} - \frac{\omega S}{j\omega_p^2\epsilon_0}\ln\left|1-\frac{\omega_p^2}{\omega^2}\right|, \qquad \cdots\cdots (55)$$

where s is the sheath thickness, d is the total distance and ϵ_0 is the dielectric constant in free space. For the brevity it is assumed that $\nu = 0$ and the surface area is unity.

It is convenient to define normalized impedance Z_n.

$$Z_n \equiv \omega_p \epsilon_0 Z. \quad \ldots\ldots\ldots\ldots\ldots\ldots\ldots\ldots\ldots\ldots\ldots\ldots\ldots\ldots\ldots\ldots\ldots\ldots \quad (56)$$

Figure 21 shows the total normalized impedance of each case. Here it is assumed that $s = 2$ and $d = 5$. This graph indicates that the three cases are different from each other, especially the case (c) has no minimum or maximum below plasma frequency. Thus the simple density profile in the sheath region does not give the correct sheath-plasma impedance.

Generally, the Langmuir-Mott-Smith theory, the formulae of the space charge equation and particle trajectory equation are used to calculate the sheath thickness (Langmuir and Blodgett, 1923, 1924). The sheath thickness of planar probe can be solved analytically, but numerical calculations must be needed for spherical and cylindrical cases.

By the space charge equation, the potential profile is expressed as three-halves law. By assuming that electrons have Maxwell-Boltzmann distribution, the potential profile is proportional to $\exp(-r/\lambda_d)$, where λ_d is the electronic Debye length. But the exact potential profile is not presented by a simple expression, and so here the parabolic distribution is assumed and is smoothly continued from a sheath region to a plasma region in order to simplify the succeeding numerical calculation.

Now the potential at a distance x is,

$$V(x) = -V_p x^2/s^2, \quad \ldots\ldots\ldots\ldots\ldots\ldots\ldots\ldots\ldots\ldots\ldots\ldots\ldots\ldots\ldots\ldots\ldots\ldots \quad (57)$$

where V_p is the probe potential and s is the sheath thickness. And the electron density is expressed by Boltzmann's law.

$$n_{ex} = n_e \exp\{-eV(x)/kT_e\}, \quad \ldots\ldots\ldots\ldots\ldots\ldots\ldots\ldots\ldots\ldots\ldots\ldots\ldots\ldots\ldots\ldots \quad (58)$$

where n_e is the ambient electron density, e is the electron charge, T_e is the electron temperature and k is the Boltzmann constant.

2.4.3 Impedance/Admittance Profile of Sheath Plasma System

(1) Planar probe

The distance of the two planar probes is d and the sheath thickness is s as shown in Fig. 22. The total impedance between two parallel probes is expressed as the sum of the sheath impedance and the plasma impedance.

The sheath impedance Z_s is

$$Z_s = \int_0^s \frac{dx}{j\omega\epsilon_0 \left\{1 - \dfrac{n_{ex}e^2}{m\epsilon_0(\omega^2 - j\omega\nu)}\right\}}, \quad \ldots\ldots\ldots\ldots\ldots\ldots\ldots\ldots\ldots\ldots\ldots\ldots\ldots\ldots\ldots\ldots \quad (59)$$

where m is the electron mass.

The mean collision frequency in the sheath region is decided by the relation of the mean free path, the sheath thickness and other parameters. If the sheath thickness is smaller than the mean free path, the mean collision frequency is very small in the sheath, and if the

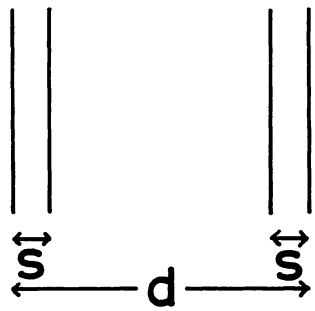


Fig. 22 Planar probe configuration

sheath thickness is larger, the mean collision frequency is near that of the ambient plasma. And if the collision frequency in the sheath is assumed to be the same as in the ambient plasma, the impedance characteristic shows no special property except the case of low probe potential. Here the mean collision frequency in the sheath is assumed to be proportional to the local electron density in the convenient way although this assumption may not correct in exact physical meaning. Thus,

$$\nu = \nu_e n_{ex}/n_e, \quad \ldots\ldots (60)$$

where ν_e is the mean collision frequency in the ambient plasma.

Next the plasma impedance is,

$$Z_p = \frac{d-s}{j\omega\epsilon_0 \{1-\omega_p^2/(\omega_p^2 - j\omega\nu_e)\}} \quad \ldots\ldots (61)$$

And the total normalized impedance is obtained by using the normalizing factor $\omega_p\epsilon_0$.

$$Z_n = \omega_p\epsilon_0(2Z_s + Z_p). \quad \ldots\ldots (62)$$

It is convenient to use the admittance, the reciprocal of impedance because that admittance characteristic is directly obtained in usual experiments. And the admittance is obtained by numerical calculations with computer.

Figure 23 shows the normalized admittance against the normalized frequency ω/ω_p in the case of $n_e = 10^{12}$ m^{-3}, $T_e = 0.1$ eV, $\nu_e/\omega_p = 0.01$, $d = 0.2$ m and $V_p = 0.1$, 0.5 and 2.0 V. The characteristic curve in the case of $V_p = 0.1$ V, is almost the same as the plasma characteristic itself except the region near 0.61 ω/ω_p. And there are a maximum and a minimum around 0.61 ω/ω_p. In the case of $V_p = 0.5$ V, the maximum and minimum shift to the lower frequency comparing with the case of $V_p = 0.1$ V. The first minimum is attributed to the antiresonance of the plasma in the sheath, on the other hand, the second minimum is attributed to the plasma resonance in the ambient plasma. And there is a maximum between two minima, this maximum is the sheath resonance. As the probe potential increases, the first minimum shifts to the lower frequency and finally it disappears, on the other hand, the sheath resonance shifts to the lower frequency at first, then, to the higher frequency, and the shape becomes more sharp.

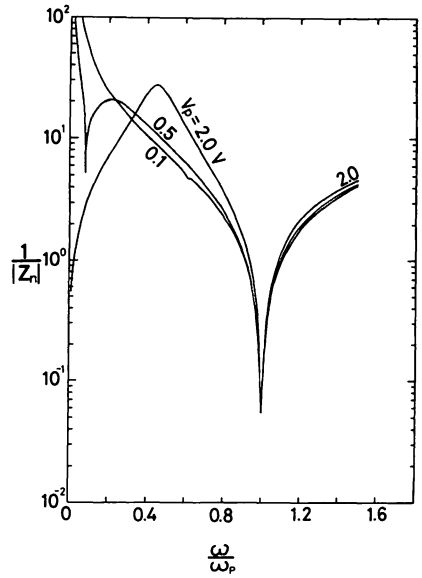


Fig. 23 Admittance characteristic curves

a) Admittance variation by the electron density

Figure 24 shows the relations between the resonant frequency and the probe potential, the dotted line indicates the first minimum and the solid lines indicate the maximum, that is, the sheath resonance. The minimum frequency characteristic does not depend on the electron density. The reason is that the electron density distribution in the sheath is similar shape although the electron density changes, and so the antiresonance due to the plasma in the sheath region does not change. The frequency characteristic curve of the sheath resonance is of concave shape. As the electron density increases, the resonant frequency

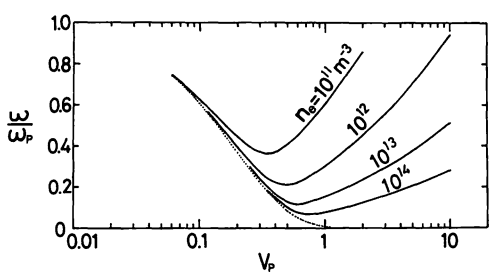


Fig. 24 Sheath resonant and antiresonant frequency variation by the electron density

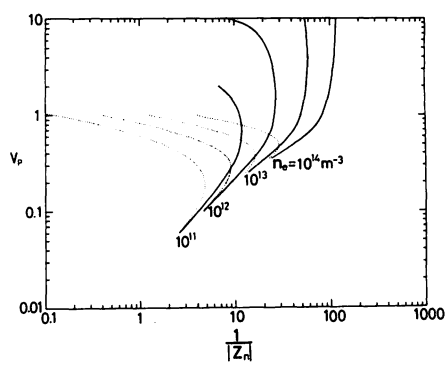


Fig. 25 Admittance values of sheath resonance and antiresonance

decreases gradually. When the sheath thickness is small, the electron density in the sheath is very near that in the ambient plasma, and as the sheath thickness increases, the admittance characteristic curve shifts to the lower frequency. But when the probe potential reaches to some value, the capacitance component of the sheath impedance increases due to the decrease of the electron content in the sheath, and again the resonant frequency increases.

Figure 25 shows the normalized admittance values of the minimum and the maximum which coincide with the resonant and antiresonant frequencies in Fig. 24. The main feature of the antiresonant frequency characteristic is that there exists a maximum at some probe potential. On the other hand, it is clear that the change of the resonant frequency characteristic is rather gradual.

b) Admittance variation by the electron temperature

Figure 26 shows the three cases of T_e = 0.1, 0.2 and 0.5 eV. As the electron temperature increases, the sheath thickness becomes larger and the resonant and antiresonant frequencies increase.

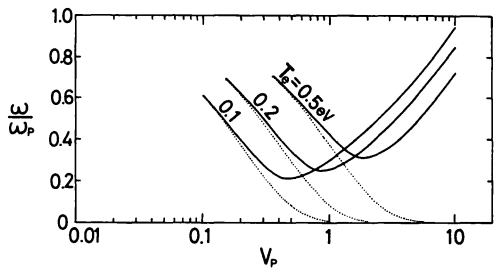


Fig. 26 Sheath resonant and antiresonant frequency variation by the electron temperature

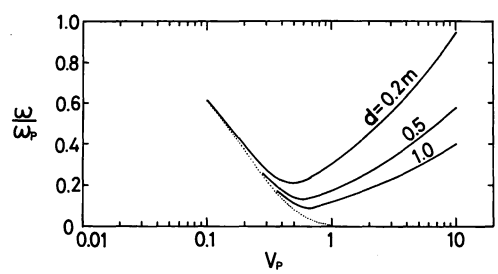


Fig. 27 Sheath resonant and antiresonant frequency variation by the probe distance

c) Admittance variation by the probe impedance

Figure 27 shows the three cases of d = 0.2, 0.5 and 1.0 m. The first antiresonant frequency does not depend on the probe distance, that is, only due to the sheath region. As the probe distance increases, the inductive component of the plasma region increases, thus the resonant frequency decreases.

d) The case when the magnetic field exists

When the magnetic field is weak, the ion Lamor radius is rather large, so it is assumed that the sheath thickness is not altered by the magnetic field. And also the same potential profile and the electron density distribution in the sheath are assumed as in the case without the magnetic field.

Permitivity K_O in this case is given by,

$$K_O = 1 - \frac{\omega_p^2(\omega - j\nu)}{\omega\{(\omega - j\nu)^2 - \omega_c^2\}} \quad , \qquad \cdots\cdots\cdots\cdots\cdots\cdots\cdots\cdots\cdots\cdots (63)$$

where ω_c is the electron cyclotron angular frequency.

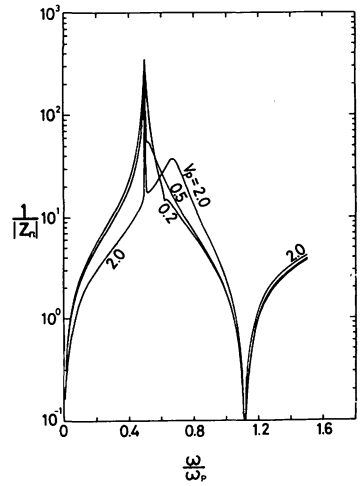


Fig. 28 Admittance characteristic curves when the magnetic field exists

Figure 28 shows the admittance characteristic when the magnetic field exists and its direction is parallel to the planar electrode surface. Here it is assumed that $\omega_c/\omega_p = 0.5$. It is clear that the admittance at the cyclotron frequency shows maximum value. In the case of $V_p = 0.2$ V, the characteristic curve is similar to the case of a plasma without the magnetic field except the region of about 0.62 ω/ω_p. As the probe potential increases, the sheath thickness increases, thus the sheath resonant frequency approaches to the cyclotron frequency. Furthermore as the probe potential increases, the maximum and minimum values increase with the probe potential. Figure 29 shows the value of the frequency at the minimum and maximum against the probe potential for the three cases of $\omega_c/\omega_p = 0.2, 0.5$ and 1.0.

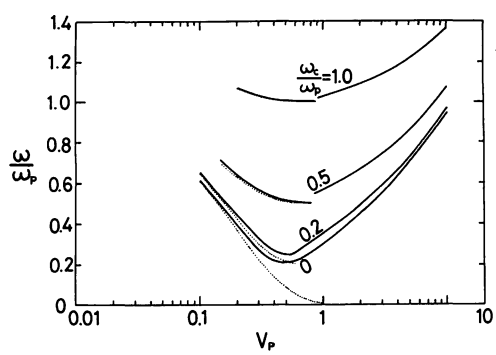


Fig. 29 Sheath resonant and antiresonant frequency variation by the magnetic field

(2) Spherical probe

The impedance between the two spheres as shown in Fig. 30 will be considered. It is assumed that the probe radius is r_p, the sheath radius is r_s and the center distance is d. The same assumption for the potential profile in the sheath is made as that of the planar probe. Thus the potential and the electron density n_{er} at a distance r from the center of the probe, are expressed as follows,

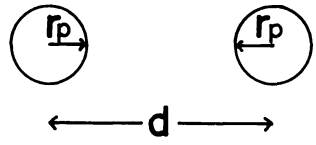


Fig. 30 Spherical probe configuration

$$V(r) = -V_p(r_s - r)^2/(r_s - r_p)^2, \quad \cdots\cdots (64)$$

$$n_{er} = n_e \exp\{-eV(r)/(kT_e)\}, \quad \cdots\cdots (65)$$

where V_p is the probe potential.

From the analogy of the planar probe, the spherical sheath impedance is,

$$Z_s = \frac{1}{4\pi j\omega\epsilon_0} \int_{r_p}^{r_s} \frac{dr}{r^2 \{1 - \dfrac{n_{er}e^2}{m\epsilon_0(\omega^2 - j\omega\nu)}\}}, \quad \cdots\cdots (66)$$

The plasma impedance between two spheres is,

$$Z_p = (2\pi j\omega\epsilon_0 r_s K_0 \sum_{N=1}^{\infty} Q_N)^{-1}, \quad \cdots\cdots (67)$$

where

$$Q_1 = 1 + M,$$

$$Q_2 = M^2/(1 - M^2),$$

when $N = 3$,

$$Q_N = (1/MQ_{N-1} - 1/Q_{N-2})^{-1},$$

$$M = r_s/d.$$

By using the normalizing factor $4\pi\omega_p\epsilon_0$, the normalizing impedance is expressed as,

$$Z_n = 4\pi\omega_p\epsilon_0(2Z_s + Z_p). \quad \cdots\cdots (68)$$

Figure 31 shows the normalized admittance against the normalized frequency ω/ω_p in the cases of $n_e = 10^{12}$ m^{-3}, $T_e = 0.1$ eV, $\nu_e/\omega_p = 0.01$, $r_p = 0.01$ m, $d = 0.2$ m and $V_p = 0.03$, 0.1, 0.5 and 2.0 V. The admittance characteristic features are similar to that of the planar probe. Figure 32 shows the relations between the resonant frequency and the

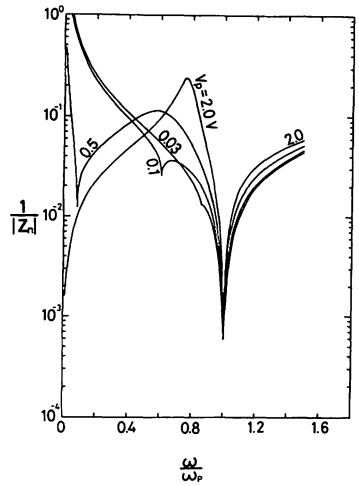


Fig. 31 Admittance characteristic curves

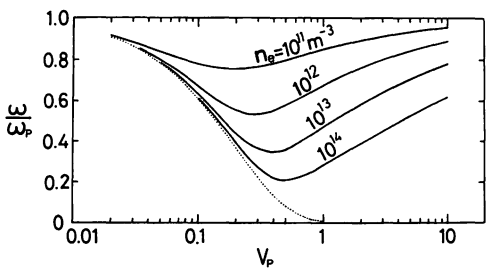


Fig. 32 Sheath resonant and antiresonant frequency variation by the electron density

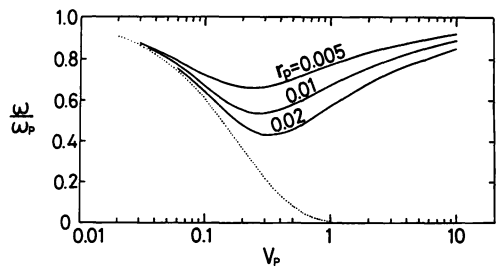


Fig. 33 Sheath resonant and antiresonant frequency variation by the probe radius

probe potential for the four cases of n_e = 10^{11}, 10^{12}, 10^{13} and 10^{14} m^{-3}. The dotted line indicates the antiresonance and the solid lines indicate the sheath resonance.

Figure 33 shows the relations between the probe radius and the resonant frequency for the three cases of r_p = 0.005, 0.01 and 0.02 m. As the probe radius increases, the sheath resonant frequency decreases.

2.4.4 Summary

The sheath-plasma impedance/admittance of the planar and spherical geometries are calculated by assuming the parabolic electron density distribution in the sheath. Here the conclusions are arranged in the followings.

(1) The assumption of the discontinuous electron density distribution in the sheath is not suitable, the continuous sheath model must be considered.

(2) The sheath-plasma impedance changes very widely by the probe potential in the

frequency range lower than the plasma frequency or upper hybrid frequency when the magnetic field exists.
(3) There exists an antiresonance in the frequency range lower than the sheath resonance at lower probe potential but the antiresonance disappears at higher probe potential.
(4) The values of the admittance at the sheath resonance and the antiresonance have maxima at some probe potential.
(5) As the electron density decreases, the frequency of the sheath resonance shifts to the lower part.
(6) As the electron temperature increases, the frequencies of the sheath resonance and the antiresonance shift to the higher part.
(7) As the probe distance increases, the frequency of the sheath resonance shifts to the lower part.
(8) When the magnetic field exists, there is always maximum value in the admittance characteristic at the cyclotron frequency, and there appears a sheath resonance between the cyclotron frequency and the upper hybrid frequency.
(9) There is no essential difference in the impedance profiles of the planar and spherical geometries.

2.5 Two-Wire Radio Frequency Probe

2.5.1 Introduction

The transmission line, so called the lecher lines are used in all modern high-frequency applications. A transmission line may be made up of parallel plates, of coaxial conductors, or in general of any two conductors separated by a dielectric material. The transmission line shows the various impedance properties according to the frequency range, the input impedance of the lecher wire shows inductance or capacitance according to the length of the line. In the case that the lecher lines are located in a plasma, the input impedance of the lecher lines shows distinguishable change from non-dispersive media according to the frequency. And there are various modes of the plasma waves, that is, electromagnetic wave and electrostatic wave in a plasma, especially when the magnetic field exists. According to the mode of the wave, characteristic of the lecher lines shows the remarkable change with frequency.

When an electrode is inserted in a plasma, the ion sheath exists around the boundary of a plasma. Therefore the sheath must be considered in discussing the above problems. Especially it becomes an important problems in the frequency range lower than the plasma frequency. Two parallel cylindrical probes which are similar to the lecher lines are treated by Crawford and Harp (1965), Messiaen and Vandenplas (1966), Wait (1966, 1967) and others. Numerical studies on electrical properties of the lecher lines in a magnetoplasma are very useful in a theoretical consideration. Here the method of the equivalent dielectric constant is used in order to treat this problem.

2.5.2 Impedance between Two Wires

At first, a structure of the ion sheath around wire is considered in the following. As the ion sheath profile, the ion sheath without the magnetic field was analyzed by Langmuir and Blodgett (1923, 1924). When the magnetic field exists, the ion sheath is treated by Spiwak and Reichrudel (1938), Brilloin (1941), Dote and Amemiya (1964, 1967) and others, and

their treatment is developed from the theory of Langmuir and Blodgett. But in the case of ion sheath, when the magnetic field is weak, the Larmor radius is larger than Debye length, in this case the sheath thickness is scarcely altered by the magnetic field. Here it is assumed that the magnetic field is weak and the ion sheath thickness is not altered by the existence of the magnetic field. So the sheath model by the Langmuir-Mott-Smith theory is used. The potential $V(r)$ at the point r in the sheath region is expressed by:

$$\left\{\frac{V(r)}{V_p}\right\}^{3/2} = \frac{r\beta^2(r_s/r)}{r_p\beta^2(r_s/r_p)}, \quad \cdots\cdots (69)$$

where V_p is the probe potential, r_p is the probe radius, β is the function of r_s/r in cylindrical sheath, r_s is the sheath radius. And the electron density $n(r)$ in the sheath region is expressed by Boltzmann's law.

$$n(r) = n_e \exp\left[-eV(r)/kT_e\right], \quad \cdots\cdots (70)$$

where e is the electron charge, T_e is the electron temperature and k is the Bolzmann constant.

The sheath impedance per unit length is

$$Z_s = \frac{1}{2\pi j\omega\epsilon_0}\int_{r_p}^{r_s}\frac{dr}{r\epsilon(r)}, \quad \cdots\cdots (71)$$

where $\epsilon(r)$ is the equivalent specific dielectric constant at distance r from the center in the sheath. j is the imajinary unit, ϵ_0 is the dielectric constant in free space.

Thus, the impedance between the two parallel wires with sheath per unit length is expressed as follows:

$$Z_p = \frac{1}{\pi j\omega\epsilon_0\epsilon}\ln\frac{d+\sqrt{d^2-4r_s^2}}{2r_s} + \frac{1}{\pi j\omega\epsilon_0}\int_{r_p}^{r_s}\frac{dr}{r\epsilon(r)}, \quad \cdots\cdots (72)$$

where d is the center distance of the two wires and ϵ is the equivalent specific dielectric constant in a plasma. The first term shows plasma impedance and the second term shows twice of the sheath impedance value.

Next, from the theory of the transmission line the impedance is expressed as:

$$Z = Z_W \coth \gamma l, \quad \cdots\cdots (73)$$

where Z_W is the characteristic impedance, γ is the phase constant. It is assumed that the lines do not contain the loss component, that is, lossless, and the skin effect is neglected, the line includes only the distributed inductance component per unit length,

$$\frac{j\omega}{4\pi}\left(4\mu_0 \ln\frac{d}{r_p} + \mu\right), \quad \cdots\cdots (74)$$

where μ_0 is the permitivity in free space, μ is that of the wires, but in this case, for example, Cu metal $\mu \simeq \mu_0$ except the feromagnetic media.

Thus,

$$Z_w^2 = \frac{1}{(\pi\epsilon_0 c)^2}\left(\ln\frac{d}{r_p}+\frac{1}{4}\right)\left\{\frac{1}{\epsilon}\ln\frac{d+\sqrt{d^2-4r_s^2}}{2r_s}+\int_{r_p}^{r_s}\frac{dr}{r\epsilon(r)}\right\}, \quad \cdots\cdots\cdots\cdots \quad (75)$$

$$\gamma^2 = -\frac{\left(\frac{\omega}{c}\right)^2\left(\ln\frac{d}{r_p}+\frac{1}{4}\right)}{\frac{1}{\epsilon}\ln\frac{d+\sqrt{d^2-4r_s^2}}{2r_s}+\int_{r_p}^{r_s}\frac{dr}{r\epsilon(r)}} \quad \cdots\cdots\cdots\cdots\cdots\cdots\cdots\cdots \quad (76)$$

Next the equivalent specific dielectric constant of a plasma will be considered. We will treat the plane wave for the brevity. Although there exist many kinds of waves in a plasma, there are mainly two kinds of wave mode, electromagnetic wave and electrostatic wave. The ion motion is neglected and we will assume the static positive charge.

(1) Electromagnetic wave

At first the electromagnetic wave will be considered. Anisortropic dielectric tensor of a magnetoplasma is treated by cold plasma approximation (for example, Stix, 1966). For the cartesian coordinates (x, y, z) with B_0 along the z axis, the dielectric tensor is given explicitly:

$$\boldsymbol{K} = \epsilon_0\begin{bmatrix} S & jD & 0 \\ -jD & S & 0 \\ 0 & 0 & 0 \end{bmatrix}, \quad \cdots\cdots\cdots\cdots\cdots\cdots\cdots\cdots\cdots\cdots\cdots\cdots \quad (77)$$

where

$$S = 1-\frac{\omega-j\nu_e}{\omega}\cdot\frac{\omega_p^2}{(\omega-j\nu_e)^2-\omega_c^2},$$

$$D = \frac{\omega_e}{\omega}\cdot\frac{\omega_p^2}{(\omega-j\nu_e)-\omega_c^2},$$

$$P = 1+\frac{\omega_p^2}{j\omega}\cdot\frac{1}{j\omega+\nu_e},$$

$$\omega_p^2 = \frac{n_e e^2}{m\epsilon_0} \quad \text{(Electron plasma angular frequency)},$$

$$\omega_c = \frac{eB_0}{m} \quad \text{(Electron cyclotron angular frequency)},$$

ν is the collision frequency. MKS rationalized units are used here. The refractive index n of the plane wave is expressed as follows when the wave propagates with the direction angle θ between B_0 axis and the wave propagated direction:

$$n^2 = \frac{(S+D)(S-D)\sin^2\theta+PS(1+\cos^2\theta)\pm[(S+D)(S-D)-PS]^2\sin^4\theta+4P^2D^2\cos^2\theta}{2(S\sin^2\theta+P\cos^2\theta)} \quad \cdots \quad (78)$$

On the one hand, there is a relation among the equivalent dielectric constant ϵ, permiability μ, and the refractive index n (Stratton, 1941),

$$n^2 = \frac{\epsilon\mu}{\epsilon_0\mu_0} . \quad \cdots\cdots (79)$$

When the medium is non-magnetic for a plasma, $\mu \simeq \mu_0$. Thus the refractive index is simply expressed as follows:

$$n^2 = \sqrt{\epsilon/\epsilon_0} . \quad \cdots\cdots (80)$$

Here we will describe the next two cases.

a) Propagation perpendicular to $\bar{B}_O$ ($\bar{k} \perp \bar{B}_O$)
For the propagation in the direction $\theta = \pi/2$,
i) Ordinary mode

$$\epsilon = \epsilon_0(1 - \omega_p^2/\omega^2). \quad \cdots\cdots (81)$$

ii) Extraordinary mode

$$\epsilon = \epsilon_0 \frac{(\omega^2+\omega\omega_c-\omega_p^2)(\omega^2-\omega\omega_c-\omega_p^2)}{\omega^2(\omega^2-\omega_c^2-\omega_p^2)} . \quad \cdots\cdots (82)$$

b) Propagation parallel to $\bar{B}_O$ ($\bar{k} // \bar{B}_O$)
i) Left-hand-polarized mode

$$\epsilon = \epsilon_0 \left(1 - \frac{\omega_p^2}{\omega^2+\omega\omega_c}\right) . \quad \cdots\cdots (83)$$

ii) Right-hand-polarized mode

$$\epsilon = \epsilon_0 \left(1 - \frac{\omega_p^2}{\omega^2-\omega\omega_c}\right) . \quad \cdots\cdots (84)$$

(2) Electrostatic wave
In a hot plasma, there also exist the electrostatic waves in addition to the electromagnetic wave. The equivalent dielectric constant is obtained from the wave equation under the quasi-static approximation.
a) $\bar{k} // \bar{B}_0$, parallel case (Longitudinal electrostatic wave)

$$\epsilon = \epsilon_0 \left[1 + \frac{\omega_p^2 m}{k^2 kT_e} \{1 - 2\alpha S(\alpha)\}\right] , \quad \cdots\cdots (85)$$

where

$$\alpha = \frac{\omega}{k\sqrt{\frac{2kT_e}{m}}} , \quad S(\alpha) = \exp(-\alpha^2) \int_0^\alpha \exp(t^2)dt.$$

In the Eq. (85) the term ω_{pi}/ω^2 (ω_{pi}; ion plasma frequency) concerning the ions is neglected, and $S(\alpha)$ is the complex error function.

This longitudinal electrostatic wave exists in the case without the magnetic field.

b) $\bar{k} \perp \bar{B}_O$, perpendicular case (Electrostatic cyclotron wave)

$$\epsilon = \epsilon_0 \left[1 + \frac{2\omega_p^2}{\lambda \omega_c^2} \sum_{N=1}^{\infty} \exp(-\lambda) I_N(\lambda) \frac{N^2}{N^2 - (\frac{\omega}{\omega_c})^2} \right], \quad \cdots\cdots\cdots\cdots\cdots\cdots \quad (86)$$

where $I_N(\lambda)$ is modified Bessel function of N-th order,

$$\lambda = \frac{k^2 k T_e}{\omega_c^2 m},$$

and k is the wave number.

2.5.3 Numerical Examples

The parameters are assumed in the following,
Electron density $n_e = 10^{12}$ m^{-3}.
Electron temperature $T_e = 0.1$ eV,
Radius of the wire $r_p = 0.001$ m,
Length of the wire $l = 10$ m,
Separation distance $d = 0.1$ m,
Collision frequency $\nu = 0$,
Electron cyclotron angular frequency $\omega_c = 0.3\omega_p$.

(1) Electromagnetic wave

a) Ordinary mode case with and without the sheath ($k \perp B_0$)

Figure 34 shows the input impedance profile against the normalized angular frequency

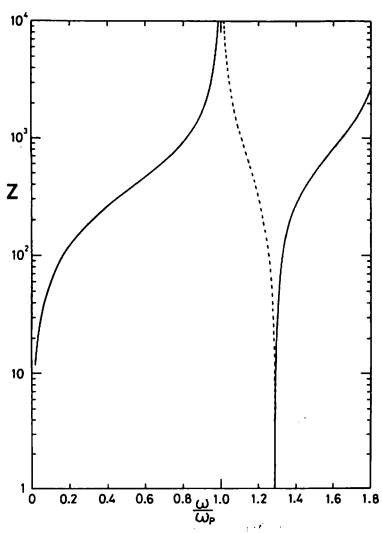


Fig. 34 Input impedance profile (Ordinary mode, without sheath). The solid and dashed lines show inductive and capacitive respectively)

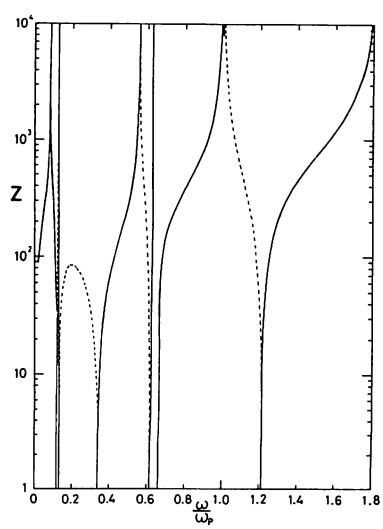


Fig. 35 Input impedance profile (Ordinary mode, with sheath)

ω/ω_p in the case of the ordinary mode without sheath. The solid and dotted lines in Fig. 34 indicate inductive and capacitive components respectively. The minimum at $\omega/\omega_p \simeq 1.289$ is due to the lecher wire characteristic. The frequency at the minimum shifts to the higher frequency when the length of lecher wire becomes short. Figure 35 shows the input impedance profile in the case when the sheath exists around the wires. Here, we will assume DC potential of the wires is 0.5 V, then, the sheath thickness r_s is 9.82389 r_p. The minimum at $\omega/\omega_p \simeq 1.211$ is also due to the lecher wire characteristic similar to the case as shown in Fig. 34. The minimum at $\omega/\omega_p \simeq 0.660$ coincides with so-called sheath resonance and there are infinitly many resonances in the frequency range between about 0.635 and 0.660. These resonances and the resonances below $\omega/\omega_p \simeq 0.635$ are due to the lecher wire characteristic.

b) Extraordinary mode case ($k \perp B_0$)

Figure 36 shows the input impedance profile in the case of extraordinary mode when there is no sheath region around wires. The maxima at $\omega/\omega_p \simeq 0.861$ and 1.161, and the minimum at $\omega/\omega_p \simeq 1.044$ are the singular point of ϵ expressed in Eq. (82). There are infinitely many maxima and minima in the frequency range between about 1.027 and 1.044. All these resonances are due to the lecher wire characteristic.

c) Left-hand-polarized mode ($k // B_0$)

Figure 37 shows the input impedance profile in the case of left-hand-polarized mode when there is no sheath region around the wires. The maximum at $\omega/\omega_p \simeq 0.861$ is the singular point of ϵ of Eq. (83) and the minimum at $\omega/\omega_p \simeq 1.209$ is due to the lecher wire characteristic.

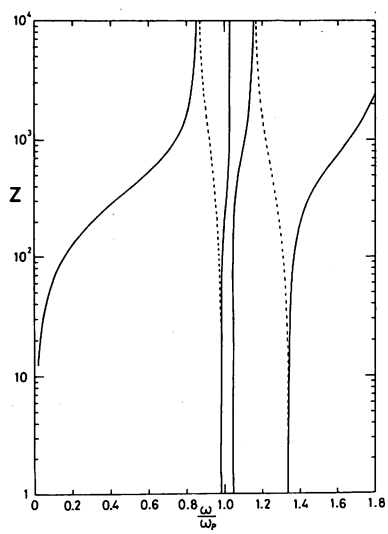


Fig. 36 Input impedance profile (Extraordinary mode, without sheath)

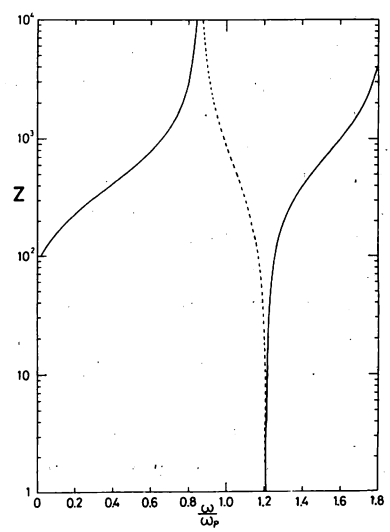


Fig. 37 Input impedance profile (Left-hand-polarized mode, without sheath)

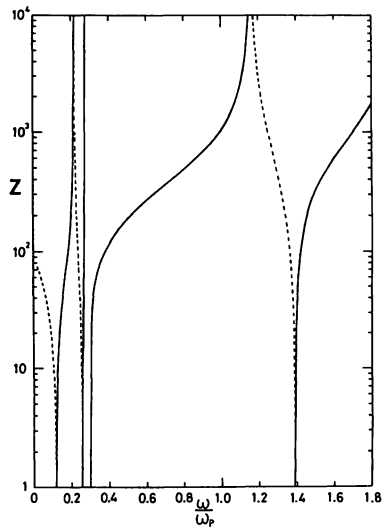


Fig. 38 Input impedance profile (Right-hand-polarized mode, without sheath)

d) Right-hand-polarized mode ($k // B_0$)

Figure 38 shows the input impedance profile in the case of right-hand-polarized mode when there is no sheath region around wires. The minimum at $\omega/\omega_p = 0.3$ and the maximum at $\omega/\omega_p \simeq 1.1612$ are the singular point of ϵ of Eq. (84). Other maxima and minima including those between about 0.256 and 0.3 are due to the lecher wire characteristic.

(2) Electrostatic mode

a) Longitudinal electrostatic mode ($k // B_0$)

Here we assume the electrostatic wave length λ is $2d$ for the brevity, and also assume that the wavelength does not change in the sheath region and the plasma region. Figure 39 shows the input impedance profile in the case of longitudinal electrostatic mode when the sheath does not exist around the wires. The infinities at $\omega/\omega_p \simeq 0.097$ and 1.008 correspond to the slow and fast electron accoustic mode respectively (Stix, 1962). The minimum at $\omega/\omega_p \simeq 1.239$ is due to the lecher wire characteristic. Figure 40 shows the input impedance profile in the case that there exists sheath around wires. The profiles are very complicated. The minimum at $\omega/\omega_p \simeq 0.672$ corresponds to the sheath resonance. There are infinitely many maxima and minima in the frequency range between about 0.657 and 0.672.

b) Electrostatic cyclotron mode ($k \perp B_0$)

We also assume that the wavelength is $2d$. Figure 41 shows the input impedance profile in the case of electrostatic cyclotron mode. There does not exist sheath around the wires. There appear maxima or minima at $\omega/\omega_p = 0.3$ and its integer times, and also appears the infinity at $\omega/\omega_p \simeq 1.055$ which is the upper hybrid frequency. Furthermore the infinities and minimum below $\omega/\omega_p = 0.3$ and the minimum at $\omega/\omega_p \simeq 1.315$ are due to the lecher wire characteristic. There are infinitely many maxima and minima in the frequency range

between about 0.278 and 0.3. Figure 42 shows the input impedance profile when there exists sheath around the wires. The impedance profile shows the very complicated characteristics and there are a great many maxima and minima in all frequency range.

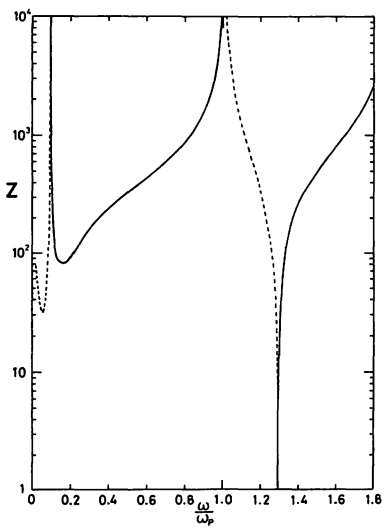


Fig. 39 Input impedance profile (Longitudinal electrostatic mode, without sheath)

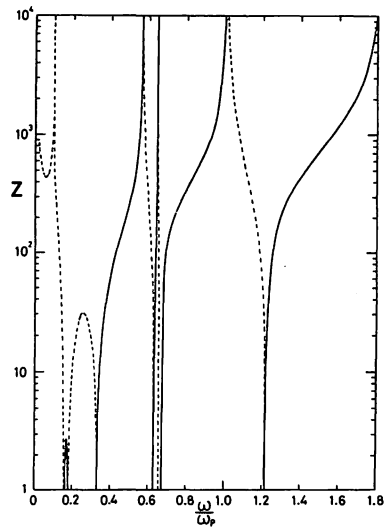


Fig. 40 Input impedance profile (Longitudinal electrostatic mode, with sheath)

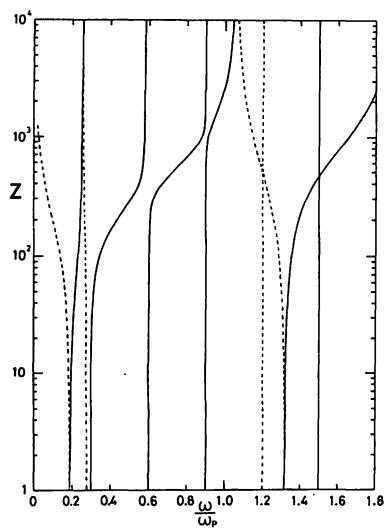


Fig. 41 Input impedance profile (Electrostatic cyclotron mode, without sheath)

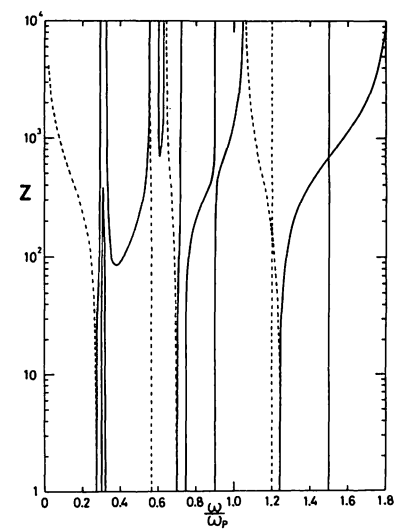


Fig. 42 Input impedance profile (Electrostatic cyclotron mode, with sheath)

2.5.4 Summary

As described in the introduction, Lecher wire in general, the parallel cylindrical lines are symmetrical shape, the electrical impedance property is derived more regorously than the asymmetrical system. Especially when the sheath exists around the electrode, impedance or admittance characteristic of the radio frequency probe greatly depends on the shape of the sheath. Therefore the two parallel wire probes are the best configuration in the other probe systems. Concerning with electrostatic mode, cyclotron harmonics are detected in the space chamber experiment (Mori *et al.*, 1973) and the rocket-borne radio frequency probe experiment (Ejiri, 1973). And by considering the ions in the dispersion formula, the electrical properties of the lower hybrid frequency, ion acoustic wave, the magnetosonic containing Alfven wave are able to be discussed. Furthermore when the magnetic field exists, about the electrostatic cyclotron wave, Landau damping and the magnetic field angle dependency can be investigated by the experiment by using the grided parallel wire probes. In practice, there exist not only single mode of the wave but also many modes of the waves simultaneously and various wavelength can be exist. Therefore the practical input impedance profile becomes more complex, but the above described characteristics are very useful to consider the characteristic of the Lecher wire.

2.6 Special Features of the Space Vehicle Use of Probes in the Ionospheric Plasma

There are two important facets of the spacecraft situation which normally control the experimental approach. Firstly, space plasma (ionosphere and magnetosphere) to be measured has the very complicated properties comparing with laboratory plasma. That is, at the lower part, the ionosphere is the partial ionized plasma, thus the collision process is important and there are many species of neutral particles and ions. The space plasma is low density and distributed wide range of temperature. In the case of electron, the altitude of 80 km is the transition region above which the electron collision frequency is less than the electron cyclotron frequency. In the case of ion, transition altitude is about 120 km. Accordingly the earth's upper atmosphere above about 200 km is considered to be plasma state. Although the neutral particle density is larger than the plasma density below about 10^4 km, the plasma density is lower than the neutral particle density above 10^4 km and fully ionized plasma consisting of protons and electrons. The interaction between the earth's magnetic field and plasma acts a very important role on the phenomena occurred in that region.

In planning probe instrumentation for a spacecraft, the parameters of Larmor radius and mean free path provide a guide to the probe geometry and mode of operation. There appears space charge layer called ion sheath around the electrode which is inserted in a plasma. The sheath thickness is of the order of the Debye length. Therefore the probe dimension has a close correlation with the Debye length. A further important problem arises in the D region of the ionosphere because the mean free path is comparable to or shorter than both the Debye length and the vehicle size. To date no fully adequate theory of probe action on supersonic spacecraft in this region has been published and the alternative empirical or semi-empirical approach has also been little studied. In measuring the quantities relating to the magnetic field the Larmor radius is important to decide the dimension of the probing electrode.

The second important fact of the spacecraft measurement is that the spacecraft is

almost always supersonic and often hypersonic with respect to the ions. In analysing data in the measurement, the method of the analysis is changed by the free molecular flow or continuous flow or transition flow (Hoult, 1964, 1965; Hoult and Kuo, 1966; Sonin, 1967).

Ram effect and wake effect become very important problem in connection with supersonic motion of the spacecraft. Furthermore, photoelectric effect on the surface of the electrode is also very important problem. And the potential alternation by the precipitation of the charged particle gives the severe effect to the measurement. In the measurement by the space vehicle, as the probe system is floating condition in a plasma, the problem of the return current is important, therefore the surface area and the status of the space vehicle are important as well as that of electrode system. And the hysteresis effect (Oyama, 1975) is very complicated problem. In the case of electron measurement, the earth's magnetic field gives the effect on current-voltage characteristic even in the electrostatic probe method (Ichimiya *et al.*, 1965). Lastly the data processing system and the telemetry system are also important problems.

Chapter III Ionospheric Studies by Sounding Rockets

3.1 Rocket Observations at Akita Rocket Range

3.1.1 Introduction

The first rocket range in Japan was constructed at Michikawa, Akita Prefecture, facing the Japan Sea. The position of the rocket range is 39°34′12″N, 140°03′35″E (geographic coordinates) and 29.3°N, 205.3°E (geomagnetic coordinates). In 1960, the test flight of rocket K-8-1 was carried out successfully, thus the rocket Kappa-8 became available for a sounding rocket. By this time, the fundamentals of rocket observation of ion density were investigated and design and construction of an ion detector were studied. Ten ionospheric sounding rockets were fired at Akita rocket range. Table 2 shows the general specifications of the ionospheric sounding rockets; name of rocket, firing date and time, peak altitudes, number of probes and measuring items. Only Langmuir probe was mounted on the first three rockets K-8-2, -3 and -4. The ion densities in the ionosphere in the daytime and nighttime were measured. The first ionospheric sounding rocket K-8-2 was fired in July, 1960. But the observation failed because that the nose-cone of the rocket did not open and the probe was not exposed in the ionosphere. K-8-3 and -4 were fired to observe the ion density in the ionosphere in September, 1960, and both succeeded in the measurement of positive ion density. In the next three rockets K-8-5, -6 and -7, the electron density, electron temperature and ion density in the E region and the lower part of the F region of the ionosphere were measured by means of both the resonance and Langmuir probes. The instruments for K-8-8 had a total of five probes. By observing the ion density in the daytime and the nighttime with both a meshed and a solid spherical probes, we can determine the quantity of photoelectron emission, the coefficient of transparency of the meshed probe, and the formulae for calculation of the orbital motion region, the one collision region and the many-collision region.

Table 2 Ionospheric sounding rockets at Akita rocket range

Rocket	Date	Time (135°EMT)	Peak alt. (km)	No. of probes	Measuring items
K-8-2	July 17, 1960	13^h11^m	182	1	N_i
K-8-3	Sept. 22, 1960	15 32	187	1	N_i
K-8-4	Sept. 26, 1960	20 25	183	1	N_i
K-8-5	Mar. 27, 1961	13 08	172	3	N_i, N_e, T_e
K-8-6	Apr. 18, 1961	21 27	144	3	N_i, N_e, T_e
K-8-7	July 21, 1961	11 42	159	3	N_i, N_e, T_e
K-8-8	Oct. 24, 1961	12 59	198	5	N_i, N_e, T_e

3.1.2 Instrument

(1) K-8-2, -3 and -4

Only a Langmuir probe was mounted on these rockets. A meshed spherical probe was used in the daytime observation. In the nighttime observation, however, an ordinary solid spherical probe was used because there was no solar radiation at night. The measurement of ion density was made by applying variable voltage to a probe and measuring the probe current.

(2) K-8-5, -6 and -7

Three probes were mounted on these rockets; a resonance probe, an ion current probe and an electron Langmuir probe to measure electron and ion density and electron temperature. The function of each probe is as follows:

a) Resonance probe

A resonance probe is one kind of radio frequency probe (Takayama *et al.*, 1960; Miyazaki *et al.*, 1960; Hirao and Miyazaki, 1963b). If radio frequency voltage is applied to a probe inserted in a plasma, superimposed on DC voltage, the DC current through the probe is considerably different from the case where only DC voltage is applied. When the radio frequency is fairly lower than the plasma frequency, the electron temperature of a plasma is determined by that difference in DC current. Also, the above described difference of DC current becomes a maximum when the frequency of applied radio frequency voltage corresponds to the frequency relating to the electron plasma frequency. It is, therefore, possible to determine the electron density from the resonant frequency. It is convenient to measure the electron temperature by applying a probe with two kinds of voltage. So we used two kinds of radio frequency voltage of 0.4 V and 0.8 V to apply the probe with in the cases of K-8-5 and -6. The DC voltage which appeared on the probe by the nonlinearity of a plasma is measured in order to calculate the electron temperature. We obtained the electron density and temperature from the radio frequency characteristics of a plasma. Radio sweep frequency voltages from DC to 7 MHz with the amplitudes of 0.5 V and 1.0 V were applied to the spherical probe 2 cm in diameter in the case of K-8-7. The sweeping period was about 0.5 sec.

b) Ion current probe

It was a meshed spherical probe 2 cm in diameter. Constant negative voltage of about

24 V was applied to the probe for continuous measurement of the ion density.

c) Electron Langmuir probe

It was a solid spherical probe of the same size as the other probes. Variable DC voltages from −2.63 V to +5.19 V were applied to the probe. The sweep time of the voltage was about 0.5 sec. After sweeping, −24 V was applied to the probe in a short time. Thus, we measured the ion density by the spherical probe. The method of analysis is the same as by a meshed ion probe. As for the two other parts, that is, the Langmuir probes with which the ion density, the electron density and the electron temperature are measured, the measuring circuit is essentially the same as K-8-3 and -4. And two probes are used for measuring the ion and the electron densities. As was previously described, the measuring circuit for the ion density is designed for making continuous measurement.

(3) K-8-8

We used five probes by adding two more probes to the previous three probes. One was to measure the electron temperature continuously; the other was a spherical probe for continuous measurement of the ion density.

3.1.3 Observational Results

(1) K-8-3

The ion current flowed almost just after the opening of the nose-cone at an altitude of about 60 km. The probe current increased as the rocket ascended, and attained to the maximum of about 2.5 μA at the top of trajectory, and then decreased with the descent of the rocket and became almost zero at an altitude of 60 km. But, when the rocket descended to

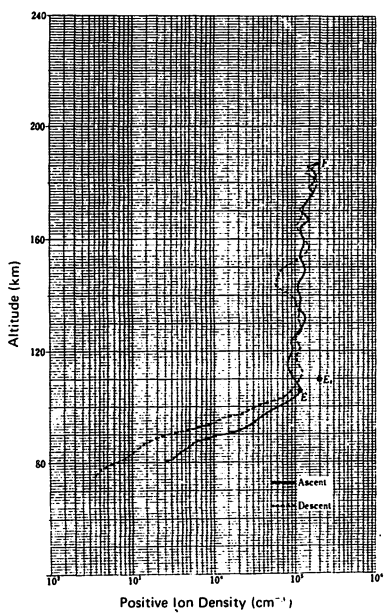


Fig. 43 Positive ion density profiles at Akita (K-8-3, Sept. 22, 1960; 15h32m 135°EMT)

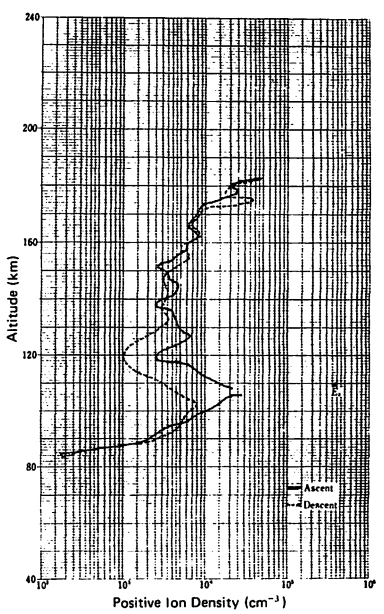


Fig. 44 Positive ion density profiles at Akita (K-8-4, Sept. 26, 1960; 20h25m 135°EMT)

an altitude of about 30–40 km, the probe current increased again. It is considered to have been caused by a thermal emission from the probe which became hot by friction between the surface of the probe and the surrounding air. The thermal emission became larger and larger and at last the current stopped to zero, then the probe was considered to be destroyed completely. Figure 43 shows the height distribution of the positive ion density from an altitude of 75 km to 186 km in the daytime ionosphere. In the figure, a black point E shows the real height of E layer observed by the vertical incidence sounding at the Akita Radio Wave Observatory, E_S shows that of the sporadic E layer, and the vertical short solid line named F shows that of $f_{min}F$. It shows that the E layer continues to the F layer gradually and a valley does not exist between these two layers.

(2) K-8-4

The probe current began to flow above 70 km and also increased with the height to the maximum of about 1 μA. During this flight the probe current showed an abrupt increase at an altitude of about 110 km in both ascending and descending modes. These increases correspond to the sporadic E layer as shown later on. In this flight also, the thermal emission current existed at the time of reentry into the atmosphere. Figure 44 shows the positive ion density profile in the altitude range from 85 km to 195 km in the nighttime ionosphere. In the figure, a black point E_S shows the real height of the sporadic E layer observed by the vertical incidence sounding. The rocket data of the height of the E_S layer agree well with the ionogram. The valley between the E and F layers at night is rather deeper than in the daytime.

(3) K-8-5

Figure 45 shows the positive ion density profile in the altitude range from 80 km to 170 km in the daytime ionosphere. Figure 46 shows the electron temperature profile in the daytime ionosphere.

(4) K-8-6

Figure 47 shows the positive ion density profile measured with the ion current probe. The solid line shows the curve in the ascending mode and the dotted line in the descending mode. From this figure it is evident that the E_S layer consists of three regions which are a few km thick. The probe current shows the zero for the most part of flight. So the ion densities in the most part of altitudes up to 144 km are presumed to be lower than 10^3 cm^{-3}. But, the ion current increased suddenly at an altitude of about 100 km. Those were coincident with the E_S layers.

(5) K-8-7

Figure 48 shows the ion density profile observed with the ion current probe. From the relation between the length of sheath radius around the probe and the mean free path of the ions, it can be seen that the region above 110 km is an orbital motion region where the mean free path of the ions is larger than the sheath radius. The region below 90 km is many collision region, and the median region is transitional region. Thus, taking consideration of the correction mentioned above, the final results were obtained.

(6) K-8-8

Figure 49 shows the positive ion density profile obtained by the meshed and solid spherical probes.

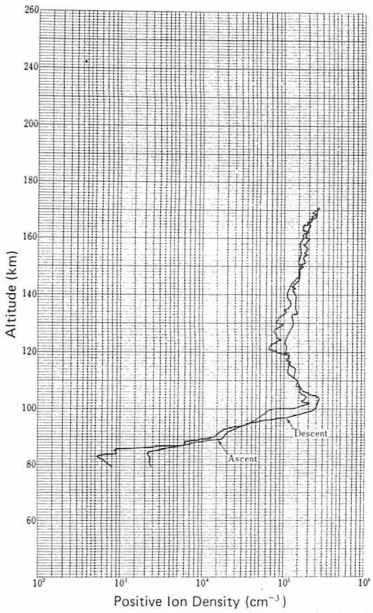


Fig. 45 Positive ion density profiles at Akita (K-8-5, Mar. 27, 1961; 13h08m 135°EMT)

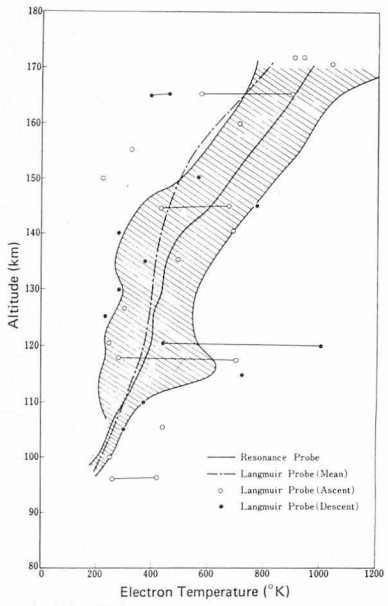


Fig. 46 Electron temperature profiles at Akita (K-8-5, Mar. 27, 1961; 13h08m 135°EMT)

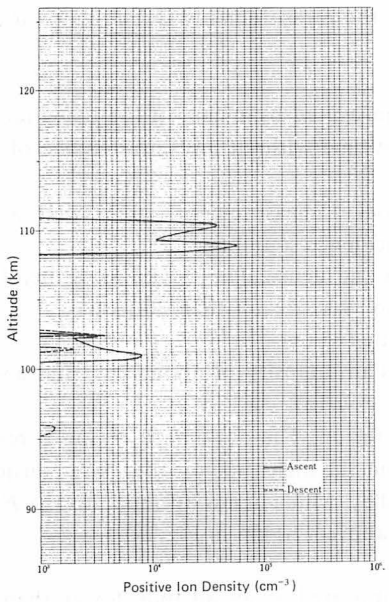


Fig. 47 Positive ion density profiles at Akita (K-8-6, Apr. 18, 1961; 21h27m 135°EMT)

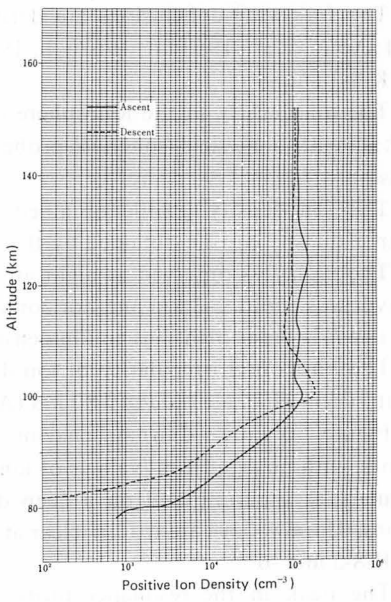


Fig. 48 Positive ion density profiles at Akita (K-8-7, July 21, 1961; 135°EMT)

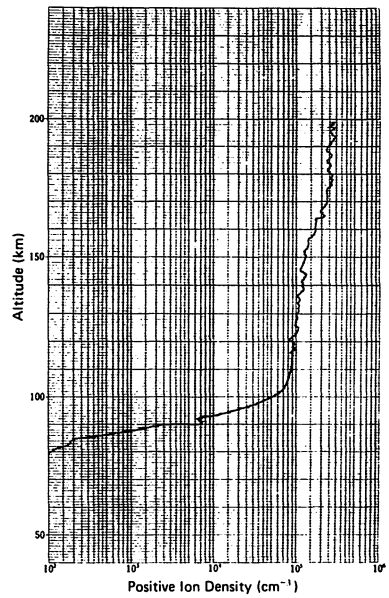


Fig. 49 Positive ion density profile at Akita (K-8-8, Oct. 24, 1961; 12h59m 135°EMT)

3.1.4 Summary and Discussions

The following conclusions are derived from the measurements (Ichimiya *et al.*, 1960, 1961; Aono *et. al.*, 1961a-d, 1962a, b, 1963).

(1) K-8-3 and -4

a) The ion density in the ionosphere could be measured by means of the Langmuir probe method with a meshed spherical probe in the daytime without any interference of photo-emission.

b) The ion density profile obtained by the rocket measurement agrees well with the electron density profile obtained by the vertical incidence sounding.

c) The E_S layers observed at night are very thin and dense. The thickness of the observed E_S layer was about 2–3 km and horizontal dimension was greater than 200 km.

d) The E layer at night has an ion density of about 10^4 cm^{-3}.

e) The horizontal irregularity of ion density has an intensity of about 20% and a scale of about 10 km at an altitude of 180 km (Aono *et al.*, 1961a).

f) Figure 50 shows diurnal behavior of the E region. The daytime E region is relatively smooth with no significant valleys of ionization, but the nighttime profiles have considerable irregularities superimposed on a deep density valley which tends to separate the E and F regions. These valleys are readily clear at altitudes above 120 km in Fig. 50.

(2) K-8-5 and -6

a) The peak in the resonance probe trace disappeared at an altitude lower than about 95 km due to the increase of collision frequency of electrons in the ionosphere in the case of K-8-5. Therefore, the measurement of electron density in lower region may well be made with the Langmuir probe.

b) Below the altitude of 140 km, the electron temperature distribution coincides with the neutral gas temperature of model atmosphere (Yonezawa, 1960). This shows that the ionosphere is a plasma in thermal state. But, above the altitude of 140 km, the electron temperature is higher than the neutral gas temperature. Figure 51 shows comparison of

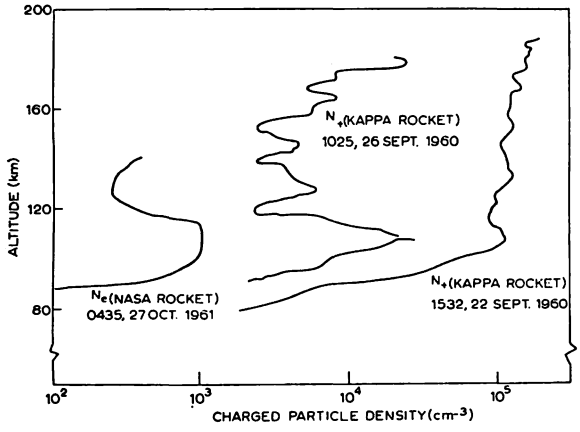


Fig. 50 Diurnal variation of the *E* region charged particle density (After Bourdeau *et al.*, 1965)

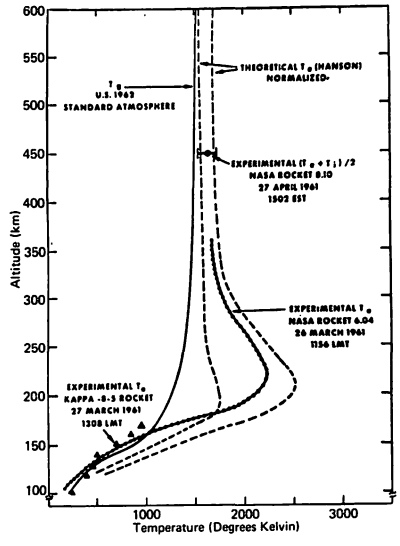


Fig. 51 Comparison of the altitude dependence of neutral gas and experimental and theoretical electron temperatures at mid-latitudes under quiet solar conditions (After Bourdeau, 1962)

neutral gas and experimental and theoretical electron temperatures profiles at mid-latitudes under quiet solar conditions. The electron temperature is much higher than the neutral gas temperature in the altitude range between about 150 km and 350 km. Temperature differences are due to photoionization of solar extreme ultraviolet radiation (Bourdeau, 1962).
c) At the time of 2130 hours, the plasma density is much smaller than 10^3 cm^{-3}. The E_S layer has multiple structures and the thickness of every layer is 2–3 km. The electron temperature is determined to be higher than 1000°K in the E_S layer.
(3) K-8-7 and -8
a) There was large difference in the results between the experiments of K-8-7 in June and K-8-8 in October. The plasma density above 100 km was indicated as being neary constant in the former experiment. In the latter experiment, the plasma density increases as the altitude increases. The electron temperature in the former case is generally higher than that in the latter case.
b) In the case of measurements of ion density by probes of the type used, we must consider many corrections to the results, for example, the photo-emission effect, the rate of transparency of the mesh and so on.
c) Number of electrons of photo-emission is 2.5×10^{11} sec^{-1} cm^{-2} by calculating for the photo-emission current of 0.04 μA/cm^2.

3.2 Rocket Observations during the IQSY at Kagoshima Space Center

3.2.1 Introduction

The place of rocket launching moved from Michikawa, Akita Prefecture to Uchinoura, Kagoshima Prefecture, the south of Kyushu Island in 1962 because that Akita rocket range and the Japan Sea, the dropping place of rockets, became narrower in area with the progress of sounding rockets. The new launching place faces the Pacific Ocean and its coordinates are 31°15′N and 131°04′45″E and the observing point of low geomagnetic latitude such as 19.8°N having special value in the field of geophysics. The geomagnetic longitude is 198.4°E.

The direct ionospheric observations were carried out at Kagoshima Space Center twenty-nine times in total till 1975; three times in 1962–63, twelve times during the IQSY and fourteen times in 1966–75. There were three-stage Lambda rocket of which peak altitude was more than 2000 km among them. The observing items are the positive ion density, the electron density, the electron temperature and so on. As other instruments in addition to the ionospheric measuring instrument are mounted on each rocket at the same time, synthetic observations of the upper atmosphere can be performed, especially observation by Lambda rocket has high values because a big payload of several kinds of instruments can be mounted on the rocket at the same time.

3.2.2 Instrument

A meshed spherical probe was used to measure the ion density in the daytime and a solid spherical probe was used in the nighttime till now. The purpose of using the meshed probe is to minimize the effect of photo-emission. Now, only in the case of limited capacity and weight for the payload or measurement of relative values of the ion density, the spherical type of the probe is used.

Since the IQSY, an ion trap was also used. The ion trap consists of two circular grids, G1 and G2, and a collector C, 8 cm in diameter each. DC sweep voltage is applied to the grid

G1, and by this potential are controlled the ions and electrons flowing into the ion trap. The voltage of −10 V is applied to the collector which collects only the ions passing through the grids. The voltage of about −40 V is applied to the second grid G2, and this grid prevents the photo-emission radiating from the collector. And the ion density is calculated from the ion current of the collector.

Three methods were used for measuring the electron density in the ionosphere. One is resonance probe method. One of two others is the Langmuir probe method by which the electron density is obtained from the current-voltage characteristic of the grid G1 in the ion trap. And the last one is to obtain the electron density from the electron current flowing to the probe to which the constant positive DC voltage is applied.

3.2.3 Observational Results

Table 3 shows the direct observations of the ionosphere by the sounding rockets during the IQSY. In the table are denoted name of rocket, firing date and time. In the following are described the results obtained by items of measurement.

Table 3 Ionospheric sounding rockets at Kagoshima Space Center during the IQSY

Rocket	Date	Time (135°EMT)	Peak altitude (km)
L-3-2	Jan. 31, 1965	14^h01^m	1040
K-9M-7	Feb. 6, 1965	14 01	(356)
L-3-3	Mar. 18, 1965	19 07	1100
K-9M-8	Mar. 25, 1965	20 21	324
K-9M-9	Mar. 27, 1965	14 01	335
K-8-12	July 16, 1965	19 50	160
K-9M-13	July 27, 1965	12 10	317
K-9M-14	Oct. 4, 1965	12 00	299

(1) Positive ion density

In the following, the solid lines named U and Y on the figures of the positive ion density profile show the results obtained by the vertical incidence soundings at Uchinoura and Yamagawa respectively.

a) L-3-3

The positive ion density profile in the altitude range from 171 km to 1099 km was measured with a planar ion trap. Figure 52 shows the ion density profile as well as the electron density. As the opening of the nose-cone was at an altitude of 161 km, the data could be obtained from an altitude of 171 km. The maximum positive ion density in the $F2$ region shows 2.8×10^5 cm^{-3} at an altitude of 249 km and almost coincides with the electron density obtained by vertical incidence sounding. Above an altitude of about 700 km, the density shows the constant value of about 2×10^4 cm^{-3}.

b) K-9M-8

The positive ion density profile in the altitude range from 71 km to 324 km was measured with a planar ion trap. The result is shown in Fig. 53. The maximum altitude

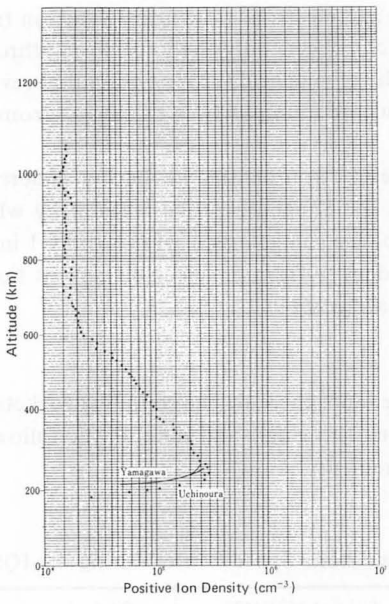


Fig. 52 Positive ion density profile at Kagoshima (L-3-3, Ascent, Mar. 18, 1965; 19h07m 135°EMT)

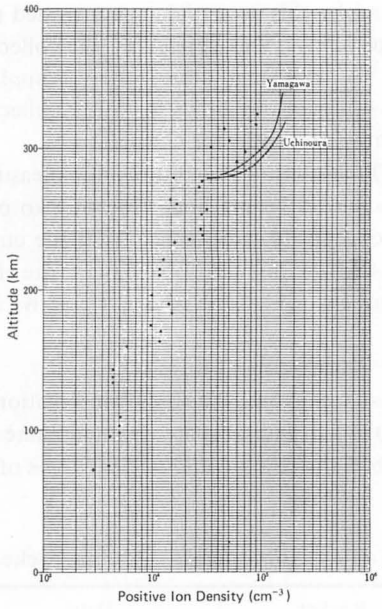


Fig. 53 Positive ion density profile at Kagoshima (K-9M-8, Ascent, Mar. 25, 1965: 20h21m 135°EMT)

analysed of 324 km was proved to be nearly equal to the maximum electron density in comparison with the result from the vertical incidence sounding.

c) K-8-12

The positive ion density profile in night E_S layer between 94.8 km and 96.4 km was measured with a disk probe to which the constant voltage was applied. The result is shown in Fig. 54. The maximum positive ion density appeared at an altitude of 95.5 km. According to observations at Yamagawa, the E layer showed the maximum electron density at 1953 hours, so the rocket measured about one minute and a half before the time, and the maximum stage of the E_S layer was expected to have larger density. Figure 54 shows that the positive ion density of the E_S layer was about 6.2 times that of quiet E region.

d) K-9M-13

The positive ion density profile in the altitude range from 75 km to 320 km was measured with a meshed spherical probe to which a constant negative voltage was applied. The result is shown in Fig. 55. In this figure, the dotted points are obtained from the calculation of the orbital-motion region in case of calculation of the positive ion density and the cross points in the many-collision region. The difference between these calculating methods is caused by the size of the ion sheath and the length of the mean free path of the ions (Dote *et al.*, 1962, 1963).

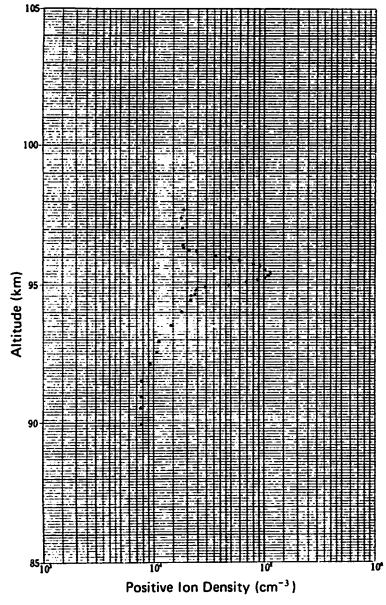


Fig. 54 Positive ion density profile at Kagoshima (K-8-12, Ascent, July 16, 1965; 19h50m 135°EMT)

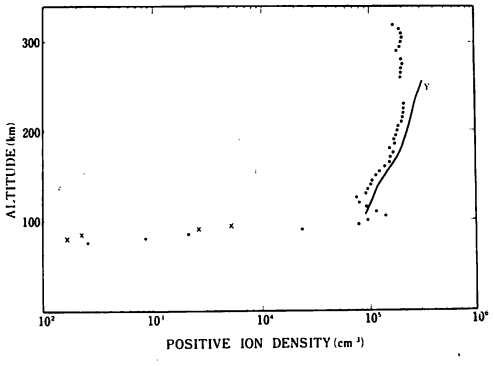


Fig. 55 Positive ion density profile at Kagoshima (K-9M-13, Ascent, July 27, 1965; 12h01m 135°EMT)

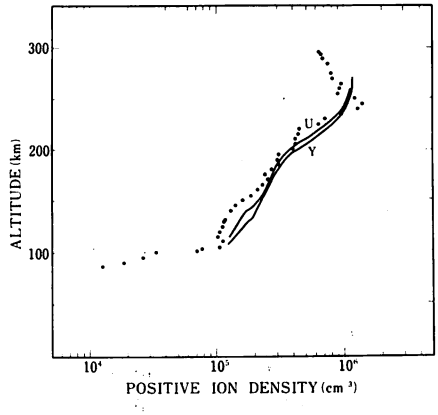


Fig. 56 Positive ion density profile at Kagoshima (K-9M-14, Ascent, Oct. 4, 1965; 12h00m 135°EMT)

e) K-9M-14

The positive ion density profile in the altitude range from 87 km to 299 km was measured with a planar ion trap. The rocket made big precession motion with the half angle of more than 40°. The result is shown in Fig. 56. In this figure the maximum positive ion density in the *E* region appears as clearly as that in the *F* region at noon.

(2) Electron density

a) L-3-2

The electron density profile in the altitude range from 160 km to 1039 km was measured by the resonance probe. Figures 57(a) and (b) show the electron density profiles in the ascending and descending modes. The envelope points in the graph of the resonant frequency versus altitude were used in the case of correction of the resonant frequency. In Figs. 57(a) and (b), the electron density shows nearly constant value about 2×10^4 cm^{-3} above an altitude of 800 km.

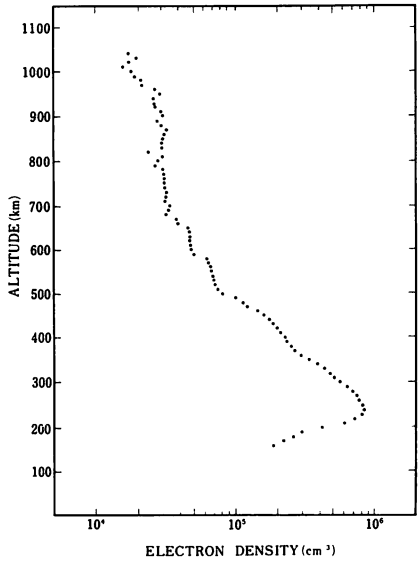


Fig. 57(a) Electron density profile at Kagoshima (L-3-2, Ascent, Jan. 31, 1965; 14h01m 135°EMT)

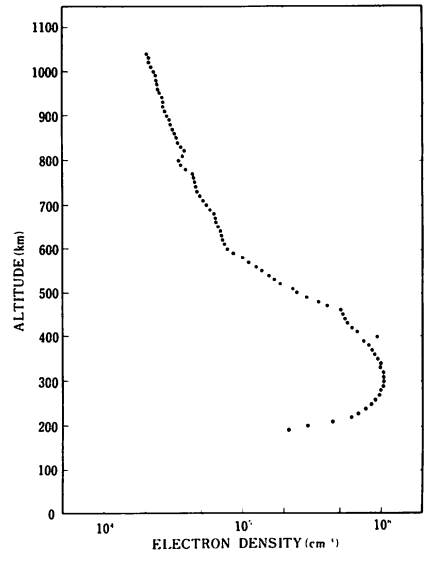


Fig. 57(b) Electron density profile at Kagoshima (L-3-2, Descent, Jan. 31, 1965; 14h01m 135°EMT)

b) L-3-3

The electron density profile in the altitude range from 183 km to 1099 km was measured by the resonance probe. Figures 58(a) and (b) show the electron density profiles in the ascending and descending modes. In Figs. 58(a) and (b), the electron density shows nearly constant value of $1\text{-}1.5 \times 10^4$ cm^{-3}, in comparison with the profile by L-3-2 which was fired at 1401 hours in winter.

c) K-9M-9

The electron density profile in the altitude range from 112 km to 338 km was measured by the resonance probe. Figure 59 shows the electron density profile.

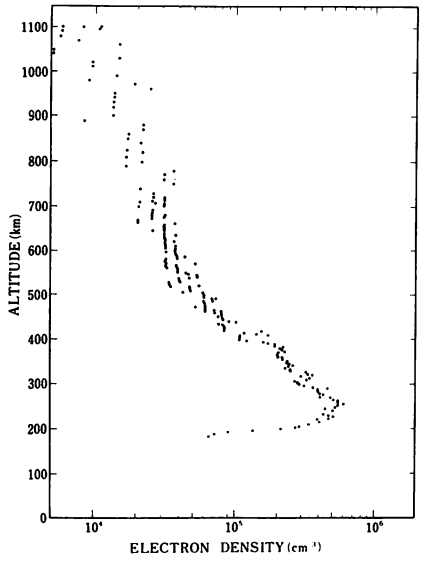


Fig. 58(a) Electron density profile at Kagoshima (L-3-3, Ascent, Mar. 18, 1965; 19h07m 135°EMT)

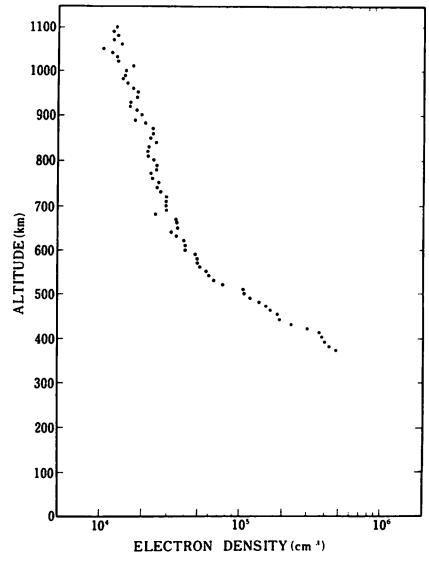


Fig. 58(b) Electron density profile at Kagoshima (L-3-3, Descent, Mar. 18, 1965; 19h07m 135°EMT)

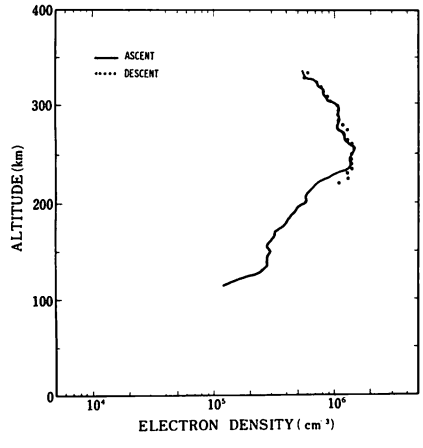


Fig. 59 Electron density profile at Kagoshima (K-9M-9, Mar. 27, 1965: 14h01m 135°EMT)

3.2.4 Summary and Discussions

(1) Positive ion density

The measurements of the positive ion density by three rockets, L-3-3, K-9M-8 and K-8-12, were carried out about 1900–2000 hours local time, the former two being in flight in March, so it is interesting to compare both results. Figure 60 shows both results, including the result by the rocket K-8-12. In this figure, an interesting variation by recombination with electrons is seen in the positive ion density profiles. Indices K_p were 0_0 and 4_+ during the flight of L-3-3 and K-9M-8 respectively and they seemed to be quiet and fairly disturbed. On the other hand, in the daily variation of f_0F2 at Yamagawa, the firing times of L-3-3 and K-9M-8 were before and after the constant value setted at night respectively. The E_S layer observed by the rocket K-8-12 showed a thin plate structure as shown in Fig. 60, and has the difference of more than one order in the positive ion density between the basis and the peak.

Next, it is interesting to compare the results of observations of the positive ion density by the rockets K-9M-13 and -14 which were fired around noon in July and October respectively. Figure 61 shows both results. In this figure, two curves approximately coincide with

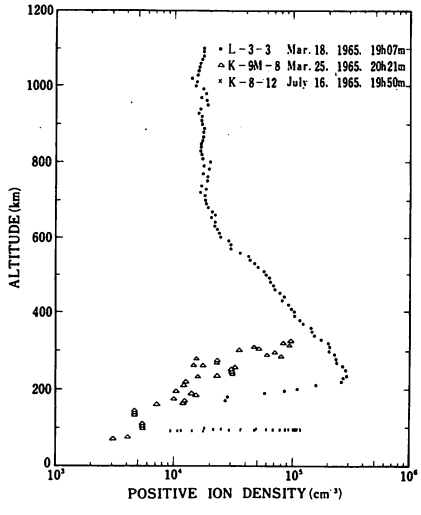


Fig. 60 Positive ion density profiles in the nighttime at Kagoshima

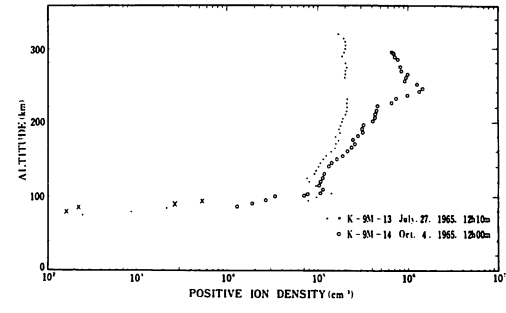


Fig. 61 Positive ion density profiles in the daytime at Kagoshima

each other in the E region, but in the F region one scarcely shows a maximum ion density, while the other shows it clearly. The K_p indices were 2_- in the former and 1_- in the latter, and so much difference was not found. The conditions of the ionosphere were regarded as quiet in both periods. Therefore, the difference appearing in the figure may be due to the seasonal variation owing to the atmospheric temperature or the flux intensity of the solar radiation.

Figure 62 shows the summarized results of the charged particle density profiles, positive ion density N_p and electron density N_e, around noon during the IQSY. One profile observed in summer is far from other four profiles which are similar mutually.

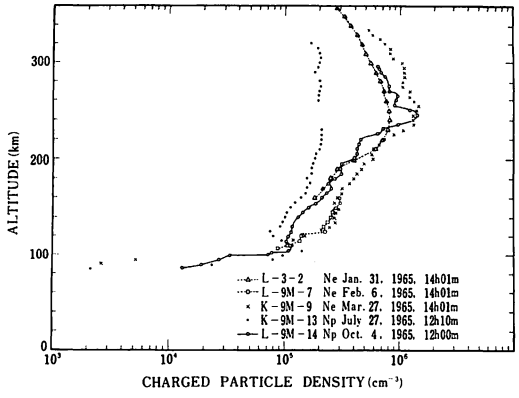


Fig. 62 Charged particle density profiles at Kagoshima

(2) Electron density

The electron density measurements by the resonance probe in the ascending and descending modes of both rockets L-3-2 and -3 were successfully performed, and it is interesting to compare both results. Electron density above 600–700 km is nearly equal to each other, but below that level the electron density by L-3-3 is lower than by L-3-2 by constant ratio. The maximum electron density appears at 250 km, and the decreasing ratio of the electron density changed abruptly at an altitude of about 500 km in the ascending mode. In the descending mode, the electron density above 800 km is equal to each other, and the maximum electron density exists at an altitude of about 350 km which is higher than in the ascending mode by 100 km. Furthermore, for both L-3-2 and -3, the electron density in the descending mode is higher than in the ascending mode especially this fact is remarkable below 800 km for L-3-2 and below 500–600 km for L-3-3. This effect is due to the change of the geomagnetic latitude, because the dropping point is different from the firing point over 1800 km, and the geomagnetic latitude changes by ten degrees toward the equator. Table 4 shows the scale height, transition altitude from O^+ to He^+, mean temperature, maximum electron density and F peak altitude. For L-3-2, K-9M-7 and -9, the firing times were around 1400 hours. The altitudes of the maximum electron densities by L-3-2 and K-9M-9 are 250 km but the value of the maximum electron density by K-9M-9 is rather higher than by L-3-2. However, the electron density profiles in the lower region are nearly the same. In the case of K-9M-7, measurement could be performed only in the altitude region between 107 km and 160 km and the profile was nearly the same as K-9M-9. (Hirao and Miyazaki, 1963a, 1965; Miyazaki, 1966).

3.3 Relation between Sunspot Number and Charged Particle Density in the Upper Ionosphere

Table 4 Quantities related to the electron density measured by rockets L-3-2 and -3

		Ascent			Descent		
		O^+ region	Transition altitude	He^+ region	O^+ region	Transition altitude	He^+ region
L-3-2 1965, 1. 31, 14h01m	H $\frac{Te+Tp}{2}$	110– 158(km) 1050–1500(°K)	550 (km)	450– 610 1070–1450	88– 90(km) 830–860(°K)	605 (km)	334– 380 790– 900
L-3-3 1965, 3. 18, 19h07m	H $\frac{Te+Tp}{2}$	109– 140(km) 1040–1330(°K)	538 (km)	390– 550 900–1310	80– 96(km) 760–910(°K)	573 (km)	442– 600 1050–1430
		h_{max} (km)	N_{max} (cm^{-3})		h_{max} (km)	N_{max} (cm^{-3})	
L-3-2		240	8.5×10^5		345	1.05×10^6	
L-3-3		255	6×10^5		(<370)	($>5 \times 10^5$)	

Table 5 Ionospheric sounding rockets at Kagoshima Space Center, 1966–75

Rocket	Date	Time (135°EMT)	Peak altitude (km)
L-3H-1	Mar. 5, 1966	13^h50^m	359
K-9M-15	Mar. 20, 1966	21 15	307
L-3H-2	July 23, 1966	15 35	1824
K-9M-20	Oct. 20, 1966	17 25	358
K-10-4	Jan. 14, 1969	19 00	231
L-3H-5	Sept.19, 1970	20 30	2017
K-9M-30	Jan. 16, 1971	16 15	357
K-9M-38	Feb. 22, 1972	15 00	352
S-310-2	Aug. 30, 1975	13 10	191

3.3.1 Introduction

The ionospheric observations in the daytime and the nighttime were carried out four sounding rockets; K-9M-15, -20 and L-3H-1, -2 in 1966, since the IQSY. No sounding rocket could be launched during April, 1967 – August, 1968, because of a conflict with fishermen, and no data were obtained from rocket observations. IASY began from January, 1969 and finished on December, 1970. The ten ionospheric sounding rockets were fired during 1969–75. Five L-3H rockets and three K-9M rockets were contained in these experiments. The main object of the L-3H rocket observation was the ionospheric measurement by using a retarding potential analyzer, and the main object of K-9M rocket observation was to measure the electromagnetic property of the ionospheric plasma. A development of the single stage

rocket has been carried out to make the firing operation easy and also to avoid an interference with fishing in the vicinity of the rocket range. The rocket S-310 is used for the ionospheric sounding at the Japanese Antarctic base, Syowa Station. The ionospheric observations by the vertical incidence sounding from the ground were carried out at Uchinoura and Yamagawa Radio Wave Observatory simultaneously with the rocket observation.

Table 5 shows the specifications of the sounding rockets. The results from the retarding potential analyzers were compared with those from the radio frequency probe and the electrostatic probes by the L-3H rockets.

3.3.2 Instruments

(1) L-3H-1

The ionospheric instruments were mounted on the second booster stage. The positive ion density was measured by Langmuir probe method and the ion trap method. The ion density was calculated from the current collected by the solid spherical probe to which two kinds of constant DC voltages of −11.2 V and −24.3 V were alternately applied. The ion density was also calculated from the ion current of the collector in the ion trap. The electron density was obtained from the current-voltage characteristic of the grid in the ion trap. The effective surface area of the grid was 10% of the total surface area of the ion trap.

(2) K-9M-15

The ion density was calculated from the current collected by the solid spherical probe to which a constant DC negative voltage of −24.1 V was applied.

(3) L-3H-2

The observing items and instruments were the same as in K-9M-15, except the meshed spherical probe to which the two kinds of constant DC negative voltages of −10.6 V and −24.0 V were applied.

(4) K-9M-20

The observing items were the electron density and ion density. The electron density was obtained by the resonance probe method. The ion density was obtained by the meshed spherical probe to which a constant negative DC voltage of −24.5 V was applied.

(5) K-10-4

The observing item was the electron density in the nighttime ionosphere. The electron density was calculated by the solid spherical probe 2 cm in diameter to which a constant DC positive voltage of 3.9 V was applied. The fine structure of the electron density profile can be obtained.

(6) L-3H-5

A retarding potential analyzer was mounted on this rocket to measure the ion density and electron density. The sensor was mounted on the top of the payload.

(7) K-9M-30 and -38

The objects of the measurements were to observe the electron density in the E and F regions and to measure complex impedance of ion sheath. The ion sheath has a great effect on radio frequency electric field for frequency lower than plasma frequency. Furthermore, it was one of objects to make a comparison between two-wire radio frequency probe and the impedance probe. Two-wire probe and single wire probe were used to measure a radio frequency characteristic. Single wire was also used as Langmuir probe for the rocket K-9M-30. And for K-9M-38, a proper Langmuir probe was used in addition to the two sets of radio frequency probes.

(8) S-310-2

The primary object was to measure the electron density and electron density irregularities in the E region and E_S layer. There were three cylindrical probes; Langmuir probe, electron current probe and plasma noise probe. In order to avoid the hysteresis effect in usual probe measurement, two glass sealed Langmuir probes (Oyama, 1975) were used for the electron density and temperature measurements.

3.3.3 Observational Results

(1) L-3H-1

The positive ion density profile was measured by the ion trap method in the altitude range from 125.5 km to 358.4 km. In calculation of the ion density from the ion current, the angle between the direction of motion of rocket and the perpendicular to the surface of the ion trap must be known. The data on the angle were obtained of the geomagnetic aspectmeter. From the data, a change in angle was rather small in the ascending mode, but rather big in the descending mode. Therefore, the measurement of the ion density profile was also measured by Langmuir probe from the altitude of 115.0 km to 358.5 km in the ascending mode and from the altitude of 358.5 km to 118.0 km in the descending mode. Two kinds of negative voltages of −11.2 V and −24.3 V were alternately applied to the probe. Figures 63(a) and (b) show the positive ion density profiles in the ascending and descending modes. In these figures, the circular points and cross marks indicate the maximum and minimum values of the changes accompanied by the spin and precession motions of the rocket.

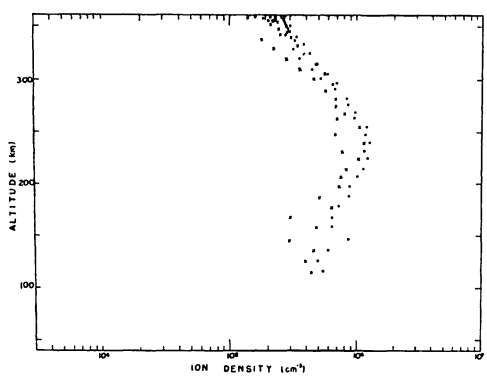


Fig. 63(a) Positive ion density profile at Kagoshima (L-3H-1, Ascent, Mar. 5, 1966; 13h50m 135°EMT)

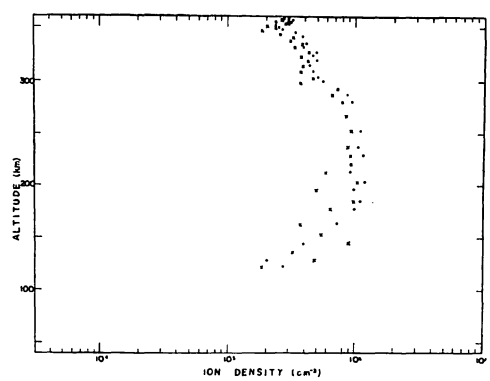


Fig. 63(b) Positive ion density profile at Kagoshima (L-3H-1, Descent, Mar. 5, 1966; 13h50m 135°EMT)

(2) K-9M-15

The positive ion density profiles were measured from 66 km to 307 km in the ascending mode and from 307 km to 137 km in the descending mode by the ion trap method. The ion current to the probe was saturated above 250 km owing to the high gain of the amplifier. The ion density profile in the ascending mode is shown in Fig. 64 which also shows the results obtained by the vertical incidence sounding.

(3) L-3H-2

Figure 65 shows the ion density profile. The dotted curve above 1400 km in this figure shows the result of impedance probe measurement and the dotted curve in the lower part shows the result obtained by the vertical incidence sounding.

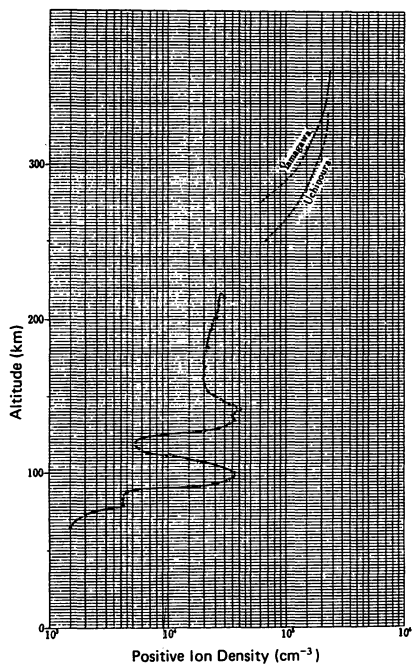


Fig. 64 Positive ion density profile at Kagoshima (K-9M-15, Ascent, Mar. 20, 1966; 21h15m 135°EMT)

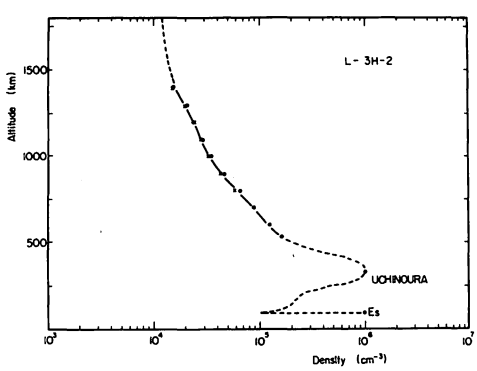


Fig. 65 Positive ion density profile at Kagoshima (L-3H-2, Ascent, July 23, 1966; 15h35m 135°EMT)

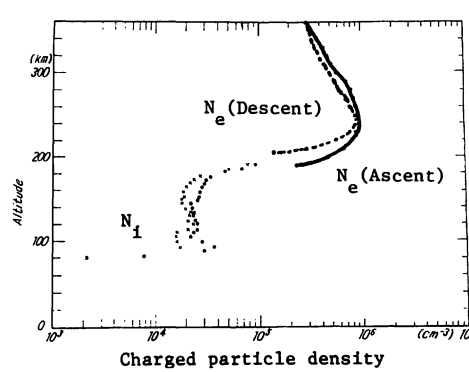


Fig. 66 Charged particle density profile at Kagoshima (K-9M-20, Oct. 20, 1966; 17h25m 135°EMT)

(4) K-9M-20

The electron density profile in the altitude range from 190 km to 358 km was measured by the resonance probe. The positive ion density profile in the altitude range from 78 km to 358 km was measured by Langmuir probe method. The ion current of the probe in the ascending and descending modes indicate maximum and minimum values of changes accompanied by the spin and precession motions of the rocket, and the ion current was saturated near the maximum ion density both in the ascending and descending modes due to the high gain of the amplifier. In calculation of the ion density from the ion current, the rocket velocity, the ion mass, the ion temperature must be known. Figure 66 shows the ion density profile and electron density profiles obtained by the resonance probe (solid and dashed lines).

(5) K-10-4

The observation of the electron density was begun from an altitude of 80 km after the firing. In this flight, the continuous electron density profile, but relative one was calculated from the saturated electron current of the probe.

Figures 67(a) and (b) show the electron density profiles. The slow increasing in electron

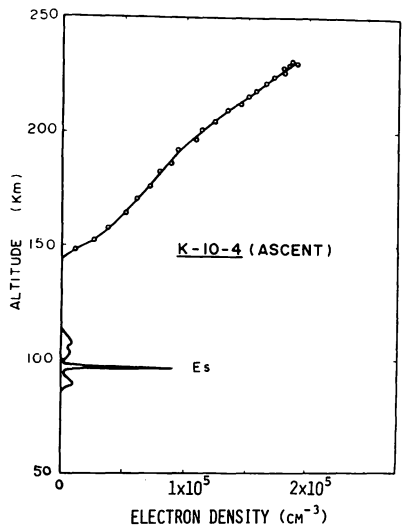


Fig. 67(a) Electron density profile at Kagoshima (K-10-4, Ascent, Jan. 14, 1969; 19h00m 135°EMT)

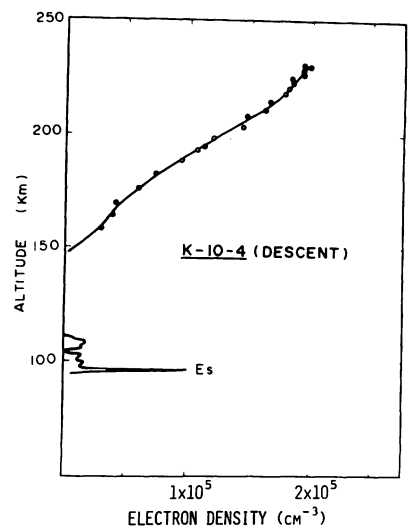


Fig. 67(b) Electron density profile at Kagoshima (K-10-4, Descent, Jan. 14, 1969; 19h00m 135°EMT)

density of the lower F region and sharp E_S layer were characterized in these observational results. E_S layers were observed in the altitude range between 86 km and 112 km in the ascending mode and between 95 km and 111 km in the descending mode, and the altitude of the peak electron density was nearly 96 km, this was coincided with the ascending and descending modes, and the thickness was from 1 km to 1.5 km. Background density was about one-tenth of the peak density, furthermore the shape of the structure of the E_S layer

was very similar to each other in the ascending and descending modes. And at least this layer structure was extended over 300 km in horizontal length. Usually, this layer structure of E_S like this result is characterized in daytime E_S profile, but this experiment showed that the layer E_S type was appeared even in the nighttime.

(6) L-3H-5

A planar retarding potential trap was mounted on the rocket. The normal ion current could not be obtained by the trouble of the line disconnection, so the ion density and temperature could not be analysed. On the other hand, the electron density and temperature were obtained from the electron current-voltage characteristic of the grid. The measurement began from 103 sec after the firing. Figure 68 shows the electron density profile in the

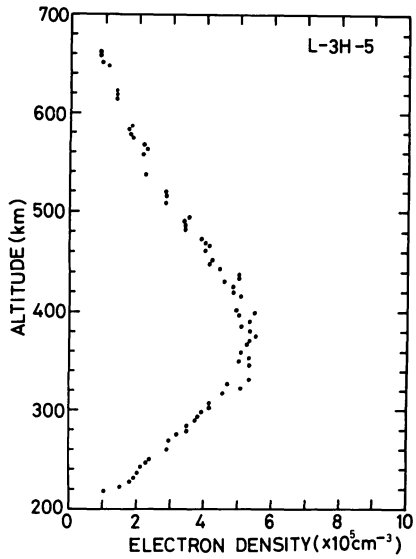


Fig. 68 Electron density profile at Kagoshima (L-3H-5, Ascent, Sept. 19, 1970; 20h30m 135°EMT)

altitude range from 209 km to 700 km. There exists the maximum electron density at an altitude of about 370 km. The electron saturation current shows the maximum value at an altitude of about 375 km. The electron saturation current decreases monotonically above that altitude. It is difficult to analyse the data from about 600 sec after the firing because of the severe telemetry noise. The rocket potential decreases to the minimum value of about 2.5 V from 4.5 V after the commencement of the measurement, after that value again increases and shows about 5.5 V above 300 km. The value of 5.5 V is rather higher than that of other rocket. When the pulse with a frequency of 240 kHz and with an amplitude of 2000 V was transmitted, the rocket potential decreased remarkably and the electron current became zero.

(7) K-9M-30 and -38

The rocket K-9M-30 was fired at 1615 hours on January 16, 1971. Measurement of the electron density in the ionosphere in the altitude range from 100 km to 350 km was carried out by the radio frequency probe method. Three cylindrical probes were mounted on the main rocket. A single wire probe, one of the radio frequency probe, showed good performance but two-wire probe system showed not so good results because that the probe extension was not carried out as the time schedule. The maximum electron density was about 8×10^5 cm^{-3} at an altitude of about 260 km. Furthermore, the triangular wave from 0 to 6 V in the period of 16 sec is superimposed on the probe in addition to the radio frequency voltage. Change of the radio frequency characteristic by the sheath dimension can be investigated. As a result of measurement, the frequency of the sheath resonance changes remarkably by bias voltage of the probe, but the upper hybrid frequency does not change. Figures 69(a) and (b) show the electron density profiles in the ascending and descending modes.

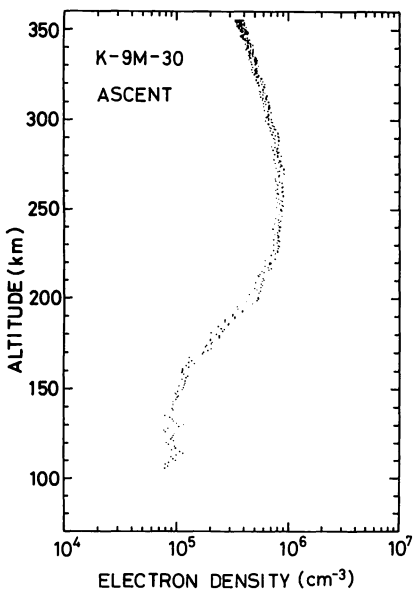


Fig. 69(a) Electron density profile at Kagoshima (Jan. 16, 1971; 16h15m 135°EMT)

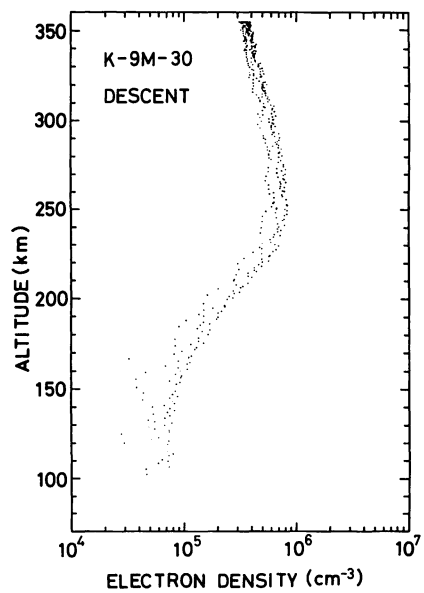


Fig. 69(b) Electron density profile at Kagoshima (Jan. 16, 1971; 16h15m 135°EMT)

The rocket K-9M-38 was fired at 1500 hours on February 22, 1972. In order to measure the electron density and temperature in the ionosphere, two-wire probe and single wire probe which were a kind of a radio frequency probe were mounted on the top of the main rocket. All probes showed good performance and measurements were made from an altitude of 90 km to 352 km. Two-wire probe and single wire probe measurements gave the mutual impedance of the ionospheric plasma. Figures 70(a) and (b) show the electron density

profiles in the ascending and descending modes, and also show the results obtained from the impedance probe. The values of f_0F2 at Yamagawa are shown in this figures. The electron density measurements with two-wire radio frequency probe are compared with those of Langmuir probe, and they showed good agreement each other.

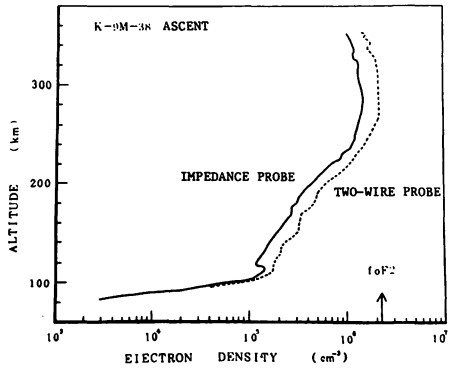


Fig. 70(a) Electron density profiles at Kagoshima (Feb. 22, 1972; 15h00m 135°EMT)

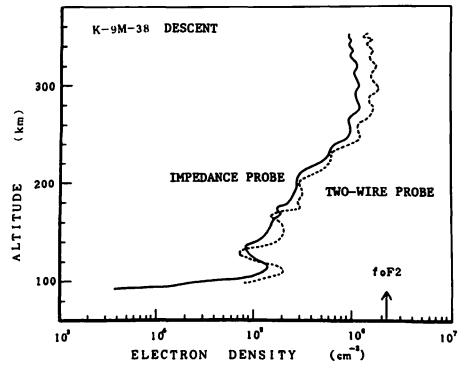


Fig. 70(b) Electron density profiles at Kagoshima (Feb. 22, 1972; 15h00m 135°EMT)

(8) S-310-2

Figure 71 shows the electron density profile in the ascending mode. The electron density profiles calculated from Langmuir probe and electron current probe are good coincidence with each other. By the result of the electron current probe there appears the sudden decrease in the electron density. In this region the measurement by the noise probe shows that there is distinguishable noise with rather big amplitude. The electron density is decreasing very slowly above about 150 km. In the descending mode, the electron density profile shows rather constant value above about 110 km.

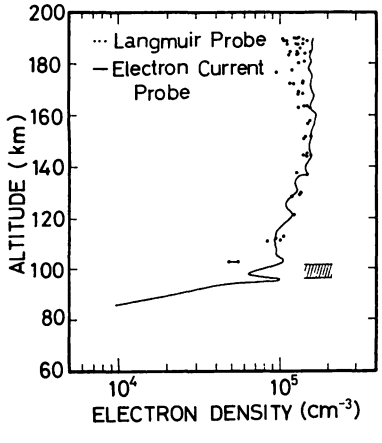


Fig. 71 Electron density profile at Kagoshima (S-310-2, Ascent, Aug. 30, 1975; 13h10m 135°EMT)

3.3.4 Relation between Sunspot Number and Charged Particle Density

Properties of the ionosphere are remarkably controlled by solar activity. The dependence of maximum electron densities of each ionospheric layer; E, $F1$ and $F2$ on solar activities, has been examined by many investigator. They have used data obtained over a long period by ground ionosonde and have derived relations between the densities and sunspot number. These comparisons were possible because bottom side ionospheric data could be obtained by the long-term operated ground based ionosonde. Space vehicle has made it possible to measure electron density in the topside ionosphere. Among these probes, the Alouette satellite is the most famous for its study of the topside ionosphere. Some theories on the profiles of electron density in the topside ionosphere, geomagnetic control (Chandra and Goldberg, 1964) and diffusive equilibrium distribution (Angerami and Thomas, 1964) have been shown to be in good agreement with observed data.

In this section, the data obtained by the Lambda rockets (Miyazaki *et al.*, 1966), the Alouette satellite (Chan *et al.*, 1966), the US rocket at Wallops Island (Jackson and Bauer, 1961; Bourdeau, 1962), and the USSR data (Newell, 1960) were used to examine sunspot cycle dependency on charged particle density in the topside ionosphere in the altitude range between 400 km and 1000 km. Ionospheric observation with rockets or satellites has already continued for almost one solar cycle.

The solar activity dependencies in the ionosphere of E, $F1$ and $F2$ layers have been investigated by Davis (1965), and Kasuya and Sawada (1956) as follows;

$$\begin{cases} f_0(E) = 0.9[(180 + 1.44R)\cos\chi]^{0.25}\ \text{MHz}, \\ f_0(F1) = (4.3 + 0.01R)(\cos\chi)^{0.2}\ \text{MHz}, \\ f_0(F2) = 4.707(1 + 0.0074R)\ \text{MHz}. \end{cases} \quad \cdots\cdots\cdots\cdots\cdots\cdots\cdots\cdots \quad (87)$$

The first two formulae give the maximum electron plasma frequency in the E and $F1$ layers as expressed in the brackets, where R and χ are sunspot number and solar zenity angle, respectively. The last formula was obtained by using the data observed at noon at Yamagawa. Following these expressions, the relations between electron plasma frequency coinciding with electron density, bewteen about 12 hours and 15 hours local time, and sunspot number at intervals of 100 km from 400 km to 1000 km have been approximated by the linear relation of the form of $f = f_0(1 + bR)$ here. An example of relation diagrams is shown in Fig. 72. The data in the middle latitudes were used here. Though the Alouette data at Quito were adopted, these data seem to be always higher than the average data. The scatter of these data is considered to be caused by geomagnetic activity and by the slight difference in time and dip latitude. However, the solar activity dependency of these data seems to coincide with other data, as is seen in the lower envelope of their plots. Both f_0 and b shown in Table 6 are plotted in Fig. 73 as a function with height. As f_0 is an electron density in the case of zero sunspot number, f_0 value versus height represents a topside profile of electron density in the very quiet sun period. The quantity b is a factor of sunspot number dependency. It is noticeable that b is not a monotonic function with height, but has a maximum at the level of 500 km, which is sometimes used as a reference level in the discussion of topside ionosphere. In the present analysis, however, it seems more reasonable to define the level of 400 km as the lowest reference level. Because in Fig. 73, one can find that the inflection point in the curve of f_0 is in the level of 400 km, and no ionization or electron production seems to exist in a higher layer than this inflection point. Angerami and Thomas (1964) discussed the electron density profile in the exosphere by means of their

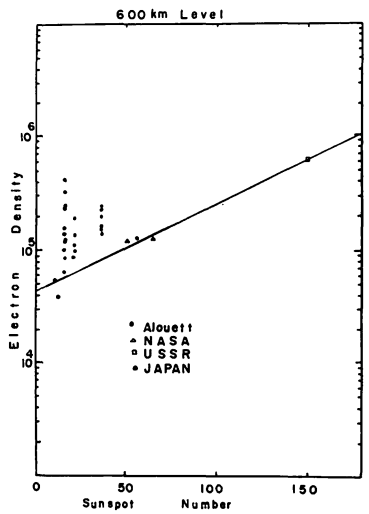


Fig. 72 Relation between sunspot number and observed electron density

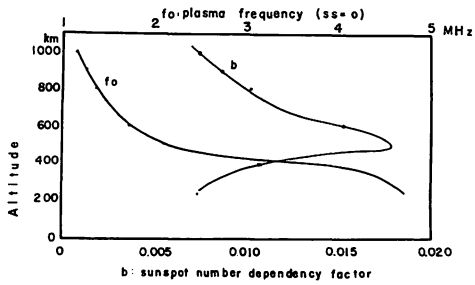


Fig. 73 Height profiles of sunspot dependency factor b and plasma frequency f_o in the case of $R = 0$

Table 6 Values of the function $f = f_o\,(1 + bR)$.

h	f_o	b
1000 km	1.15	0.0074
900	1.26	0.0087
800	1.36	0.0102
700	1.54	0.0115
600	1.72	0.01525
500	2.10	0.01785
400	3.81	0.01055
*	4.707	0.0074

* in $F2$ at Yamagawa

diffusive equilibrium theory. They concluded that the electron density profile was determined not only by temperature but also by ion composition at the exospheric base level, the reference level being 500 km.

Now one can calculate average electron density profiles of the topside ionosphere by means of the obtained f_o and b values in the cases of 0, 50, 100, 150 and 200 of R, respectively, which are shown in Fig. 74. These show a fairly systematic change according to sunspot number, i.e. solar activity. To estimate the scale height of each distribution, electron density profiles are normalized by making the electron density at 400 km level unity. In

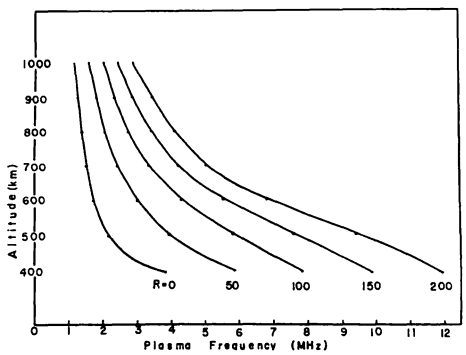


Fig. 74 Electron density profiles in the topside ionosphere. Parameters are sunspot numbers

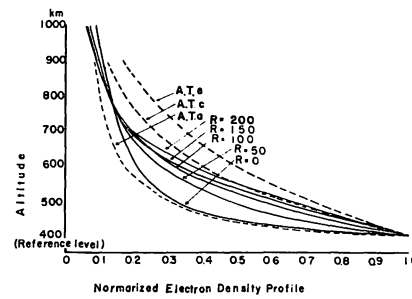


Fig. 75 Normalized electron density profiles. R is sunspot number. A.T. means the theoretical curve derived by Angerami and Thomas. a is the case of $T = 500^{\circ}K$, $\eta_2 = 6.3 \times 10^{-2}$, $\eta_3 = 1.6 \times 10^{-2}$; c of $T = 1500^{\circ}K$, $\eta_2 = 2.0 \times 10^{-2}$, $\eta_3 = 1.6 \times 10^{-3}$ and e of $T = 2000^{\circ}K$, $\eta_2 = 2.0 \times 10^{-3}$, $\eta_3 = 1.6 \times 10^{-5}$.

Fig. 75, normalized distributions for the cases of 0, 50, 100, 150 and 200 of R are shown. The theoretical normalized profiles by Angerami and Thomas (1964) were also plotted simultaneously in Fig. 75, though the reference level in their report is not 400 km but 500 km.

From Fig. 75 one can recognize that, if the temperature in the reference level changes from 500°K to 1500°K, according to the sunspot number, the He^+/O^+ number density ratio, η_2 and η_3, should be from 6×10^{-2} and 1.6×10^{-2} to 2×10^{-2} and 1.6×10^{-3}, respectively. The temperature variation described in consistent with the results in CIRA (Hirao and Miyzaki, 1967).

3.3.5 Summary and Discussions

The observational results of the charged particle density obtained by L-3H-1 show that the measurement is strongly affected by the spin and precession motions of the rocket. The observation by K-9M-15 in the nighttime ionosphere shows interesting facts. In the case of ion density measurement, two layers at altitudes of about 100 km and 140 km were observed. And E_s layer was observed at an altitude of about 102 km by the vertical incidence sounding. The layer at an altitude of about 100 km observed by rocket coincides with the E_s layer, the thickness of the layer is over 20 km. The layer around 140 km high in the ascending mode is considered to be the middle layer observed for the first time, and this layer is assumed to exist in the descending mode. Indices K_p and ΣK_p are 2_- and 18_0 on the day, and they seem to be rather disturbed condition.

As the geomagnetic activity index ΣK_p was 8_- on the day of K-9M-20 flight, the observational result in the twilight was a typical example in quiet condition. Figure 76 shows the profiles of charged particle density in quiet condition as observed by K-9M-14, L-3-2 and -3

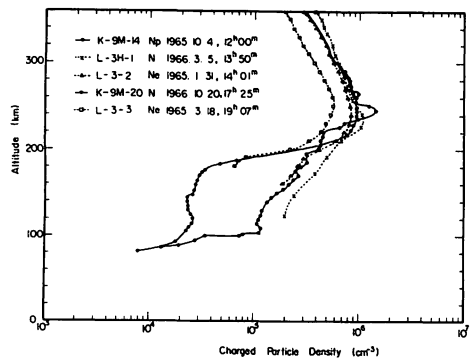


Fig. 76 Comparison of charged particle density profiles

and L-3H-1 including K-9M-20. The observational results by K-9M-14, L-3H-1 and L-3-2 which were fired between 1200 hours and 1400 hours resembled each other, and showed typical profiles of the ionosphere in the daytime. In the case of K-9M-20 fired at 1725 hours, the density in the *E-F* region decreased abruptly, and in the case of L-3-3 fired at 1907 hours, the density also decreased abruptly and the density in the *E-F* region was assumed to be very low (Bourdeau *et al.*, 1965).

As described in the case of L-3H-2, the probe ion current by Langmuir probe with constant negative voltage in the descending mode was far less than in the ascending mode. One of the reasons why the calculated values of the ion density at 300 km were far less than the real values, seems to be charge-up effect, and the effect of charge-up on the rocket body must be considered in the descending mode. The E_S layer exists at 120 km in the descending mode, its ion density being 12.4 times of that in the background (Miyazaki *et al.*, 1966, 1967).

The detailed electron density profiles could be deduced from the radio frequency characteristic by the rocket K-9M-30. There were some differences between the results of two-wire radio frequency probe and impedance probe with whip antenna in K-9M-38 rocket experiment. The maximum electron density deduced from the two-wire radio frequency probe was coincided very well with that deduced from the value of f_0F2 at Yamagawa in ascending mode. The electron density profile by the impedance probe was shifted lower value from that by the two-wire radio frequency probe above about 105 km. These are future problems.

The electron density irregularities in the frequency range from a few Hz to 330 Hz were observed around 100 km in the ascending mode by the rocket S-310-2. The relative amplitudes of the irregularities were of the order of 10% and their frequency power spectrum were $f^{-3.0}$. The most probable production mechanism seems to be the cross-field plasma instability (Mori *et al.*, 1975a,b; Ogawa *et al.*, 1975).

Chapter IV Relation between Lower Ionospheric Electron Density Profiles and Cosmic Noise Absorption during Auroral Zone Disturbances

4.1 Introduction

Upon reopening of the observations of geophysical phenomena at Syowa Station (69°00'S, 39°35'E; geomagnetic lat. 69.6°S, long. 77.1°E), Antarctica by the seventh JARE (Japanese Antarctic Research Expedition) party in 1966, a concrete plan for sounding rocket experiments was made. After the successful rocket flights of S-160JA-1 and -2 by the 11th JARE party as preliminary experiments (Hirasawa *et al.*, 1970), the 12th, 13th and 14th JARE parties carried out firings of a total of twenty-one rockets to observe directly various basic quantities relating to the ionosphere and auroral phenomena at Syowa Station, Antarctica in the period between 1971 and 1973. The electron density profiles in the lower ionosphere under various disturbed conditions were obtained by two S-160JA and twelve S-210JA rocket experiments. Eight of the twelve S-210JA rockets were launched during the night. The observational results of the electron density measurements and discussions are given and general study of the relation between the electron density profile and auroral zone disturbance is described in this chapter.

4.2 Instruments

The radio frequency, Langmuir and electron current probes were installed on the rockets, S-210JA-5, -6, -7, -8, -9, -10, -16, -17 and -18. The radio frequency probe and electron current probe were installed on the rockets S-210JA-11 and -12, and only the electron current probe was installed on the rockets S-160JA-3, -4 and S-210JA-19.

There are calibration systems in the Langmuir probe circuit and in the electron current probe circuit. Electron current calibrations in both electrostatic probes can be made within every 16 seconds of flight. There is also a frequency mark circuit in the radio frequency probe circuit. The frequency can be calibrated during every measuring period. With the radio frequency probe, the error of the absolute value of electron density may be about ±20% (Ejiri *et al.*, 1973). The error in electron density measurement by the Langmuir probe may be slightly larger than that by the radio frequency probe method. With the electron current probe, the relative variations in electron density can be measured with an accuracy of a few percent (Smith, 1966), but the error of the absolute value of the electron density may amount ± a few tens of percent at lower altitudes of small electron density. Here, the electron density above about 90 km is adopted from the results obtained by the radio frequency probe, and the electron density below that level is obtained by the normalization of the results of the electron current probe.

4.3 Observational Results

Table 7 shows the general data concerning the ionospheric sounding rocket experiments and the ionospheric and other conditions. Cosmic noise absorption (CNA) was observed with the riometer at the frequency of 30 MHz. The ionospheric condition was deduced from the ionogram at Syowa Station. In the item; ionospheric probes, symbols EP, LP and RFP mean the electron current probe, the Langmuir probe and radio frequency probe respectively.

Figure 77 shows the electron density profiles observed with the rocket S-160JA-3. The electron density obtained is higher than that of S-160JA-1 or -2 (Hirasawa *et al.*, 1970) throughout the ascending and descending modes.

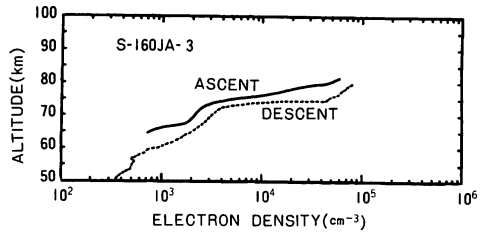


Fig. 77 Electron density profiles at Syowa Station, Antarctica (Apr. 30, 1971; 13h00m 45°EMT)

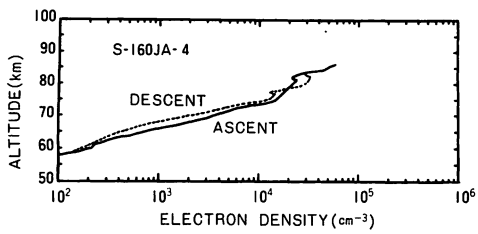


Fig. 78 Electron density profiles at Syowa Station, Antarctica (Apr. 17, 1972; 02h42m 45°EMT)

Table 7 Ionospheric sounding rockets and ionospheric and other conditions during rocket experiments at Syowa Station, Antarctica, 1971–73.

Rocket	Date	Time (135°EMT)	Peak alt. (km)	Ionospheric Probes	Geomag. H-comp. (gamma)	30 MHz CNA (dB)	Ionosphere
S-160JA-3	Apr. 30, 1971	13^h00^m	83	EP			
S-210JA-5	Sept. 14, 1971	00 50	114	EP, LP, RFP	−150	−0.8	E_S
S-210JA-6	Dec. 3, 1971	15 00	131	EP, LP, RFP		−0.8	
S-210JA-12	Feb. 11, 1972	15 00	108	EP, RFP	Quiet	0.0	Quiet
S-160JA-4	Apr. 17, 1972	02 42	86	EP	−320	−1.2	Blackout
S-210JA-9	May 14, 1972	02 13	129	EP, LP, RFP	−290	−1.3	Blackout
S-210JA-10	May 16, 1972	02 02	115	EP, LP, RFP	−200	−0.3	Spread F
S-210JA-11	Aug. 7, 1972	04 45	126	EP, RFP	−600	−4.8	Blackout
S-210JA-8	Aug. 11, 1972	04 01	127	EP, LP, RFP	−450	−2.6	Blackout
S-210JA-7	Dec. 14, 1972	00 23	126	EP, RFP	−200	−1.5	Blackout
S-210JA-16	Feb. 15, 1973	02 45	103	EP, LP, RFP	−300	−1.5	E_S
S-210JA-17	Apr. 23, 1973	02 54	125	EP, LP, RFP	−750	−5.0	Blackout
S-210JA-19	July 15, 1973	22 09	130	EP	− 50	0.0	E_S
S-210JA-18	Aug. 23, 1973	03 53	129	EP, LP, RFP	+ 50	−0.5	Unstable E_S

Figure 78 shows the electron density profiles observed with the rocket S-160JA-4 which was fired in the nighttime. The cosmic noise absorption is 1.2 dB and the deviation of the horizontal component of the geomagnetic field with respect to the quiet level is -320γ. The ionosphere is in rather disturbed condition and the electron density of the ionosphere is high in the lower altitude region between 65 km and 80 km.

Figure 79(a) and (b) show the electron density profiles observed with the rocket S-210JA-5. In the ascending mode, the electron density increases with a steep gradient in

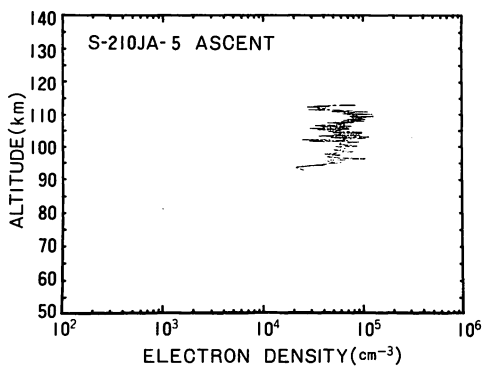


Fig. 79(a) Electron density profile at Syowa Station, Antarctica (Sept. 14, 1971; 00h50m 45°EMT)

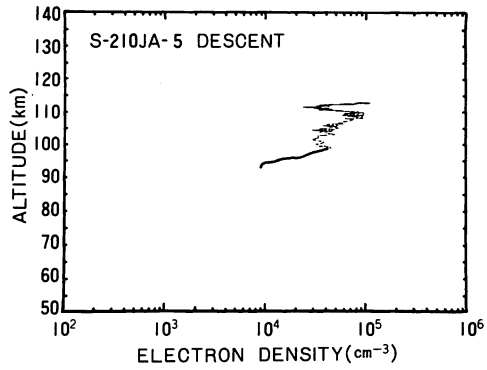


Fig. 79(b) Electron density profile at Syowa Station, Antarctica (Sept. 14, 1971; 00h50m 45°EMT)

the altitude range to about 95 km, then the gradient of the electron density profile becomes rather small above 95 km with an electron density of about 1×10^5 cm^{-3}. In the descending mode, the gradient of the electron density changes at an altitude of about 100 km.

The spin rate of the rocket was about 1 Hz, and there also existed a rather large precession motion of the rocket. The length of the cylindrical electrode was about 50 cm, and the measuring electrodes entered and left the wake region of the rocket during the spin and precession motions. The electron density in the rocket wake region was lower than that of ambient plasma. Therefore, the observed values of the electron density show increases and decreases arising from the spin and precession of the rocket. The most probable profile is derived by connecting the peak values. In Fig. 79(a), there exist three electron density maxima at the altitudes of about 97 km, 103 km and 110 km. The most probable electron density profile is the dashed envelope line from the consideration of electrostatic probe measurements. In Fig. 79(b), the decrease in electron density around 112 km may be caused by the precession effect of the rocket.

Figures 80(a) and (b) show the electron density profiles observed with the rocket S-210JA-6 which was fired in the daytime. The gradient of the electron density below about 88 km is comparatively large, the maximum electron density of 2×10^5 cm^{-3} appears in the altitude region between about 95 km and 105 km, and the electron density decreases above 105 km. The ionospheric condition is in slight disturbance. The reason of the decreases of the electron density around 110 km in the ascending mode and around 125 km in the des-

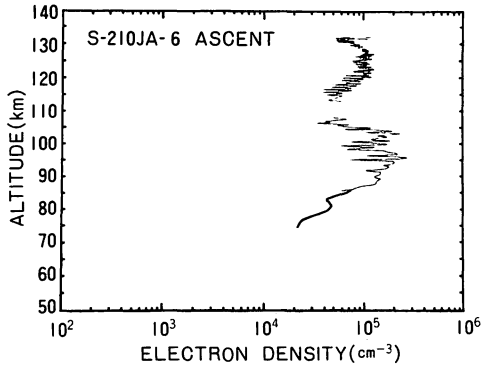


Fig. 80(a) Electron density profile at Syowa Station, Antarctica (Dec. 3, 1971; 15h00m 45°EMT)

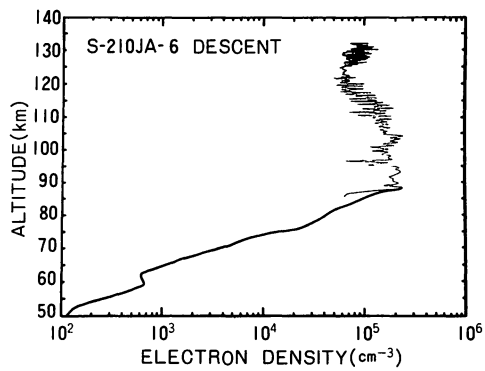


Fig. 80(b) Electron density profile at Syowa Station, Antarctica (Dec. 3, 1971; 15h00m 45°EMT)

cending mode is inferred from the measurement to be affected by the rocket wake.

Figures 81(a) and (b) show the electron density profiles observed with the rocket S-210JA-7. The rocket was fired at the time of a few degrees of the solar elevation angle, therefore the solar ultraviolet and X-rays contribute to the ionization of the upper atmosphere. The profiles of the electron density in the ascending and descending modes are similar to each other. The electron density increases abruptly up to the altitude of about 95 km, the gradient of the electron density above 95 km is low and the maximum electron density of about 3–4 X 10^5 cm^{-3} appears around 110 km. The electron density decreases above 110 km. It is interesting that the gradient of the electron density changes at an altitude of about 85 km. This fact suggests that the ionization mechanism changes at this altitude.

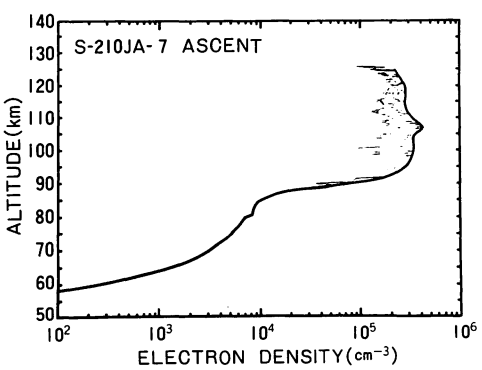


Fig. 81(a) Electron density profile at Syowa Station, Antarctica (Dec. 14, 1972; 00h23m 45°EMT)

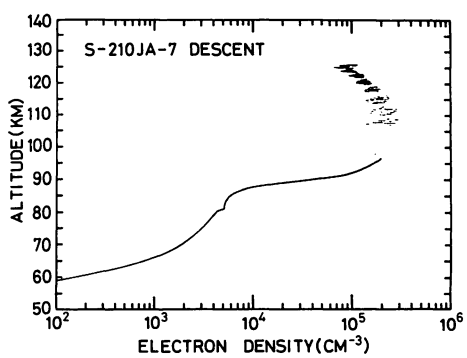


Fig. 81(b) Electron density profile at Syowa Station, Antarctica (Dec. 14, 1972; 00h23m 45°EMT)

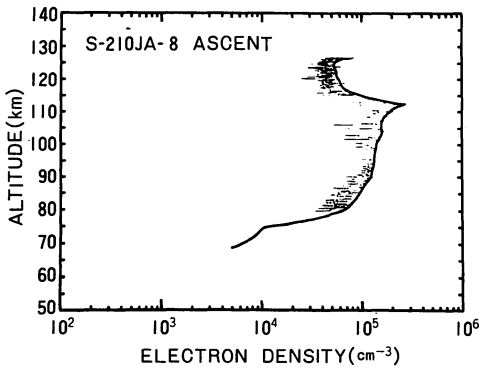


Fig. 82(a) Electron density profile at Syowa Station, Antarctica (Aug. 11, 1972; 04h01m 45°EMT)

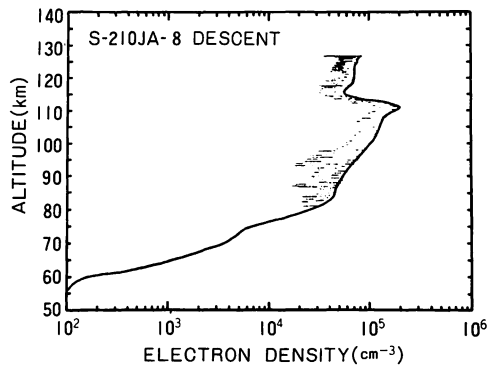


Fig. 82(b) Electron density profile at Syowa Station, Antarctica (Aug. 11, 1972; 04h01m 45°EMT)

Figures 82(a) and (b) show the electron density profiles observed with the rocket S-210JA-8 which was fired in the period of the August event, 1972 (Hakura *et al.*, 1973; Radio Research Laboratories, 1973). The electron density increases with a steep gradient in the altitude up to about 80 km in both the ascending and descending modes; the gradient of the electron density increases rather gradually up to a maximum at an altitude of about 112 km and then decreases with rather steep gradient above 112 km.

Figures 83(a) and (b) show the electron density profiles observed with the rocket S-210JA-9. Although the ionogram shows that there was a radio blackout at the time of firing, it shows the occasional appearance of the E_S layer before and after the firing time. The electron density profiles during the ascent and descent are different from each other.

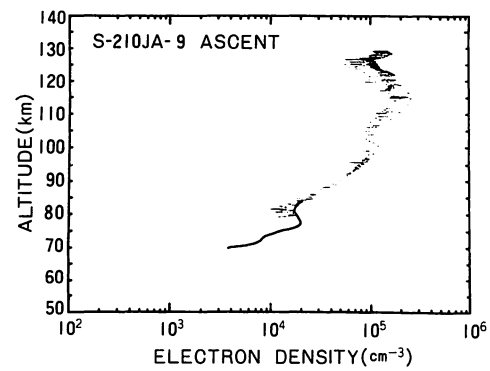


Fig. 83(a) Electron density profile at Syowa Station, Antarctica (May 14, 1972; 02h13m 45°EMT)

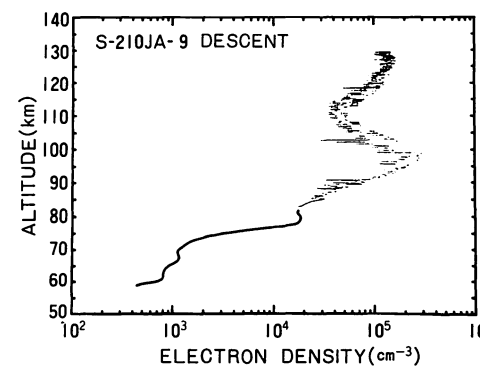


Fig. 83(b) Electron density profile at Syowa Station, Antarctica (May 14, 1972; 02h13m 45°EMT)

That is, the electron density increases monotonically to a maximum at the altitude of about 115 km and is about 2.5×10^5 cm^{-3} in the ascent. The electron density decreases above 115 km. On the other hand, the electron density shows a maximum of about 3×10^5 cm^{-3} and shows a minimum at 110 km during descent. The difference of the electron density profiles in the ascending and descending modes is due to auroral structure. According to the all-sky photographs taken at the same time of the rocket firing, the visible aurora moved northward at first and moved southward later (Ogawa *et al.*, 1975).

Figures 84(a) and (b) show the electron density profiles observed with the rocket S-210JA-10. At the firing time, the disturbance of the ionosphere was rather small and the ionogram shows the existence of spread *F*. The electron density increases with a steep gradient in the altitude range up to about 80 km and the electron density was about 8–10

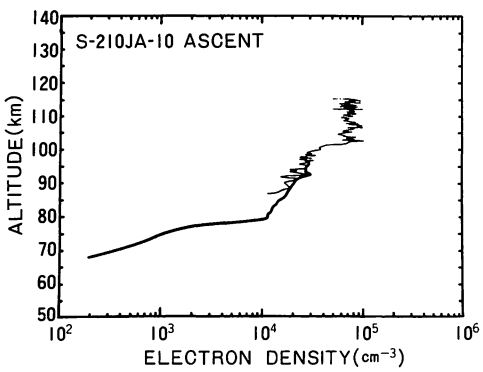


Fig. 84(a) Electron density profile at Syowa Station, Antarctica (May 16, 1972; 02h02m 45°EMT)

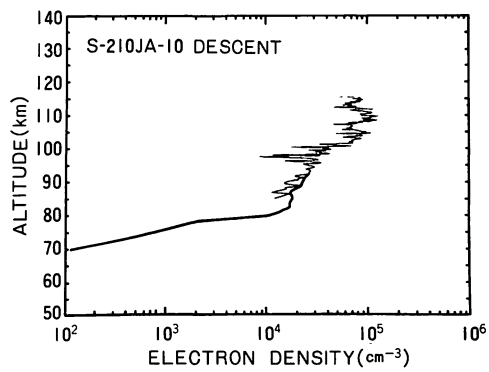


Fig. 84(b) Electron density profile at Syowa Station, Antarctica (May 16, 1972; 02h02m 45°EMT)

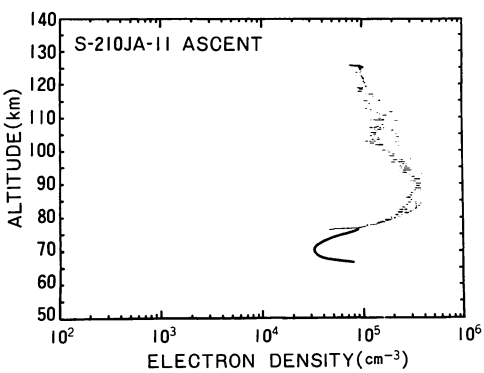


Fig. 85(a) Electron density profile at Syowa Station, Antarctica (Aug. 7, 1972; 04h45m 45°EMT)

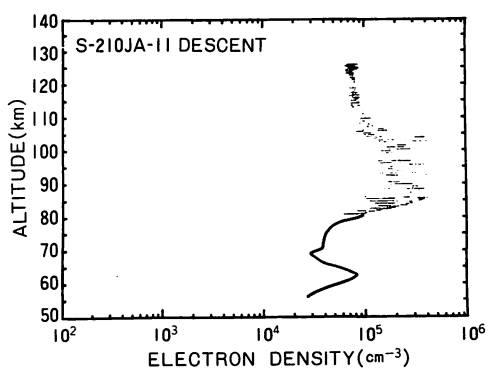


Fig. 85(b) Electron density profile at Syowa Station, Antarctica (Aug. 7, 1972; 04h45m 45°EMT)

$\times 10^4$ cm^{-3} above about 100 km during both the ascending and descending modes.

The electron density profiles as shown in Figs. 84(a) and (b) exhibit irregular shapes. These are partly caused by the wake effect due to the precession of the rocket or the existence of large-scale irregularities in the ionosphere.

Figures 85(a) and (b) show the electron density profiles observed with the rocket S-210JA-11 which was fired in the period of the August event, 1972. In the ascending mode, the electron density increases with a steep gradient in the altitude range up to about 77 km; the electron density increases gradually above 77 km and reaches a maximum of about 4–5 $\times 10^5$ cm^{-3} at an altitude of about 90 km. The electron density decreases gradually above 90 km. In the desending mode, the electron density measurements by the radio frequency probe show saturation in the altitude range between 85 km and 103 km; the electron density is presumed to have a maximum of 4–5 $\times 10^5$ cm^{-3} in that region from the electrostatic probe measurements. The electron density decreases with a steep gradient above 105 km.

Figures 86(a) and (b) show the electron density profiles observed with the rocket S-210JA-12 which was fired in the quiet daytime condition of the ionosphere. The profile

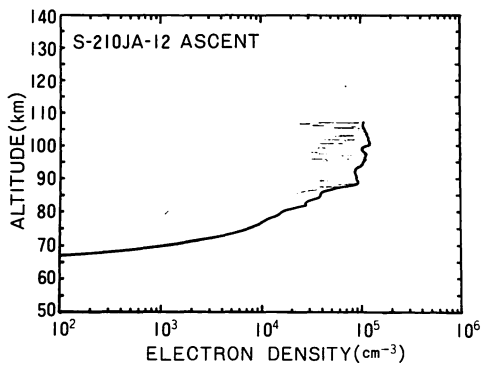


Fig. 86(a) Electron density profile at Syowa Station, Antarctica (Feb. 11, 1972; 15h00m 45°EMT)

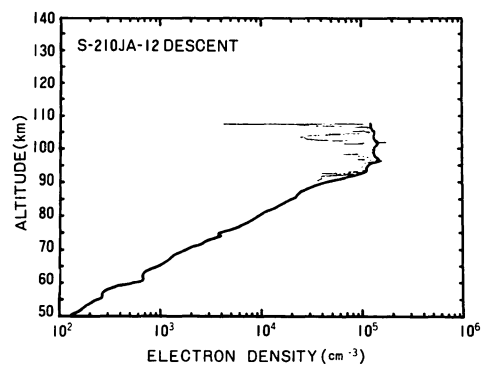


Fig. 86(b) Electron density profile at Syowa Station, Antarctica (Feb. 11, 1972; 15h00m 45°EMT)

shows the typical daytime ionospheric condition. In the ascending mode, the electron density increases abruptly at the altitude of about 88 km, and the electron density remained approximately the constant value of 1–2 $\times 10^5$ cm^{-3} above 88 km. In the descending mode, the electron density increases abruptly at the altitude of about 93 km, and the electron density shows nearly constant value above 93 km. The sudden decrease more than one order in the electron density is considered to be caused by the rocket wake by the abnormal aspect of the rocket.

Figures 87(a) and (b) show the electron density profiles observed with the rocket S-210JA-16 which was fired just before the sunrise at Syowa Station. The electron density increases abruptly at the altitude of 95 km, and the electron density increases gradually or

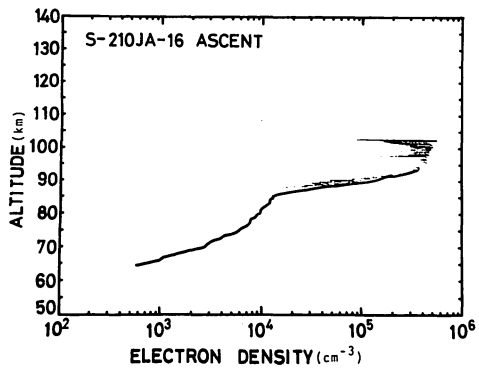


Fig. 87(a) Electron density profile at Syowa Station, Antarctica (Feb. 15, 1973; 02h45m 45°EMT)

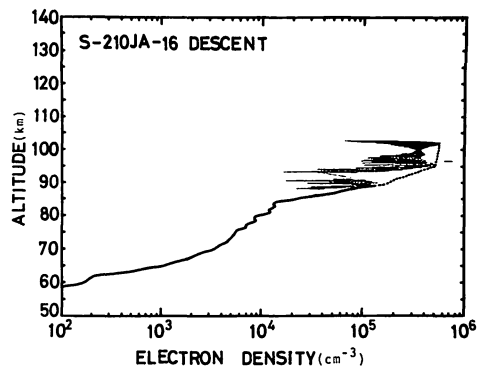


Fig. 87(b) Electron density profile at Syowa Station, Antarctica (Feb. 15, 1973; 02h45m 45°EMT)

remains in the constant value of 5-6 X 10^5 cm^{-3} in both the ascending and descending modes. The gradient of the electron density changes remarkably at 86 km in the ascending mode and at 84 km in the descending mode. The remarkable increase and decrease in the electron density above 90 km in the descending mode as shown in Fig. 87(b) are considered to be due to the affect by the rocket wake.

Figures 88(a) and (b) show the electron density profiles observed with the rocket S-210JA-17. The magnitude of the ionospheric disturbance at the firing time was the largest in these rocket experiments. Since the values obtained by the radio frequency probe in the altitude range between 90 km and 105 km in the ascent show saturation, the electron density was obtained from the measurement by the electron current probe in this region.

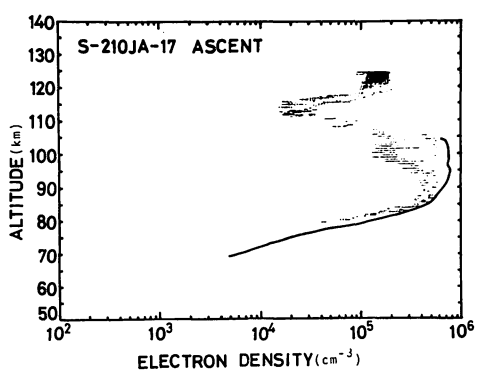


Fig. 88(a) Electron density profile at Syowa Station, Antarctica (Apr. 23, 1973; 02h54m 45°EMT)

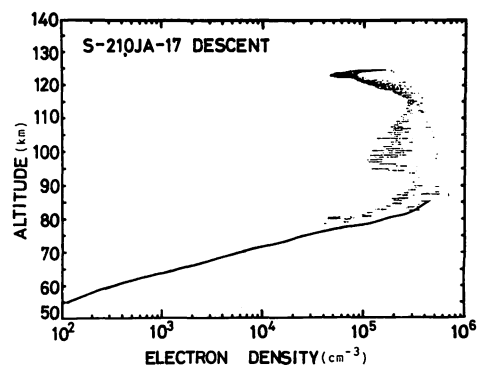


Fig. 88(b) Electron density profile at Syowa Station, Antarctica (Apr. 23, 1973; 02h54m 45°EMT)

The electron density is about 7-8 X 10^5 cm^{-3}. A maximum electron density of 6 X 10^5 cm^{-3} appears in the region between 87 km and 105 km, and the electron density decreases gradually above 105 km during the descent. As described before, the electron density measurements show increases and decreases due to the spin and precession of the rocket. The horizontal lines in the figures show the spread over some range of electron density from the spin effect of the rocket. The spread in the electron density is almost one order of the magnitude. The decreases in the measured electron density in the altitude range between 105 km and 120 km in the ascent and between 121 km and 125 km in the descent are assumed to be partly caused by the rocket wake.

Figures 89(a) and (b) show the electron density profiles observed with the rocket S-210JA-18. This rocket traversed the region of visible aurora around 105 km in the ascent; the maximum electron density is 5.33 X 10^5 cm^{-3} at 103.4 km. In the descending mode, there are decreases and increases in the electron density profile and the maximum electron density is about 1.5 X 10^5 cm^{-3}. The ionosphere is assumed not to be in a severely disturbed condition.

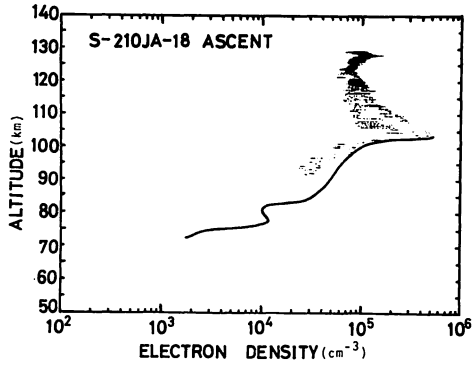


Fig. 89(a) Electron density profile at Syowa Station, Antarctica (Aug. 23, 1973; 03h53m 45°EMT)

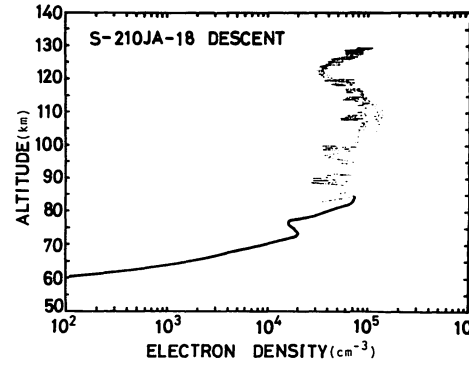


Fig. 89(b) Electron density profile at Syowa Station, Antarctica (Aug. 23, 1973; 03h53m 45°EMT)

Figures 90(a) and (b) show the electron density profiles observed with the rocket S-210JA-19. The maximum electron density is about 1 X 10^5 cm^{-3}. Figure 90(a) shows the existence of the E_S layer around 105 km, but Fig. 90(b) shows no remarkable E_S layer. The cause for this difference is due to the structure of the E_S layer. The ionosphere is rather quiet except for the appearance of the E_S layer.

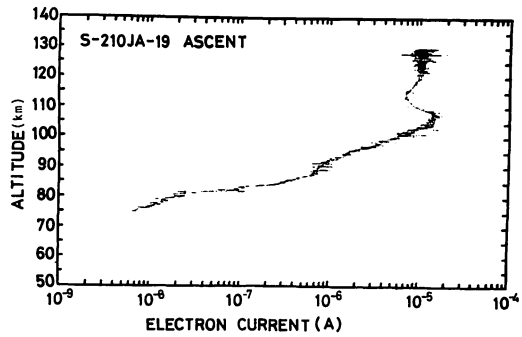


Fig. 90(a) Electron density profile at Syowa Station, Antarctica (July 15, 1973; 22h09m 45°EMT)

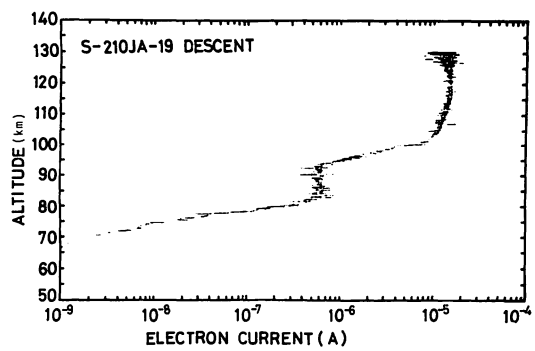


Fig. 90(b) Electron density profile at Syowa Station, Antarctica (July 15, 1973; 22h09m 45°EMT)

4.4 Relation between the Electron Density Profile and the Cosmic Noise Absorption

Figure 91 shows the electron density profiles in the ascending mode when the aurora appears in the nighttime. The author wishes to make clear in the following that the increase in the electron density, especially in the D and E region between about 75 km and 110 km, in proportional to the magnitude of the disturbance such as the variation of the geomagnetic field and cosmic noise absorption.

The collision frequency profile is derived from the electron density profile, and the absorption measurement by the riometer. The collision frequency profile is assumed to be of the log-linear type, that is, $\nu = \nu_0 \exp(-h/H)$, where h is the altitude from the ground level, H is the scale height and ν_0 is a constant (Budden, 1961). The best-fitting curve is derived by the method of least squares. The collision frequency thus obtained is expressed as $\nu = 1.49 \times 10^9 \exp(-h/16.3)$. In this equation, the scale height $H = 16.3$ is large compared with the usual scale height of several km; this is partly caused by the assumption of the simple log-linear collision frequency profile. Figure 92 shows a comparison between observed

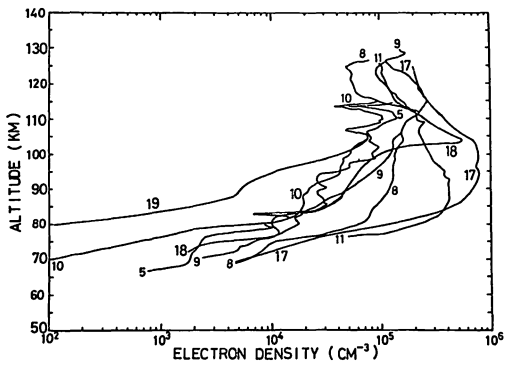


Fig. 91 Electron density profiles during auroral disturbances. The number on curves indicates the serial number of the rocket S-210JA

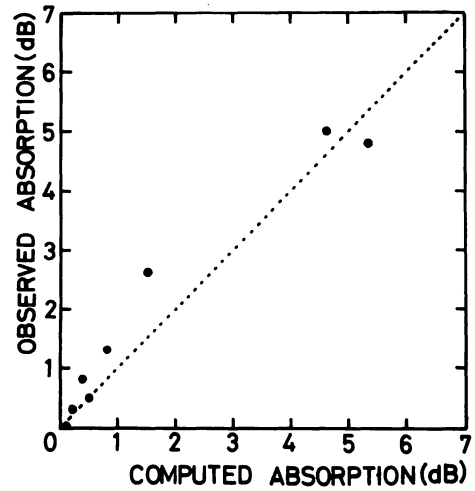


Fig. 92 Comparison between observed absorption and computed absorption

absorption and computed absorption by using the above derived collision frequency profile obtained. Figure 93 shows the collision frequency profile obtained. The collision frequency in the present experiments is lower than that of previous data at lower altitudes, lies at about the midpoint of the values in the middle altitude region, but has a lower value at high altitudes. Figure 94 shows the absorption coefficient profiles at 30 MHz, which are calculated by using the electron density profiles and the collision frequency profile. From this, it is clear that for all of the cases except S-210JA-19, there exists a maximum absorption layer in the region between 75 km and 85 km, and the location of this altitude is not strongly dependent on the magnitude of the ionospheric disturbance. The region above 120 km scarcely contributes to the absorption.

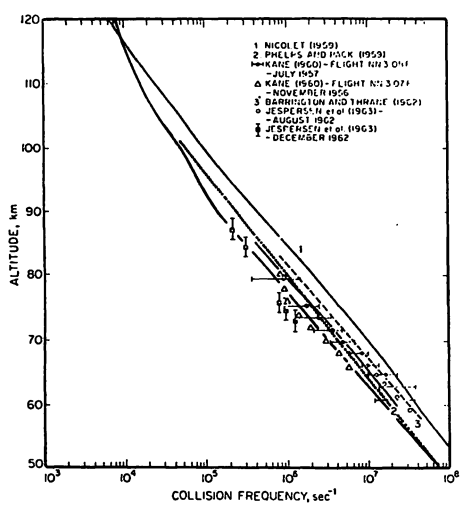


Fig. 93 Collision frequency profiles. The dotted line shows the collision frequency profile which is derived from the best fitting curve of the observational results of electron density measurements and cosmic noise absorption measurements by the method of least squares. Other profiles after Whitten and Poppoff (1965); 1, the upper solid line; 2, the medium solid line; 3, the medium chain line, and the lower solid line are after Hanson (1961).

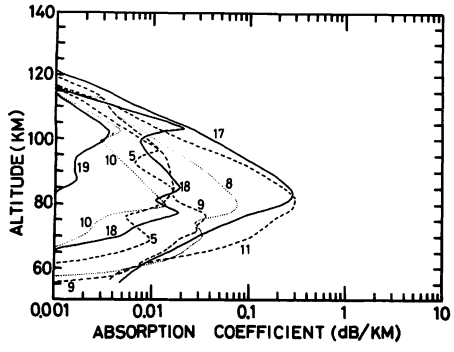


Fig. 94 Absorption coefficient profiles. The number on curves indicates the serial number of the rocket S-210JA.

The ionograms observed at Syowa Station, Antarctica show that an E_S layer almost always exists in the nighttime (Radio Research Laboratories, 1971–1972). Thus, the result obtained by the rocket S-210JA-19 may be assumed to be a typical example of the night E_S layer profile from the consideration of the ionogram, riometer measurement and geomagnetic variation. There exists always an ionizing source of the night E_S in the auroral zone. The energetic particles associated with auroral phenomena increase the electron density, and the increase in the electron density is superimposed on the night E_S layer during the auroral disturbances.

The increment of the electron density is discussed in the following. Figure 95 shows the profiles of the increments of the electron density which are the differences between the electron density observed by each rocket and the electron density obtained by S-210JA-19. From this graph it is clear that all the profiles of the increment of the electron density show nearly the same parabolic-type shape and that the heights of the peak electron density are

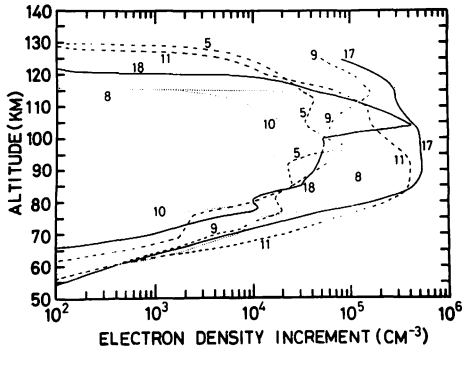


Fig. 95 Profiles of the increment of the electron density. The number on curves indicates the serial number of the rocket S-210JA.

located in the region between 90 km and 100 km. The curve of the electron density increment has double peaks in the cases of S-210JA-8 as well as in the case of S-210JA-18; however, the upper peak is associated with the visible aurora in analogy to the case of S-210JA-18 and is not related to CNA to any great extent. As regards the result by S-210JA-10, the approximation of the electron density around 100 km may not be a good one, so there appears a decrease in the electron density around 100 km.

Figure 96 shows the relation between the maximum increment of the electron density and cosmic noise absorption. The empirical formula which is deduced from this figure is as follows:

$$\triangle n_e = \exp(0.205x + 4.67), \quad \ldots\ldots\ldots\ldots\ldots\ldots\ldots\ldots\ldots\ldots\ldots\ldots\ldots\ldots \quad (88)$$

where $\triangle n_e$ is the maximum increment of the electron density per cm^3 and x is the cosmic noise absorption in dB. The dotted lines to the extreme left of Fig. 96 are measurements for S-210JA-10. They deviate from the straight line; this is partly due to the comparatively small disturbance of the ionosphere.

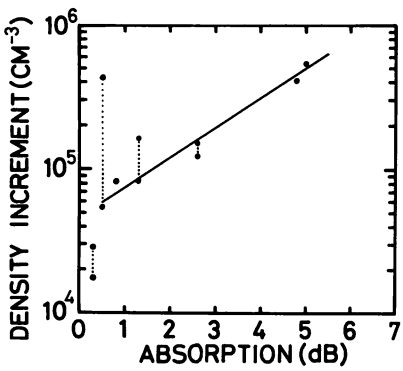


Fig. 96 Relation between the maximum electron density increment and cosmic noise absorption

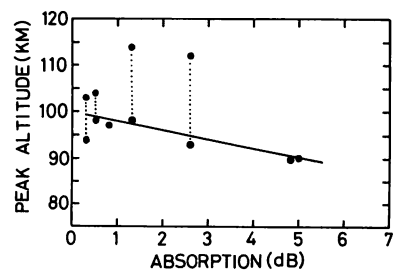


Fig. 97 Relation between the height of the peak of electron density increment and cosmic noise absorption

Figure 97 shows the relation between the height of the peak electron density and cosmic noise absorption. The empirical formula is as follows:

$$h_m = -2x + 100, \quad \ldots\ldots\ldots\ldots\ldots\ldots\ldots\ldots\ldots\ldots\ldots\ldots\ldots\ldots \quad (89)$$

where h_m is reckoned in km.

4.5 Summary and Discussions

In the previous section, the results of the electron density measurements with the rocket experiments by the 12th, 13th and 14th JARE parties are described and also analysis of the relation between electron density profiles and riometer observations are presented.

The rockets S-160JA-3, S-210JA-6 and -12 were fired in the daytime, the rocket S-210JA-7 was fired at low solar elevation angle, the rocket S-210JA-16 was fired just before the sunrise and other rockets S-160JA-4, S-210JA-5, -8, -9, -10, -11, -17, -18 and -19 were fired in the nighttime.

The observed electron density distributions in the polar ionosphere strongly change according to the degree of the disturbance. The electron density profile has a close relation to auroral structures; therefore, there are cases in which the profiles in the ascending and descending modes are different from each other (see, for example, the cases of S-210JA-9 and -18).

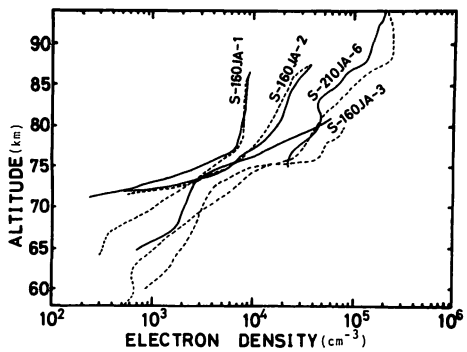


Fig. 98 Electron density profiles in the daytime. The solid and dashed lines indicate the cases of ascent and descent respectively.

Figure 98 show the electron density profiles below about 94 km in the daytime which were observed with the rockets S-160JA-1, -2, -3 and S-210JA-6. Ionograms show the quiet conditions and the records of the cosmic noise absorption show also quiet conditions in the case of S-160JA-1 and -2. But the magnetogram in the case of S-160JA-2 shows small positive bay, and E_S layer exists. In the case of S-160JA-3, the riometer record shows absorption from 0600 hours and at the firing time the cosmic noise absorption was 0.2 dB. In the case of S-210JA-6, by the riometer record at the firing time the cosmic noise absorption was 0.8 dB and the upper atmosphere was rather in disturbed condition (Ogata and Ose, 1972). The electron density profile by S-210JA-5 is not shown in Fig. 98, but the electron density is assumed to be 1×10^2 cm^{-3} at 66 km, 1×10^3 cm^{-3} at 76 km, 1×10^4 cm^{-3} at 86 km. By the record of the riometer, rather abrupt cosmic noise absorption commenced from about 0043 hours, and CNA was 0.8 dB, but the time after and before that time, the riometer record shows quiet condition. As there appears only E_S layer on the ionogram, there exist the absorbing layers. Figure 98 shows that the electron density has a close relation to the ionospheric disturbances.

Comparing the results of S-210JA-5 and -6, the electron density above about 95 km by S-210JA-6 is higher by two or three times than that of S-210JA-5, below that altitude the electron density is higher by one order.

Next, the riometer record shows that CNA was 0 dB at the firing time of S-210JA-12, CNA was 1.2 dB at the firing time of S-160JA-4 and the ionosphere was in slightly disturbed condition. In the case of S-210JA-9, CNA was 1.3 dB and this absorption appeared after the small absorption of 30 minutes, and that absorption continued for about 40 minutes. In the case of S-210JA-11, CNA was 4.8 dB and there appeared large absorption between 0420 hours and 0500 hours. In the case of S-210JA-8, CNA was 2.6 dB and the rather larger absorption continued for a while. In the case of S-210JA-7, CNA was 1.5 dB and the ionospheric condition was comparatively quiet, but the absorption commenced from about 0000 hours (Isozaki and Miyazaki, 1973).

Comparing the results observed with S-210JA-6 and -12, the electron density above 88 km in the case of S-210JA-6 is about twice of that of S-210JA-12. This reason is that S-210JA-12 was fired at quiet condition and S-210JA-6 was fired at slightly disturbed condition. The electron density in the *D* region between 75 km and 90 km in the case of S-210JA-6 is larger than that in S-210JA-12. In the case of S-160JA-3, the electron density at an altitude of about 80 km is much higher than those of the former two cases.

Both the solar ultraviolet radiation and X-rays, and the energetic particles from the exosphere are considered to be ionizing sources of the atmosphere in the cases of S-210JA-7 and -16 since these rockets were fired just before and after the sunrise. The profiles of the electron density distribution in the ascending and descending modes are similar to each other in both cases of S-210JA-7 and -16. The electron density in the case of S-210JA-16 is about twice of that in the case of S-210JA-7 above about 85 km. The fact is inferred from that the magnetic and ionospheric disturbances in the case of S-210JA-16 are larger than that in S-210JA-7.

In the cases of S-210JA-7, -8, -10 and -16, it is interesting that there exists the change of the gradient of the electron density in the *D* region. This may suggest that the ionization by the auroral X-rays in the auroral zone disturbance contributes to the lower part of the *D* region (Kamiyama, 1966 a,b, 1967a,b; Rees, 1964; Rees *et al.*, 1969).

The decreases of the electron density at an altitude of about 80 km in the ascending mode and about 75 km in the descending mode in the case of S-210JA-18 and the change of the electron density gradient about 90 km in both the ascending and descending modes in the case of S-210JA-19 may have relations with the change in the ionizing agency.

The peak of the absorbing layer during polar cap absorption was estimated to be located in the altitude range between 55 km and 60 km throughout the day at College, Alaska by Parthasarathy *et al.* (1963), but the absorbing layer at Syowa Station is located at somewhat higher altitudes, that is, around 85 km. Though only the profiles in the nighttime are considered in the previous section, the profiles in the daytime can be considered to be similar according to such observations, that is, the peak of the increment of the electron density from the quiet condition exists in the altitude range between 90 km and 110 km.

As the polar ionosphere is very complicated, its interpretation requires other data such as the intensity and spectrum of auroral electrons, auroral X-rays intensity and so on. It is important to carry out simultaneous measurements of such quantities by sounding rockets (Miyazaki, 1974b, 1975a, b).

Chapter V Ion Transition Height Characteristics in the Topside Ionosphere by Satellite TAIYO Observation

5.1 Introduction

The topside ionosphere consists of electrons and mainly O^+, He^+, H^+ ions. The distributions of these ion species are generally explained by the diffusive equilibrium along the magnetic field line (Angerami and Thomas, 1964), but there remain the complex phenomena such as the equatorial anomaly concerning the low latitudes (Bramley and Peart, 1964). Recently, Titheridge (1976) indicates that the diurnal variations of the ion transition heights in the northern hemisphere and the southern hemisphere are very different from each other. The ion transition heights in the southern hemisphere are very lower than those in the northern hemisphere in the American zone.

The observations of the ion concentration by the Explorer 32 showed that the altitude of the $O^+ - H^+$ transition level exhibited a strong longitudinal dependence, that is, the ion transition heights at American longitudes (330°E – 20°E) were different from European and Pacific longitudes (70°E – 120°E and 190°E – 250°E respectively) (Taylor *et al.*, 1965, 1968). Brinton *et al.* (1970) explained that the difference was interpretted as an effect caused by the interaction between atmospheric winds and the magnetic field. Recently, Gledhill (1976) in his review paper mentioned that the aeronomic effects in the ionosphere at the South Atlantic geomagnetic anomaly were partly caused by the corpuscular precipitation.

The present chapter gives the observational results concerning the $O^+ - H^+$ ion transition height deduced from the retarding potential analyzer aboard TAIYO which is orbitting in the equatorial region. Besides this, various phenomena in connection with the South Atlantic geomagnetic regional anomaly were observed by other payloads (Hirao, 1975a,b).

5.2 TAIYO RPA Instrumentation and Orbit

The aeronomy satellite TAIYO was launched on February 24, 1975, into an orbit with an inclination of 31.6°, perigee of 255 km, and apogee of 3136 km.

A retarding potential analyzer is one of the seven scientific payloads aboard TAIYO. In the topside ionosphere, there exist O^+, He^+ and H^+ ions and the main constituent changes from O^+ to H^+ ions with height in the period of low solar activity. Therefore, the total ion current flowing into a detector is the sum of each ionic component. When two or three kinds of ion coexist, it is rather difficult to determine the density and temperature in the DC current voltage characteristic curve.

The derivative of the ion current with respect to the voltage applied to the electrode is:

$$\frac{\mathrm{d}j_i}{\mathrm{d}V} = -\frac{e^2 N_i}{\sqrt{2\pi k T_i M}} \exp\left\{-\left(\sqrt{\frac{eV}{kT_i}} - \frac{v_s}{v_p}\right)^2\right\} . \quad \cdots\cdots\cdots\cdots\cdots\cdots \quad (90)$$

where N_i is the ion density, T_i the ion temperature, M the ion mass, k the Boltzmann constant, e the unit charge, V the voltage applied to the electrode, v_s the satellite speed and $v_p = (2kT_i/M)^{1/2}$. Equation (90) shows that the peak value and its position change remarkably due to satellite speed and ion mass. Thus the characteristic of the derivative of the ion current with respect to the voltage changes remarkably with the mixing ratio of ions. The paper (Miyazaki, 1975) includes a more extensive description of the space craft TAIYO

and retarding potential analyzer.

5.3 Longitudinal and Latitudinal Variations of Ion Transition Heights

Here, the two kinds of ion, O^+ and H^+ are assumed to exist because the number of sunspots in 1975–1976 is at minimum. Since He^+ ions are minor constituent over the entire range during the period of low solar activity (Taylor *et al.*, 1968), and He^+ ions are not discussed in this paper.

Data stored in the tape recorder aboard the satellite of a total of 117 paths of the revolution and some of the real time data were used to investigate the longitudinal, latitudinal and diurnal variations of $O^+ - H^+$ ion transition heights. The period was between March 1975 and October 1976. The values of the planetary magnetic three-hour-range indices K_p in 63 paths show to be less than 2, the K_p's in 40 paths show to be 3 or 4 and the K_p's in 14 paths to be larger than 5. Thus, the most part of the observational period were under quiet condition.

The white circles in Fig. 99 show the longitudinal variation of $O^+ - H^+$ ion transition heights in the period of 06 – 18 hours local solar time. The location of the geomagnetic latitudes of the data points lies between about ±30° as the low inclination of the satellite trajectory. Although the data points are spread generally, the values between about 0°E – 100°E longitude are larger than those between about 200°E – 300°E. The cross marks in Fig. 99 show the nighttime ion transition height distributions. The range of the local solar time is between 18 and 06 hours. The ion transition heights are nearly constant over the whole longitudes, and spreading of the data points is smaller in contrast to the daytime condition.

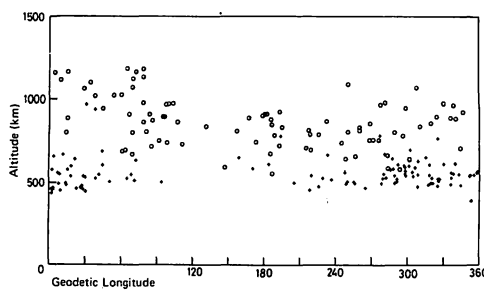


Fig. 99 Longitudinal $O^+ - H^+$ ion transition height characteristic in the daytime [o] and nighttime [+].

Fig. 100 shows the dip latitudinal variation of $O^+ - H^+$ ion transition heights in the period 06 – 18 hours local solar time. Fig. 101 shows the dip latitudinal variations of the relative ion densities at the $O^+ - H^+$ ion transition heights. The values of the ion transition heights are minima at the dip equator and become larger towards high latitudes. The values of the ion densities at the ion transition heights show maxima at the dip equator and become smaller towards high latitudes. On the other hand, the observational results in the nighttime indicate that the values of the ion transition heights are roughly constant over the dip lati-

tudes, $-40^\circ \sim +30^\circ$, and that the values of the ion densities exist in a wide range.

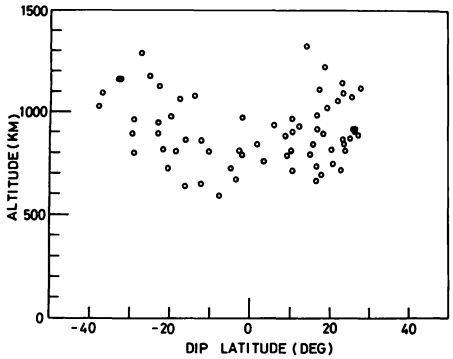


Fig. 100 Dip latitudinal $O^+ - H^+$ ion transition height characteristics in the daytime.

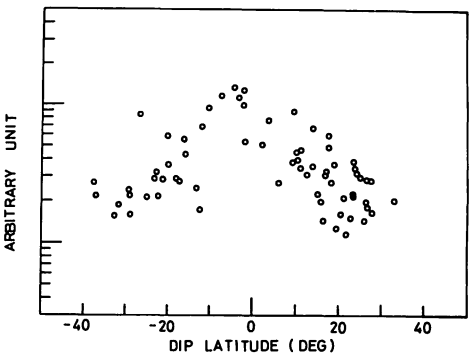


Fig. 101 The relative ion density variation characteristics at the ion transition heights against the dip latitudes in the daytime

5.4 Summary and Discussions

The main features of the present results are summarized below.

(a) In the daytime, the ion transition heights exist in the altitude ranging 700 – 1200 km.

(b) In the nighttime, the ion transition heights are nearly constant values of approximately 450 – 650 km in the whole longitudes, that is, there exist no remarkable difference in the longitudinal variation.

(c) But, there are some cases which the ion transition heights are rather low in the region of weak magnetic field.

(d) Concerning the dip latitudinal variations, at the dip equator, the transition heights are not so changeable against the local solar time but the ion densities at that level are very changeable. And it is interesting that the levels nearly coinside with the upper level of the equatorial anomaly, about 700 km.

(e) At the higher dip latitudes, the ion transition heights are very changeable against the local time variation, but the ion density variation becomes small towards the high dip latitudes.

Next, a semi-empirical formula of ion transition height is calculated in observational results. There are two assumptions to be considered that primary the formula consists of two parts; one does not depend on the solar condition and another depends on the solar condition, and that secondary the formula is a function of $\sin I$ and $\cos \chi$ in the following.

$$H = H_o + a \sin^2 I, \qquad \chi \geqq 90^\circ \quad \cdots\cdots\cdots\cdots\cdots\cdots \quad (91)$$

$$H = H_o + a \sin^2 I, + (b + c \sin^2 I) \cos^d \chi, \qquad \chi \leqq 90^\circ \quad \cdots\cdots\cdots\cdots\cdots\cdots \quad (92)$$

where H is $O^+ - H^+$ ion transition height in km, I is magnetic dip angle in degree and χ is solar zenith angle in degree.

Thus, the five coefficients are determined by the method of least squares by using observational data. These numerical figures are listed as follows.

$$H_0 = 591, a = -87.1, b = 217, c = 473, \text{and } d = 0.331.$$

As an interpretation of longitudinal and latitudinal variation of the ion transition heights, the perpendicular velocity to the magnetic field, of the charged particles induced from $\boldsymbol{E} \times \boldsymbol{B}$ in the daytime, where $\boldsymbol{E}$ is the electric field by the dynamo effect and $\boldsymbol{B}$ is the earth's magnetic field, is main factor. And also the neutral atmospheric wind in the F region is main factor. On the other hand, in the nighttime, it is considered that effects by the high energy particles (Hirao *et al.*, 1975) contribute in the Brazilian anomaly region, therefore, those levels are rather variable than other region.

Chapter VI Concluding Remarks

In this paper, firstly the various plasma probes are reviewed as well as the historical survey of the direct measurements of the ionospheric plasma with space vehicle. And various characteristics of the electrostatic probe and the radio frequency probe are analysed and cleared out from a view-point of ionospheric plasma probe. Especially the detailed analyses of the ion collection region for Langmuir probe and retarding potential analyzer with planar, spherical and cylindrical electrodes are performed when there exists relative velocity between a plasma and a probing electrode. Furthermore, impedance properties of two-wire radio frequency probe are investigated for both electrostatic and electromagnetic modes. In the last part of Chapter II, discussions are given about some problems in use of plasma probe on space vehicles.

A total of thirty-nine ionospheric sounding rockets were fired at Michikawa and Uchinoura. Twenty-eight rockets observations among of them made the ionospheric structure and properties clear, and a relation between sunspot number and the charged particle density in the upper atmosphere is derived from the observational results in Chapter III.

Twenty-one rockets were launched to observe the polar ionosphere and auroral phenomena at Syowa Station in Antarctica, during the 12th, 13th and 14th Japanese Antarctic Research Expeditions (1971–73) and fourteen electron density profiles were obtained. On these profiles, the author gave consideration to nighttime ones and, besides describing them in detail in relation to geomagnetic, ionospheric, auroral and other conditions, found empirical relations which connect the maximum increment of peak electron density and the height of its level in the D region during disturbed conditions with cosmic noise absorption in Chapter IV.

A retarding potential analyzer, RPA, with a planar Faraday cup was mounted on the satellite TAIYO. In Chapter V, descriptions of observational results by the RPA of the $O^+ - H^+$ ion transition height characteristic are given. The results indicate that the ion transition height correlates with the intensity of the geomagnetic field. Furthermore, it is important to know the distributions of densities of positive ions and electrons for the understanding of the problem of ionosphere-magnetosphere coupling. And much useful results will be obtained from the RPA from now on.

As the further ionospheric plasma probe studies, it is an important factor to consider the problems; the current return problem, the spacecraft equilibrium potential, photoelectric emission current, magnetic field effects, contact potentials, vehicle gassing, interference from

other equipment, ram and wake effects, the constraint of the data rate and so on. It is very important to measure detailed collision frequency and electron density profiles as well as negative ion density profile in order to discuss precisely the various properties of the lower ionosphere. It is also an important factor to consider the sampling volume of the sensor for both the electrostatic and radio frequency probes. And it is also necessary to analyse the more detailed characteristic of the sheath-plasma system in order to get precise knowledge of the space plasma because a plasma covers wide range of density and temperature. Synthetic studies for disturbed and quiet conditions of the ionosphere by simultaneous measurements with many sensors are also important.

While it is probably easy to obtain erroneous results with plasma probes in space, it is probably possible to obtain exact characteristics of the plasma with a careful study in theory and experiment. There is no doubt that plasma probe will be one of commonest of the spacecraft payloads. And much fruitful results which will be obtained from those measurements perhaps serve to not only the progress of space science but also the wonderful progress of humankind for ever.

Acknowledgements

The author wishes to express his sincere thanks to Prof. K. Hirao of the Institute of Space and Aeronautical Science, University of Tokyo for his valuable discussions and continuous encouragements throughout the present work. The author's deep gratitude is also tendered to Prof. N. Fukushima, Prof. T. Oguchi, Prof. T. Tohmatsu, Prof. T. Obayashi and Prof. T. Itoh for their valuable guidances and advices. Sincere thanks are also due to Prof. K. Kaneshige, Prof. K. Takayama, Prof. T. Yonezawa, Prof. M. Hirono, Dr. Y. Aono, Dr. Y. Nakata, Dr. K. Tao, Dr. T. Ishida and Dr. T. Dote for their continuous advices and encouragements.

The author deeply indebted to Prof. T. Nagata and Dr. I. Kasuya for having opportunity to join a member of the wintering party of the 13th Japanese Antarctic Research Expedition (February, 1972 – February, 1973) and participate the rocket experiments at Syowa Station in Antarctica.

The main part of the present work was done under the research projects of Artificial Satellite Research Division, Radio Research Laboratories. The rocket observation projects have been supported by the Institute of Space and Aeronautical Science, University of Tokyo and the National Institute of Polar Research.

References

Allen, J.E., R.L.F. Boyd and P. Raynolds, The collection of positive ions by a probe immersed in a plasma, Proc. Phys. Soc., B, **70**, 297–304, 1957.

Alpert, Y.L., A.V. Gurevich and L.P. Pitayevsky, On the effects produced by a fast-moving body in a plasma, Space Research III, 1224–1271, 1962.

Angerami, J.J. and J.O. Thomas, Studies of planetary atmospheres, 1, The distribution of electrons and ions in the earth's exosphere, J. Geophys. Res., **69**, 4537–4560, 1964.

Aono, Y., K. Hirao and S. Miyazaki, Rocket observation of ion density in the ionosphere, J. Radio Res. Labs., **8**, 441–451, 1961a.

Aono, Y., K. Hirao, S. Miyazaki, T. Ichimiya, K. Takayama and T. Dote, Positive ion and electron densities of the ionosphere measured by sounding rockets, Space Research II, 1215–1219, 1961b.

Aono, Y., K. Hirao, S. Miyazaki, T. Ichimiya, K. Takayama, T. Dote, T. Sugiyama and T. Muraoka, Positive ion density, electron density and electron temperature in the ionosphere by the Kappa rocket, Proceedings of the Third International Symposium on Rockets and Astronautics Tokyo, 401–405, 1961c.

Aono, Y., K. Hirao and S. Miyazaki, Positive ion density, electron density and electron temperature in the ionosphere by the Kappa-8-5 and -6 rockets, J. Radio Res. Labs., **8**, 453–465, 1961d.

Aono, Y., K. Hirao and S. Miyazaki, Rocket observation of ion density, electron density and electron temperature in the ionosphere, J. Radio Res. Labs., **9**, 407–419, 1962a.

Aono, Y., K. Hirao and S. Miyazaki, Profiles of electron temperature, electron density and ion density observed with Kappa rocket, Proceedings of the Forth International Symposium on Rockets and Astronautics Tokyo, 1962b.

Aono, Y., K. Hirao and S. Miyazaki, Profile of charged particle density in the ionosphere observed with rockets, Space Research III, 221–227, 1963.

Baker, K.D., A.M. Despain and J.C. Ulwick, Simultaneous comparison of RF probe techniques for determination of ionospheric electron density, J. Geophys. Res., **71**, 935–944, 1966.

Balmain, K.G., Impedance of a radio-frequency plasma probe with an absorptive surface, Radio Sci., **1**, 1–12, 1966.

Balmain, K.G. and G.A. Oksiutik, RF probe admittance in the ionosphere, Theory and experiment, Plasma Waves in Space and Laboratory Vol. 1, ed. by J.O. Thomas and B.J. Landmark, pp. 247–261, Edinburgh Univ. Press, New York, 1969.

Bates, D.R. and T.N.L. Patterson, Helium ions in the upper atmosphere, Planet. Space Sci., **9**, 599–605, 1962.

Bourdeau, R.E., Ionospheric research from space vehicles, Report of NASA GSFC X-615-62-234, 1962.

Bourdeau, R.E., J.H. Chapman and K. Maeda, Ionospheric research by means of rockets and satellites, Progress in Radio Science 1960–1963 Vol. VIII, ed. by K. Maeda and S. Silver, pp. 5–70, Elsevier Publishing Company, Amsterdam, 1965.

Bramley, E.N. and M. Peart, Diffusion and electromagnetic drift in the equatorial F_2 region, J. Geophys. Res., **69**, 4609–4616, 1964.

Brillouin, L., Theory of the magnetron, I, Phys. Rev., **60**, 385–396, 1941.

Brinton, H.C., R.A. Pickett and H.A. Taylor, Jr., Thermal ion structure of plasmasphere,

Planet. Space Sci., **16**, 899–909, 1968.

Brinton, H.C., H.G. Mayr, R.A. Pickett and H.A. Taylor Jr., The effect of atmospheric winds on the $O^+ - H^+$ transition level, Space Research X, 652–662, 1970.

Buckley, R., A theory of resonance rectification, The response of a spherical plasma probe to alternating potentials, Proc. Roy. Soc., **A290**, 186–219, 1966.

Buckley, R., The response of a spherical plasma probe to alternating potentials, Results of computations and use for plasma diagnostics, J. Plasma Phys., **1**, 171–191, 1967.

Budden, K.G., Radio Waves in the Ionosphere, Cambridge Univ. Press, Cambridge, 1961.

Chan, K., L. Colin and J.O. Thomas, Electron densities and scale heights in the top-side ionosphere, NASA SP-3027, 1966.

Chandra, S. and R.A. Goldberg, Geomagnetic control of diffusion in the upper atmosphere, J. Geophys. Res., **69**, 3187–3198, 1964.

Crawford, F.W. and R.S. Harp, The resonance probe–A tool for ionospheric and space research, J. Geophys. Res., **70**, 587–596, 1965.

Crawford, F.W., Plasma resonance probe characteristics in a magnetic field, J. Appl. Phys., **36**, 3142–3145, 1965.

Davies, K., Ionospheric Radio Propagation, National Bureau of Standards Monograph 80, pp. 138–140, U.S. Government Printing Office, Washington, D.C., 1965.

Davies, P.G., The electrical properties of a spherical plasma probe near the plasma frequency, Proc. Phys. Soc., **88**, 1019–1032, 1966.

DeForest, S.E., Spacecraft charging at synchronous orbit, J. Geophys. Res., **77**, 651–659, 1972.

Dote, T., K. Takayama and T. Ichimiya, Analysis of probe characteristics in drifting plasma, J. Phys. Soc. Japan, **17**, 174–183, 1962.

Dote, T., T. Ichimiya and F. Tamaki, Some experiments on probe characteristics in drifting plasma, J. Phys. Soc. Japan, **18**, 260–265, 1963.

Dote, T. and H. Amemiya, Negative characteristic of a cylindrical probe in a magnetic field, J. Phys. Soc. Japan, **19**, 1915–1924, 1964.

Dote, T. and T. Ichimiya, Characteristics of resonant probes, J. Appl. Phys., **36**, 1866–1872, 1965.

Dote, T. and H. Amemiya, Analysis of the negative characteristic of a cylindrical probe in a magnetic field, J. Phys. Soc. Japan, **22**, 270–276, 1967.

Dote, T. and T. Ichimiya, Characteristics of plasma resonance probe and RF impedance probe in a magnetic field, J. Phys. Soc. Japan, **22**, 1266–1273, 1967.

Ejiri, M., T. Dote, S. Miyazaki, T. Aso and S. Matsumura, Electron density measurements with R.F. and D.C. plasma probes in low density plasmas, Rept. Ionos. Space Res. Japan, **27**, 229–232, 1973.

Ejiri, M., Study of RF plasma probes and its application to the rocket and satellite observations, pp. 139–141, Institute of Space and Aeronautical Science, Univ. of Tokyo, 1973.

Gledhill, J.A., Aeronomic effects of the South Atlantic anomaly, Rev. Geophys. Space Phys., **14**, 173–187, 1976.

Hakura, Y., ed., Solar-terrestrial events in August 1972, Rept. Ionos. Space Res. Japan, **27**, 145–189, 1973.

Hanson, W.B., Structure of the ionosphere, Satellite Environment Handbook, ed. by F.S. Johnson, pp. 27–46, Stanford Univ. Press, Stanford, California, 1961.

Hanson, W.B. and D.D. McKibbin, An ion-trap measurement of the ion concentration profile

above the F_2 peak, J. Geophys. Res., **66**, 1667–1671, 1961.
Hanson, W.B., D.D. McKibbin and G.W. Sharp, Some ionospheric measurements with satellite-borne ion traps, J. Geophys. Res., **69**, 2747–2764, 1964.
Harp, R.S. and F.W. Crawford, Characteristics of the plasma resonance probe, J. Appl. Phys., **35**, 3436–3446, 1964.
Heatley, A.H., Collector theory for ions with Maxwellian and drift velocities, Phys. Rev., **52**, 235–238, 1937.
Heikkila, W.J., N. Eaker, J.A. Fejer, K.R. Tipple, J. Hugill, D.E. Schneible and W. Calvert, Comparison of several probe techniques for ionospheric electron concentration measurements, J. Geophys. Res., **73**, 3511–3535, 1968.
Heikkila, W.J., Laboratory study of probe impedance, Plasma Waves in Space and Laboratory Vol. 1, ed. by J.O. Thomas and B.J. Landmark, pp. 231–246, Edinburgh Univ. Press, New York, 1969.
Hirao, K. and S. Miyazaki, Ion probe used in the Japanese sounding rocket, Aeronomy Report No. 1, 14–16, Univ. of Illinois, 1963a.
Hirao, K. and S. Miyazaki, Resonance probe available for the IQSY, Aeronomy Report No. 1, 17–20, Univ. of Illinois, 1963b.
Hirao, K. and S. Miyazaki, Rocket-borne ionospheric direct-sounding instruments, J. Radio Res. Labs, **12**, 357–380, 1965.
Hirao, K., S. Miyazaki, M. Ohshio, N. Fugono and I. Shiro, Direct observations of the ionosphere by sounding rockets during the IQSY, J. Radio Res. Labs., **13**, 75–139, 1966.
Hirao, K., Layer structure in the electron temperature profile in the ionosphere, J. Geomag. Geoelectr., **18**, 333–341, 1966.
Hirao, K. and S. Miyazaki, Relation between sunspot number and charged particle density in the upper ionosphere, J. Geomag. Geoelectr., **19**, 261–265, 1967.
Hirao, K., The satellite TAIYO, Scientific objectives and preliminary results, Rept. Ionos. Space Res. Japan, **29**, 99–104, 1975a.
Hirao, K., The TAIYO mission, J. Geomag. Geoelectr., **27**, 265–270, 1975b.
Hirao, K., M. Matsuoka and F. Nagai, Anomalous intense count observed with SXR instrument aboard TAIYO in the ionosphere over South America, Abstract of the 58th Annual Meetings of Society of Terrestrial Magnetism and Electricity Japan, I-40, October 1975 (in Japanese).
Hirasawa, T., T. Nagata, S. Kawaguchi and K. Hirao, Rocket observations of electron density of daytime ionosphere at Syowa Station, Antarctica, Rept. Ionos. Space Res. Japan, **24**, 237–243, 1970.
Holt, O. and J. Trøim, Impedance of a radio frequency plasma probe in a static magnetic field, Plasma Waves in Space and Laboratory Vol. 1, ed. by J.O. Thomas and B.J. Landmark, pp. 263–284, Edinburgh Univ. Press, New York, 1969.
Hoult, D.P., Weak shock waves in the ionosphere, J. Geophys. Res., **69**, 4617–4620, 1964.
Hoult, D.P., *D*-region probe theory, J. Geophys. Res., **70**, 3138–3187, 1965.
Hoult, D.P. and T.J. Kuo, First-order corrections to *D*-region probe theory, J. Geophys. Res., **71**, 3191–3200, 1966.
Huddlestone, R.H. and S.L. Leonard, Plasma Diagnostic Techniques, Academic Press, New York–London, 1965.
Ichikawa, Y.H., Theoretical analysis of the characteristics of resonance probe, IPPJ-14, 1–21, Nagoya Univ., 1963.

Ichimiya, T., K. Takayama, H. Ikegami, Y. Aono, K. Hirao and S. Miyazaki, Resonance probe for measurement of electron density in the ionosphere, Proceedings of the Second International Symposium on Rockets and Astronautics Tokyo, 245–248, 1960.

Ichimiya, T., K. Takayama, T. Dote, Y. Aono, K. Hirao, S. Miyazaki, T. Sugiyama and T. Muraoka, Measurement of positive-ion density in the ionosphere by sounding rocket, Nature, **190**, 156–158, 1961.

Ichimiya, T., T. Dote and K. Takayama, Some problems in use of ionospheric probe on sounding rockets, J. Inst. Elect. Engnr. Japan, **85**, 1957–1959, 1965 (in Japanese).

Ikegami, H. and K. Takayama, Resonance probe, IPPJ-10, 1–31, Nagoya Univ., 1963.

Ikeji, H. and K. Takayama, Resonances of radio frequency probe in a plasma, J. Phys. Soc. Japan, **21**, 2021–2028, 1966.

Isozaki, S. and S. Miyazaki, Riometer records of 30 MHz cosmic noise at Syowa Station, Antarctica in 1972, JARE Data Report, 20 (Ionosphere), 1–76, Polar Research Center National Science Museum, 1973.

Jackson, J.E. and J.A. Kane, Measurement of ionospheric electron densities using an RF probe technique, J. Geophys. Res., **64**, 1074–1075, 1959.

Jackson, J.E. and S.J. Bauer, Rocket measurement of a daytime electron density profile up to 620 km, J. Geophys. Res., **66**, 3055–3057, 1961.

Kaiser, T.R., The admittance of an electric dipole in a magneto-ionic environment, Planet. Space Sci., **9**, 639–657, 1962.

Kaiser, T.R. and J.K.E. Tunaley, Radio-frequency impedance probes, Space Sci. Rev., **8**, 32–73, 1968.

Kamiyama, H., Ionization and excitation by precipitating electrons, Rept. Ionos. Space Res. Japan, **20**, 171–187, 1966a.

Kamiyama, H., Flux of bremsstrahlung photons caused by energetic electrons precipitating into the upper atmosphere, Rept. Ionos. Space Res. Japan, **20**, 374–394, 1966b.

Kamiyama, H., The dependence of the relative intensities of some of the auroral line upon the energy spectrum of precipitating electrons, The Science Reports of the Tohoku Univ., **18**, 83–90, 1967a.

Kamiyama, H., The electron density distribution in the lower ionosphere produced through impact ionization by precipitating electrons and through photoionization by the associated bremsstrahlung X-rays, J. Geomag. Geoelectr., **19**, 27–47, 1967b.

Kanal, M., Theory of current collection of moving cylindrical probes, J. Appl. Phys., **35**, 1697–1703, 1964.

Kane, J.A., Electron densities in the *E* region deduced from rocket observations, Electron Density Profiles in the Ionosphere and Exosphere, ed. by B. Maehlum, pp. 67–79, Pergamon Press, London, 1962.

Kasuya, I. and K. Sawada, Comparison of f_0F2 at four observatories in Japan, J. Radio Res. Labs., **3**, 45–53, 1956.

Knudsen, W.C. and G.W. Sharp, Ion temperature measured around a dawn-dusk-auroral-zone satellite orbit, J. Geophys. Res., **72**, 1061–1072, 1967.

Kostelnicek, R.J., An investigation of boundary theories for the resonance probe, Radio Sci., **3**, 319–324, 1968.

Langmuir, I. and K.B. Blodgett, Currents limited by space charge between concentric spheres, Phys. Rev., **22**, 347–356, 1923.

Langmuir, I. and K.B. Blodgett, Currents limited by space charge between coaxial cylinders,

Phys. Rev., **24**, 49–59, 1924.
Medicus, G., Theory of electron collection of spherical probes, J. Appl. Phys., **32**, 2512–2520, 1961.
Medicus, G., Spherical Langmuir probe in 'drifting' and 'accelerated' Maxwellian distribution, J. Appl. Phys., **33**, 3094–3100, 1962.
Messiaen, A.M. and P.E. Vandenplas, High-frequency dielectric resonance probe for the measurement of plasma densities, J. Appl. Phys., **37**, 1718–1724, 1966.
Miyazaki, S., K. Hirao, Y. Aono, K. Takayama, H. Ikegami and T. Ichimiya, Resonance probe–A new probe method for electron density and electron temperature in the ionosphere, Rept. Ionos. Space Res. Japan, **14**, 148–159, 1960.
Miyazaki, S., Results of electron density measurements by sounding rockets L-3H-2 and 3, J. Geomag. Geoelectr., **18**, 481–483, 1966.
Miyazaki, S., K. Hirao, M. Ohshio, N. Fugono, I. Shiro and T. Koizumi, Direct observations of the ionosphere by sounding rockets K-9M-15, L-3H-1 and L-3H-2, J. Radio Res. Labs., **13**, 185–200, 1966.
Miyazaki, S., K. Hirao and N. Fugono, Direct observation of the ionosphere with sounding rocket K-9M-20, J. Radio Res. Labs., **14**, 185–193, 1967.
Miyazaki, S., Ionospheric measuring probe–Retarding potential trap–, J. Radio Res. Labs., **14**, 209–217, 1967a.
Miyazaki, S., Characteristic of ion collection of the spherical Langmuir probe in drifting Maxwellian distribution, J. Radio Res. Labs., **14**, 219–224, 1967b.
Miyazaki, S. and H. Mori, Ionospheric measuring probe (II)–Retarding potential trap–, J. Radio Res. Labs., **15**, 69–80, 1968.
Miyazaki, S., Radio frequency characteristic of electrode immerced in magnetoplasma and application to plasma diagnostic techniques (I), J. Radio Res. Labs., **15**, 81–103, 1968.
Miyazaki, S., Probe impedance loss in the cold magnetoplasma, Rept. Ionos. Space Res. Japan, **23**, 75–78, 1969.
Miyazaki, S., Preliminary observation of polar ionosphere by low frequency pulse sounder, J. Geomag. Geoelectr., **26**, 79–81, 1974a.
Miyazaki, S., Rocket observations of the ionosphere over Syowa Station, Antarctica, J. Radio Res. Labs., **21**, 551–572, 1974b.
Miyazaki, S., Results of rocket observation of electron density at Syowa Station, Antarctic Record No. 52, 128–140, National Institute of Polar Research Japan, 1975a.
Miyazaki, S., Relation between lower ionospheric electron density profiles and cosmic noise absorption during auroral zone disturbances, J. Geomag. Geoelectr., **27**, 113–129, 1975b.
Miyazaki, S., The retarding potential analyzer aboard the satellite TAIYO, J. Geomag. Geoelectr., **27**, 311–320, 1975c.
Mori, H., M. Ejiri and T. Aso, Plasma wave effect on radio frequency probe characteristic, Abstract of the 53rd Annual Meetings of Society of Terrestrial Magnetism and Electricity Japan, I-68, April, 1973.
Mori, H., T. Ogawa and S. Miyazaki, Rocket observations of plasma irregularities in the polar *E* region, Antarctic Record No. 52, 141–146, National Institute of Polar Research Japan, 1975a.
Mori, H., T. Ogawa, S. Miyazaki, K. Hirao and K. Oyama, Observations of electron density, temperature and irregularities by the rocket S-310-2, Abstract of the 58th Annual Meet-

ings of Society of Terrestrial Magnetism and Electricity Japan, I-26, October, 1975b.
Mott-Smith, H.M. and I. Langmuir, The theory of collectors in gaseous discharges, Phys. Rev., **28**, 727–763, 1926.
Nagata, T. and T. Tohmatsu, Modern Aeronomy, Syokabo, Tokyo, 1973 (in Japanese).
Newell, H.E., The upper atmosphere studied by rockets and satellites, Physics of the Upper Atmosphere, ed. by J.A. Ratcliffe, p. 108, Academic Press, New York, 1960.
Ogata, T. and M. Ose, Riometer record of 30 MHz cosmic noise at Syowa Station, Antarctica in 1971, JARE Data Reports, No. 18 (Ionosphere), 1–62, Polar Research Center National Science Museum, 1972.
Ogawa, T., H. Mori and S. Miyazaki, Electron density irregularities observed in the antarctic auroral *E* region, J. Radio Res. Labs., **22**, 1–21, 1975.
Oyama, K., Characteristic of the contaminated Langmuir probe and countermoves for its application to the space observations, Report of Institute of Space and Aeronautical Science No. 525, Univ. of Tokyo, 1975.
Parthasarathy, R., G.M. Lerfald and C.G. Little, Derivation of electron-density profiles in the lower ionosphere using radio absorption measurements at multiple frequencies, J. Geophys. Res., **68**, 3581–3588, 1963.
Pavkovich, J.M. and G.S. Kino, RF behavior of the plasma sheath, M.L. Report No. 1077, 1–17, Stanford Univ., 1963.
Pavkovich, J.M., Numerical calculations related to the RF properties of the plasma sheath, M.L. Report No. 1093, 1–175, Stanford Univ., 1963.
Pyati, V.P. and H. Well, Capacitance of biconical antennas in magneto-ionic media; Elliptic cone capacitance, Radio Sci., **69D**, 291–298, 1965.
Radio Research Laboratories, Ionospheric Data at Syowa Station (Antarctica), ION. ANT-16, -17, -18, -19, 1971–1972.
Radio Research Laboratories, Solar-terrestrial disturbances of August 1972, Rev. Radio Res. Labs., **19**, 245–390, 1973 (in Japanese).
Rees, M.H., Ionization in the earth's atmosphere by aurorally associated bremsstrahlung X-rays, Planet. Space Sci., **12**, 1093–1108, 1964.
Rees, M.H., A.I. Stewart and J.C.G. Walker, Secondary electrons in Aurora, Planet. Space Sci., **17**, 1997–2008, 1969.
Smith, L.G., Electron density measurements by the asymmetric probe, J. Geophys. Res., **66**, 2562, 1961.
Smith, L.G., Rocket observations of sporadic *E* and related features of the *E* region, Radio Sci., **1**, 178–186, 1966.
Sonin, A.A., Theory of ion collection by a supersonic atmospheric sounding rocket, J. Geophys. Res., **72**, 4547–4557, 1967.
Spiwak, G. and E. Reichrudel, Theory of collector currents in a plasma disturbed by a magnetic field, Technical Physics of the USSR, **5**, 715–724, 1938.
Stix, T.H., The Theory of Plasma Waves, p. 10, McGraw-Hill, New York, 1962.
Stratton, J.A., Electromagnetic Theory, p. 275, McGraw-Hill, New York, 1941.
Takayama, K., H. Ikegami and S. Miyazaki, Plasma resonance in a radio-frequency probe, Phys. Rev. Letters, **5**, 238–240, 1960.
Taylor, H.A., H.C. Brinton and C.R. Smith, Positive ion composition in the magnetosphere obtained from the Ogo-A satellite, J. Geophys. Res., **70**, 5769–5782, 1965.
Taylor, H.A. Jr., H.C. Brinton, M.W. Pharo III and M.K. Rahman, Thermal ions in the

exosphere; Evidence of solar and geomagnetic control, J. Geophys. Res., **73**, 5521–5533, 1968.

Titheridge, J.E., Ion transition heights from topside electron density profiles, Planet. Space Sci., **24**, 229–245, 1976.

Ulwick, J.C., W. Pfister, R.P. Vancour, R.T. Bettinger, O.C. Haycock and K.D. Baker, Firing of an Astrobee 200 rocket with a multiple ionospheric experiment, Proc. Inst. Radio Engn., **50**, 2272–2286, 1962.

University of Tokyo, Sounding Rocket Data in Japan Vol. 1 (1958–1972), ed. by Department of Space Sciences, 1–249, Institute of Space and Aeronautical Science, Univ. of Tokyo, 1972.

Uramoto, J., J. Fujita, H. Ikegami and K. Takayama, RF current component in the resonance probe, IPPJ-19, 1–15, Nagoya Univ., 1963.

Wait, J.R., Quasi-static theory of a cylindrical impedance probe for magnetoplasma, Radio Sci., **1**, 1297–1301, 1966.

Wait, J.R., Further note on the quasi-static theory of a cylindrical impedance probe for magnetoplasma, Radio Sci., **2**, 253–256, 1967.

Whitten, R.C. and I.G. Poppoff, Physics of the Lower Ionosphere, Prentice-Hall, INC., Englewood Cliffs, New Jersey, 1965.

Yonezawa, T., On the physical properties and composition of the upper atmosphere between 100 km and 400 km above ground in middle latitudes, J. Radio Res. Labs., **7**, 67–84, 1960.